Green Chemistry

CRITICAL REVIEW

View Article Online
View Journal | View Issue

Cite this: *Green Chem.*, 2026, **28**, 5131

Electrocatalytic activation of C–H, C–O, and C–C bonds in biomass valorization: mechanisms and catalysts

Mengyuan Liu,†[a] Guohao Xu,†[b] Chendong Lin,[a] Xiaotong Chen,[b] Boyang Lin,[a] Wei Liu *[b] and Shunji Xie *[a]

Received 27th November 2025,
Accepted 13th February 2026

DOI: 10.1039/d5gc06393k

rsc.li/greenchem

Electrocatalytic activation of specific C–H, C–O, and C–C bonds in biomass is crucial for producing sustainable high-value chemicals and fuels under mild conditions. Key challenges include selective differentiation of chemically similar bonds and suppression of parasitic reactions. This review comprehensively analyzes mechanisms and catalyst designs for selective bond activation in key biomass platforms (*e.g.*, glucose, glycerol, 5-hydroxymethylfurfural, lignin derivatives). We attempt to present a summary of existing selective C–H, C–O, and C–C bond activation strategies. Each strategy is illustrated in terms of the bond activation mechanism, representative catalyst systems, and optimization of conditions. Finally, pending challenges and potential opportunities related to selective bond activation strategies are discussed to propose future research directions. We hope that this review will help inspire further progress in designing new selective approaches for biomass valorization.

Green foundation

1. This review highlights electrocatalytic strategies for the selective activation of C–H, C–O, and C–C bonds in biomass under mild conditions, enabling high-value product synthesis (*e.g.*, glucaric acid, FDCA, BHMF) with >90% selectivity. Catalyst innovations (single-atom, high-entropy alloys) and process optimization (pH/potential control) reduce energy inputs and eliminate harsh reagents.
2. The work bridges renewable electricity and biomass valorization, offering a carbon-neutral route to replace fossil-derived chemicals. Its scalable, aqueous-phase processes address global challenges in sustainable energy, a circular economy, and climate mitigation.
3. The future will focus on rational catalyst design (*e.g.*, bio-inspired, non-precious metals), mechanism-driven innovation using *in situ* spectroscopy and AI, and integrated system engineering for energy-efficient paired electrolysis. This review shapes the field by providing a unified "bond-activation" framework, critically outlining key challenges and future directions. It will accelerate progress by guiding research beyond model compounds to real biomass, fostering interdisciplinary convergence (*e.g.*, electrochemistry, data science), and ultimately pushing this technology toward practical, sustainable chemical production.

1. Introduction

Biomass resources have garnered significant attention due to their renewable characteristics and carbon-neutral technology potential, given that the non-renewable nature of fossil fuels (*e.g.*, petroleum, coal, natural gas) leads to reserve depletion and overexploitation crises, posing severe challenges for global energy security and sustainable economic development.[1,2] Biomass encompasses diverse carbon sources, including photosynthetic products from plants (*e.g.*, wood, crop straw), organic waste (agricultural residues, food waste), and microbial metabolic byproducts.[3,4] These resources can be converted into energy carriers (*e.g.*, bioethanol, syngas) and high-value chemicals (*e.g.*, platform molecules, bio-based materials) through thermochemical, biocatalytic, or electrochemical pathways.[5–7] Their unique advantages are twofold: first, biomass utilization significantly reduces dependence on fossil fuels, mitigating risks associated with a monolithic energy structure. Second, their inherent carbon cycling forms a closed-loop system—plants absorb atmospheric CO_2 *via* photosynthesis, and the CO_2 released during biomass conversion is reabsorbed by subsequent generations of plants, achieving near-zero net carbon emissions over the entire life

[a]*State Key Laboratory of Physical Chemistry of Solid Surfaces, Collaborative Innovation Center of Chemistry for Energy Materials, National Engineering Laboratory for Green Chemical Productions of Alcohols, Ethers and Esters, College of Chemistry and Chemical Engineering, Xiamen University, Xiamen, 361005, China. E-mail: shunji_xie@xmu.edu.cn*
[b]*School of Chemistry and Chemical Engineering, Central South University, Changsha, Hunan 410083, China. E-mail: wliu300@csu.edu.cn*
†These authors are the co-first authors.

cycle.[8] This "carbon-neutral" characteristic positions biomass as a strategic resource bridging energy transition and climate governance, offering a key technological pillar for building a sustainable society.

The high-value transformation of biomass resources fundamentally relies on the selective activation and reconstruction of characteristic chemical bonds within their molecular structures. Biomass primarily consists of three polymeric components: (1) polysaccharides (cellulose and hemicellulose) featuring C–O–C glycosidic bonds as their backbone with abundant C–OH and C–H bonds;[9] (2) lignin, a three-dimensional network structure crosslinked through C–O ether and C–C bonds;[10] and (3) lipids/terpenoids characterized by extended C–C bonds and ester functionalities.[11] To achieve efficient valorization, distinct activation strategies must be developed for each bond type: C–H bond functionalization enables the production of valuable aldehydes, ketones, and carboxylic acids *via* selective oxidation processes;[12,13] C–O bond cleavage requires tailored depolymerization approaches;[14] and C–C bond activation presents unique challenges due to its high bond dissociation energy and nonpolar nature.[15,16] Conventional thermocatalytic methods face significant limitations, including a dependence on precious metals (*e.g.*, Pd-mediated C–H activation), corrosive acid/base requirements (for C–O bond scission), and undesirable product distributions from high-temperature pyrolysis (for C–C bond cleavage).[17–19] Emerging electrocatalytic technologies present significant advantages. While current high-performance systems often depend on noble-metal benchmarks, this approach creates a promising pathway for utilizing Earth-abundant alternatives, such as alloys or phosphides of nickel, iron, and copper. These materials enable enhanced control over reaction selectivity and efficiency under comparatively mild conditions.

Electrocatalytic biomass conversion has emerged as a revolutionary approach for sustainable biorefining due to its transformative potential. This technology demonstrates three fundamental advantages: (1) mild reaction conditions (ambient temperature and pressure) significantly reduce the high energy consumption and equipment corrosion risks associated with conventional thermocatalysis;[20,21] (2) direct utilization of renewable electricity achieves nearly 90% energy conversion efficiency, dramatically minimizing energy loss;[22,23] (3) the unique spatial separation of half-reactions (independent anodic oxidation and cathodic reduction) effectively suppresses side reactions.[24,25] Importantly, precise modulation of the electrode potential enables atomic-level selective activation of C–H, C–O, and C–C bonds, endowing biomass molecular frameworks with programmable reconstruction capabilities, a breakthrough that circumvents the harsh reaction conditions required by traditional catalysis.

To the best of our knowledge, existing reviews on biomass valorization predominantly focus on the electrocatalytic conversion of specific alcohols or polyols, with limited systematic analysis of bond activation mechanisms.[26–28] To bridge this critical gap, this review proposes a bond activation-oriented classification framework to systematically elucidate electrocatalytic mechanisms for biomass-derived C–H, C–O, and C–C bond transformations (Fig. 1): (a) C–H bond activation focuses on selective oxidation reactions of carbohydrates, revealing hydrogen abstraction mechanisms mediated by reactive oxygen species and electronic state modulation strategies at catalytic interfaces; (b) C–O bond cleavage is categorized as oxidative cleavage and reductive hydrogenolysis, with an emphasis on the regulatory role of interfacial pH and potential in proton-coupled electron transfer (PCET) processes; (c) C–C bond activation explores oxidative decarboxylation and nucleophilic oxidation, highlighting synergistic effects between catalyst crystallographic facets and bifunctional active sites. As sustainable utilization of biomass resources gains global momentum, this review critically examines advanced catalyst design principles and the depolymerization of lignin, catalysts for selective bond scission and mechanistic characterization techniques. In summary, this paper aims to provide a comprehensive description of electrolytes, catalytic sites, and considerations for specific biomass conversion pathways from the perspective of electrocatalytic activation, cleavage and functionalization mechanisms of different types of C–H, C–O, and C–C bonds.

Mengyuan Liu

Mengyuan Liu obtained her PhD degree from China University of Petroleum in 2023. She is now working in Prof. Ye Wang's group as a post-doctoral fellow at the College of Chemistry and Chemical Engineering of Xiamen University (China). Her research focuses on the design of catalysts and the study of reaction mechanisms for the conversion of biomass into high-value-added chemicals.

Guohao Xu

Guohao Xu is currently pursuing a PhD in Metallurgical Physical Chemistry at Central South University under the supervision of Prof. Wei Liu. His research focuses on efficient electro- and chemical conversion of biomass and polyester plastics.

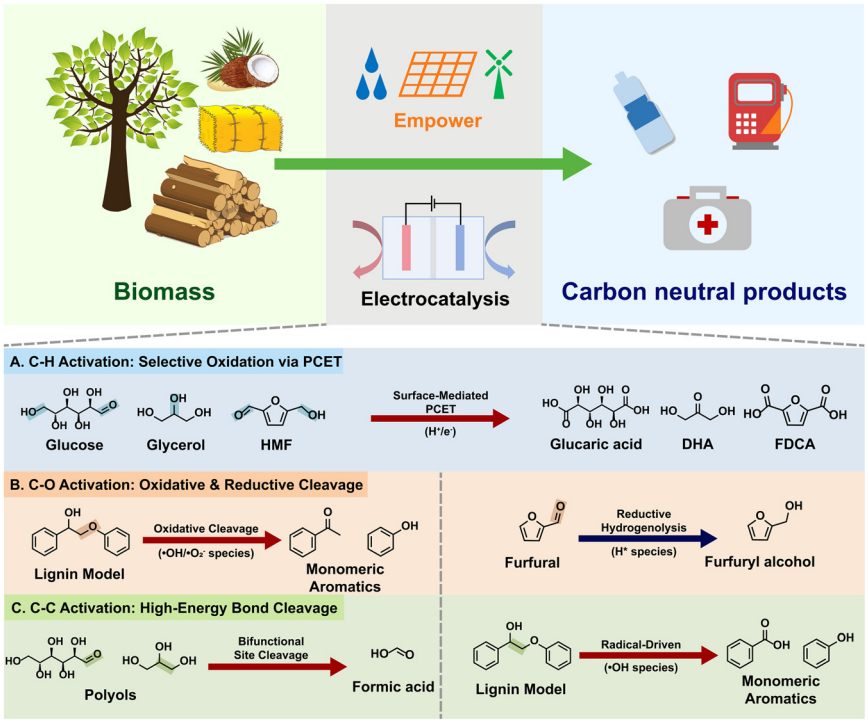

Fig. 1 Electrocatalysis-driven biomass valorization: selective activation and reconstruction of C–H, C–O, and C–C bonds.

2. Electrocatalytic activation of C–H bonds

As fundamental building blocks of organic molecular frameworks, C–H bonds are ubiquitous in biomass and its derived compounds. Selective functionalization of these bonds enables the direct introduction of oxygen-containing functional groups (*e.g.*, carboxyl, ketone, and aldehyde groups), thereby facilitating the synthesis of high-value-added chemicals.[26,27] Concurrently, electrocatalytic oxidation has emerged as a novel green strategy that utilizes external electric fields to regulate reaction pathways, demonstrating unique potential for the targeted transformation of C–H bonds in biomass.[28,29] Compared to conventional methods, C–H bond oxidation strategies offer significant advantages: (1) improved atom economy, (2) streamlined synthesis routes, and (3) compatibility with green processes.[30,31] However, the inherent high bond dissociation energy and low polarity of C–H bonds make their activation highly challenging. Furthermore, the coexis-

Wei Liu

Wei Liu received his PhD from the Georgia Institute of Technology. His international experience includes serving as a state-sponsored Visiting Scholar at the Renewable Bioproducts Institute at Georgia Institute of Technology (2012–2015) and conducting postdoctoral research at Texas A&M University in 2020. In 2021, he joined the Central South University as a professor. His current research focuses on the efficient electro- and chemical conversion of biomass-derived renewable energy.

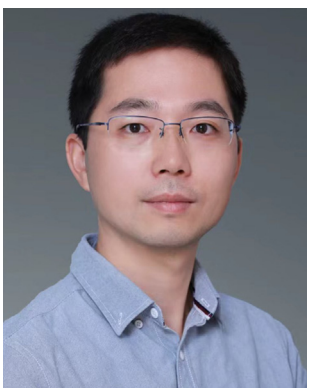

Shunji Xie

Shunji Xie received his BSc and MSc degrees from Hunan University of China in 2008 and 2011, and obtained his PhD degree from Xiamen University in 2014. He then carried out postdoctoral research at the Collaborative Innovation Center of Chemistry for Energy Materials (iChEM). He is currently a full professor at the College of Chemistry and Chemical Engineering of Xiamen University. His research interests focus on photocatalysis and electrocatalysis for C1 and sustainable chemistry, including CO_2 reduction, CH_4 oxidation, biomass conversion and ethylene glycol synthesis.

tence of primary, secondary, tertiary, and furan C–H bonds in biomass molecules necessitates the development of site-selective catalytic systems. In recent years, transition metal-catalyzed C–H bond activation has become a research focus due to its precise directional activation capability and high atom utilization efficiency.[13,32,33] The following sections systematically elucidate the mechanisms of oxidation reactions, with a particular emphasis on the application of electrocatalysis in the activation of C–H bonds in key biomass platform molecules such as glucose, glycerol, and 5-hydroxymethylfurfural (HMF).

2.1 Glucose oxidation: C1/C6 selective carboxylation

Glucose, as the most abundant monosaccharide derived from biomass,[34] serves as a pivotal platform molecule for synthesizing high-value chemicals such as gluconic acid (GLUA) and glucaric acid (GA). The electrochemical valorization of glucose hinges on the site-selective activation of its C–H bonds, particularly at the C1 aldehyde and C6 hydroxymethyl groups.[35–37] This precise bond activation enables the synthesis of target products with significantly enhanced market value compared to raw glucose.[38] However, the intrinsic chemical similarity of C–H bonds and competing over-oxidation pathways pose formidable challenges.[39] The core of the electrocatalytic strategy lies in the synergistic design of catalysts and reaction systems to differentiate and activate specific C–H bonds under mild conditions.

The electrocatalytic oxidation of glucose to GLUA and GA proceeds *via* a sequential C–H activation mechanism, as illustrated. This process can be dissected into two distinct stages, each with its own energetic and kinetic considerations (Fig. 2a). The initial oxidation targets the C1 aldehyde group, a step that typically serves as the rate-determining stage. This process occurs at relatively low potentials on metallic active sites such as Pt^0 or Au^0 through a PCET mechanism, leading to the formation of a gluconolactone intermediate that subsequently hydrolyzes to gluconic acid.[42,43] The main challenge at this stage lies in suppressing competing reactions, including glucose isomerization and C–C bond cleavage.[3,42] The subsequent stage involves oxidation of the C6 hydroxymethyl group, which demands higher potentials that generally coincide with the formation of surface metal oxides like PtO_x.[45] This second oxidation faces a different primary constraint—the strong chemisorption of the glucaric acid product that can poison catalytic active sites.[46,47] Consequently, effective catalysts for this stage must not only cleave the C–H bond but also ensure efficient product desorption.[48] Essentially, an optimal catalyst must successfully navigate these two contrasting energy landscapes, enabling efficient

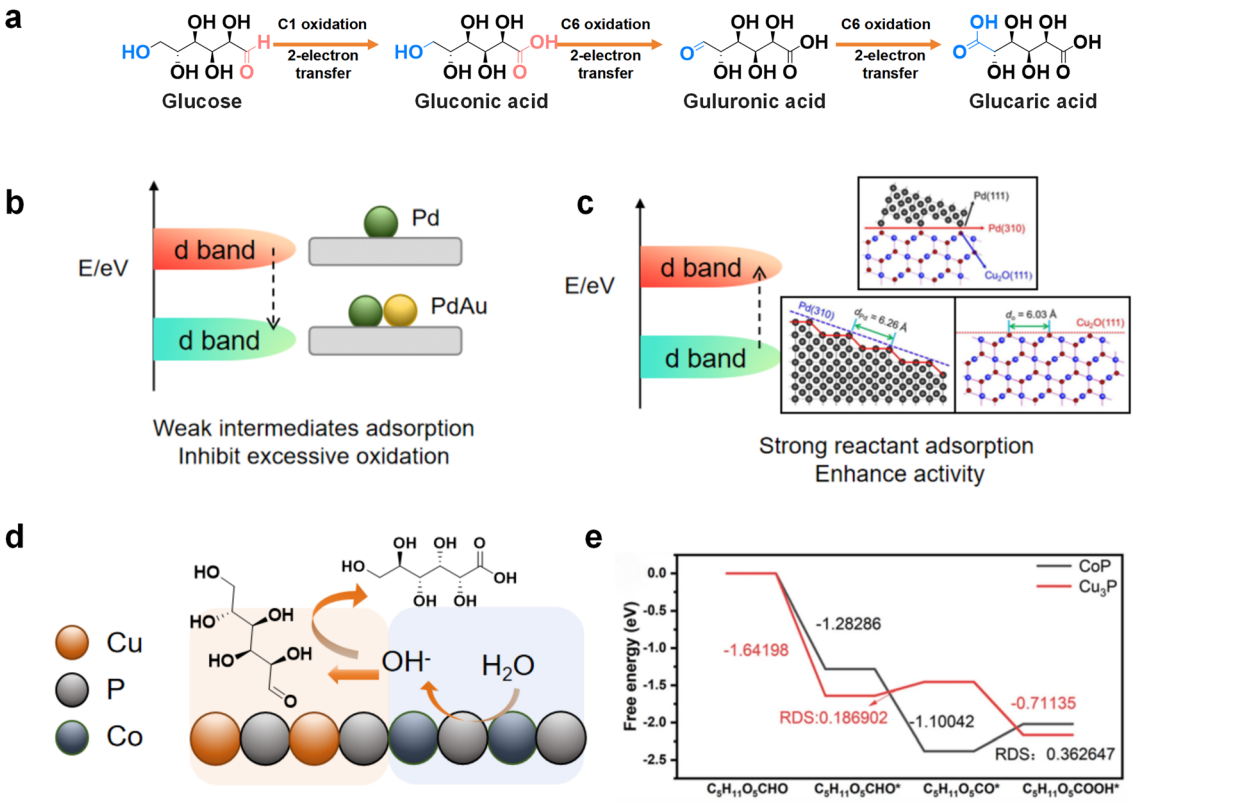

Fig. 2 (a) Schematic illustration of the reactions occurring in the electrochemical oxidation of glucose. (b) PdAu electronic structure modulation. (c) Electronic effect of the Pd/Cu_2O heterojunction; reproduced from ref. 40 with permission from Elsevier, copyright 2019. (d) The dual active sites of CuCoP synergistically catalyze the oxidation of glucose. (e) Glucose oxidation free energy on CuCoP and CoP; reproduced from ref. 41 with permission from Springer Nature, copyright 2025.

first C–H bond activation at low overpotentials while simultaneously resisting deactivation during the more challenging second oxidation step.

To overcome the challenges associated with the sequential activation of C–H bonds, advanced catalyst design has converged on three interconnected strategies: electronic structure modulation, the creation of synergistic interfaces, and nanostructuring for enhanced mass transport. The first strategy involves fine-tuning the electronic structure of the active metals, primarily by adjusting their d-band center. This optimization directly controls the adsorption strength of reaction intermediates. For instance, introducing Au into a Pd catalyst shifts the d-band center of Pd downward (Fig. 2b). This weaker binding to intermediates effectively suppresses the over-oxidation pathway that would otherwise lead to undesired CO adsorbates and C–C bond cleavage, thereby boosting the selectivity for gluconic acid to 87%.[43] A similar electronic effect can be achieved through doping or by constructing heterojunctions. In a study by Guo *et al.*, lattice mismatch was utilized to design a Pd/Cu_2O catalyst, promoting an upward shift in the d-band center (Fig. 2c). This enhancement increased the glucose adsorption energy, thereby improving the oxidation activity of C–H bonds. DFT calculations revealed that the strain induced by lattice mismatch leads to electron accumulation at the Pd/Cu_2O interface. Additional projected density of states (PDOS) analysis indicated that this electron accumulation shifted the d-band center closer to the Fermi level, strengthening the adsorption capacity for glucose molecules.[40] The second approach focuses on designing catalysts with multiple, spatially distinct active sites that work in concert. A representative example is the CuCoP system. In this structure, Cu_3P sites act as strong adsorption centers for glucose molecules, while neighboring CoP sites generate nucleophilic OH^- species that attack the C–H bonds (Fig. 2d).[41] DFT calculations confirm that this bifunctional synergy significantly lowers the energy barrier for hydrogen removal, forming the $C_5H_{11}O_5CO^*$ intermediate and speeding up C–H bond cleavage (Fig. 2e). Multi-metallic systems further amplify this cooperative effect by providing a broader spectrum of active centers to facilitate the multi-step reaction. Wu *et al.* report a FeCoNiCu layered double hydroxide (LDH) nanosheet catalyst, which achieves high activity and stability in glucose electrooxidation through the synergistic effect of multiple active centers at Cu–Co, Cu–Cu, and Cu–Ni bridge sites. Experimental results show that the catalyst reaches a current density of 100 mA cm^{-2} at 1.22 V *vs.* RHE, with glucose conversion close to 100% and a glucaric acid yield exceeding 90%.[46] The physical architecture of the catalyst is crucial for achieving high current densities. Designing three-dimensional porous frameworks or nanoarray electrodes dramatically increases the electrochemically active surface area and provides shorter diffusion pathways for reactants and products. This structural engineering effectively alleviates mass transport limitations. The three-dimensional porous Cu/Cu_2O structure effectively accelerates mass transport by increasing the electrochemically active surface area (ECSA = 1.34 μF cm^{-2}) and shortening the diffusion path.[45] Similarly, Liu *et al.* prepared NiFe layered double hydroxide nanosheet arrays on three-dimensional nickel foam ($NiFeO_x$-NF). This nanoarray electrode exhibited excellent activity and selectivity toward the anodic oxidation of glucose, achieving a current density of 100 mA cm^{-2} at 1.39 V, with a faradaic efficiency (FE) of 87% and a glucaric acid yield of 83%.[49] Table 1 reveals distinct correlations between applied potential, catalyst composition, and product distribution. First, the degree of oxidation is largely potential-dependent: mild potentials (<0.8 V *vs.* RHE) favor partial oxidation to GLUA, predominantly driven by noble metals (*e.g.*, Pd_3Au_7 at 0.4 V, entry 3). In contrast, deep oxidation to GA generally necessitates elevated potentials (>1.1 V), a regime where transition-metal oxides demonstrate superior stability. Notably, multi-component non-noble systems (*e.g.*, FeCoNiCu-LDH, entry 5) achieve >99% GA selectivity and conversion, significantly outperforming single-component Au catalysts (entries 1 and 2). This trend underscores that rational catalyst design must evolve from optimizing single active sites to integrating electronic modulation with hierarchical nanostructures to maximize yield. From the perspective of catalyst stability (Table 1), both noble metal systems and multicomponent non-noble metal systems exhibit operational stability ranging from several to tens of hours. Common deactivation mechanisms include poisoning of active sites by reaction intermediates (*e.g.*, CO) and oxidation of the active sites themselves under high potentials. For

Table 1 Summary of the performance of representative catalysts for electrochemical glucose oxidation

No.	Catalyst	Electrolyte	Conc. (mM)	Potential (V *vs.* RHE)	Conv. (%)	Sel. (%)	FE (%)	Catalyst stability (h)	Deactivation mechanism	Ref.
1	Au[a]	0.1 M Na_2CO_3	40 (GLU)	~0.6	25	97.6 (GLUA)	—	—	—	42
2	Au[a]	0.1 M NaOH	–(GLUA)	1.1	—	89.5 (GA)	—	—	—	42
3	Pd_3Au_7/C[b]	0.1 M NaOH	100 (GLU)	0.4	67	87 (GLUA)	63.3	6	CO adsorption poisoning	43
4	SC/Au[c]	0.1 M NaOH	100 (GLU)	1.3	57.7	81.5 (GLUA)	—	6	OH^- competitive adsorption	44
5	D-FeCoNiCu-LDH/NF[b]	1.0 M KOH	100 (GLU)	1.22	~100	>99 (GA)	95	50	—	46
6	Pt/CNF[a]	0.1 M H_2SO_4	100 (GLU)	0.78	—	>80 (GLUA)	—	0.5	Oxidation of the active site	50
7	$NiFeO_x$–NF[a]	1.0 M KOH	10 (GLU)	1.3	98.3	83.3 (GA)	87	24	CO adsorption poisoning	49
8	CuCoP[a]	1.0 M KOH	100 (GLU)	1.4	—	—	99.5	—	—	41

GLU: glucose; GLUA: gluconic acid; GA: glucaric acid. [a] H-cell. [b] Flow-cell. [c] Single-cell.

example, Pt/CNF (entry 6) showed activity decay after 0.5 h due to oxidation of active sites, whereas Pd_3Au_7 (entry 3) achieved stable operation for 6 h, as the electronic modulation effect of Au weakened CO adsorption and thus alleviated poisoning-induced deactivation. Designing active centers with resistance to poisoning and oxidation is key to improving the durability of glucose oxidation catalysts. In summary, the design of electrocatalysts for glucose oxidation has evolved from optimizing single active sites to the collaborative regulation of electronic structure, interfacial microenvironments, and mass transport. Electronic structure modulation, as exemplified by PdAu alloys, optimizes the d-band center to balance reactant adsorption and product desorption, which is crucial for enhancing selectivity. Interface engineering, such as in CuCoP systems, creates bifunctional sites that enable simultaneous reactant activation and nucleophile supply, effectively lowering the energy barrier for C–H bond cleavage. Meanwhile, nanostructural engineering, exemplified by 3D porous electrodes, enhances reaction efficiency at high current densities by increasing the specific surface area and shortening mass transport pathways. The integration of these strategies represents the future direction for developing high-performance glucose oxidation catalysts.

Applied potential dictates the catalyst's surface oxidation state. Lower potentials (0.4–0.6 V *vs.* RHE) favor metallic active sites for selective C1 oxidation, whereas higher potentials (>1.1 V *vs.* RHE) promote the formation of metal oxides necessary for C6–H activation, albeit with an increased risk of over-oxidation (Fig. 3a and b).[36] The electrolyte pH simultaneously influences the reaction pathway, as alkaline conditions within the pH 11–13 range provide essential hydroxide ions that function as both proton acceptors and sources of surface oxygen species.[44] However, this alkaline dependence presents a significant trade-off, where excessively basic environments beyond pH 12.5 trigger glucose isomerization and consequently cause substantial selectivity losses (Fig. 3c).[42] Both temperature and substrate concentration further modulate the kinetic–thermodynamic balance of the system. Temperature governs pathway selection through kinetic–thermodynamic competition: at low temperature (5 °C), side reactions are suppressed, achieving >97% selectivity for C6 oxidation, but the conversion remains low (25%) due to slow kinetics. Conversely, high temperature (50 °C) increases conversion to 48.5%, yet accelerates C–C bond cleavage, leading to a sharp decline in selectivity, revealing an inherent trade-off in reaction conditions (Fig. 3d).[42] Similarly, once the substrate concentration surpasses a certain saturation threshold, the reaction transitions from being concentration-limited to active-site-limited (Fig. 3e).[51] Consequently, optimizing these reaction conditions requires identifying an operational window where all parameters synergistically enhance rather than compromise the catalyst's intrinsic activity and selectivity, rather than simply maximizing individual parameters. The identified optimal operating window for electrocatalytic glucose oxidation is highly constrained: low potentials yield sluggish kinetics, high potentials cause over-oxidation, high pH triggers isomerization, low pH limits OH^- formation, and substrate concentration must be precisely balanced. This demanding set of conditions falls short of the high-current, high-concentration benchmarks necessary for practical industrial application.

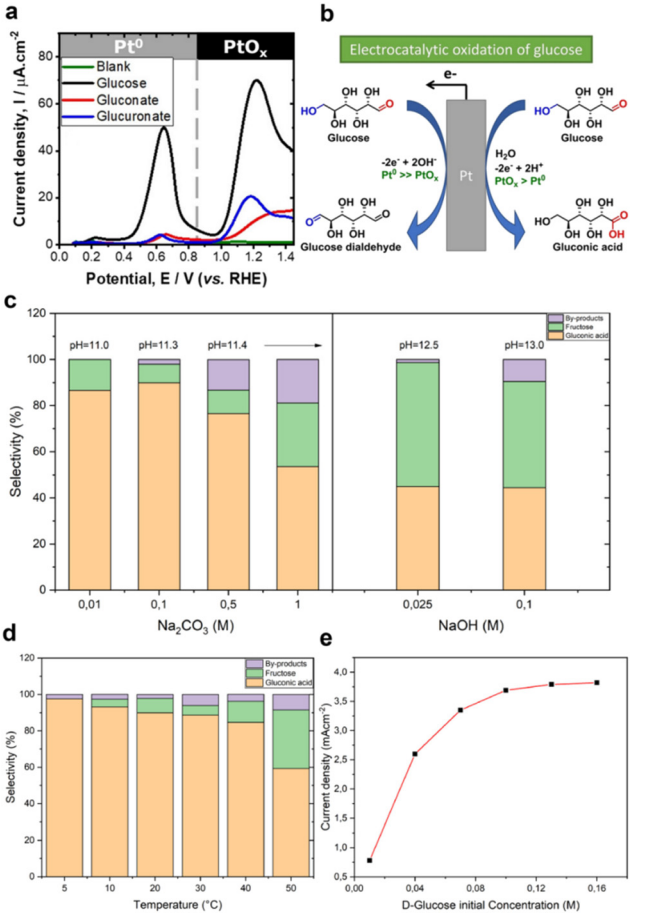

Fig. 3 (a) Blank LSV and LSV of 0.1 M glucose, 0.1 M gluconate, and 0.1 M glucuronate in 0.2 M PBS (pH = 7) on a polycrystalline Pt electrode recorded at a scan rate of 1 mV s^{-1}. The potential windows 0–0.85 V and >0.85 V *vs.* RHE correspond to Pt^0 and PtO_x, respectively; reproduced from ref. 36 with permission from Wiley-VCH GmbH, copyright 2023. (b) Schematic diagram of the influence of different Pt species on the products of electrocatalytic oxidation of glucose at the Pt electrode; reproduced from ref. 36 with permission from Wiley-VCH GmbH, copyright 2023. (c) Influence of pH on the selectivity to gluconic acid (orange), fructose (green) and by-products (violet) for the oxidation of 0.04 M glucose on Au at 20 °C after 24 h; reproduced from ref. 42 with permission from Elsevier, copyright 2021. (d) Dependence of the selectivity to gluconic acid (orange), fructose (green) and by-products (violet) on the reaction temperature for the oxidation of 0.04 M glucose in 0.1 M Na_2CO_3 for 24 h; reproduced from ref. 42 with permission from Elsevier, copyright 2021. (e) Current density response to the variation of initial glucose concentration derived from the respective cyclic voltammogram at 10 mV s^{-1} (Na_2CO_3 0.1 M); reproduced from ref. 42 with permission from Elsevier, copyright 2021.

Beyond catalyst design, reactor engineering plays a crucial role in modulating mass transport and residence time. Optimizing reactor configurations offers a vital pathway to overcome conversion bottlenecks, thereby suppressing side

reactions and improving selectivity. In a representative study, Bin *et al.* utilized a continuous-flow reactor with a MnO_2-decorated tubular porous titanium electrode. The flow-through design mitigated mass transport limitations and ensured fast product desorption, resulting in near 100% glucose conversion and 99% selectivity for GA/GLUA in neutral electrolyte. Furthermore, the GA/GLUA ratio could be readily regulated by varying the current density, highlighting the system's exceptional tunability.[52] Similarly, Düzenli *et al.* demonstrated efficient direct glucose oxidation in a continuous-flow fuel cell using Au-, Cu-, and Pt-doped graphene SACs. Mechanistic insights suggest that Cu sites promote a single-step pathway to gluconolactone, whereas Au and Pt sites follow a two-step mechanism. Meanwhile, Ni, Pd, and Zn dopants could initiate deprotonation but failed to yield lactones. These results demonstrate that high selectivity relies on the interplay between the reactor's mass transport capabilities and the thermodynamic favorability of the active sites.[53]

2.2 Glycerol oxidation: multi-C–H site regulation

Glycerol, as a byproduct of large-scale biodiesel production, has exceeded tens of millions of tons annually.[54] Its low market price (0.24–0.6 USD per kg) urgently requires value-added transformation to enhance economic viability. As a C3 platform molecule, glycerol can be selectively oxidized to produce high-value chemicals such as glyceric acid (GLA) and dihydroxyacetone (DHA), increasing its market value by over a hundredfold.[55,56] Traditional thermocatalytic or enzymatic methods face challenges such as high energy consumption and poor selectivity.[57,58] In contrast, electrocatalysis, under ambient temperature and pressure, enables precise activation of C–H bonds and preservation of C–C bonds by modulating potential and interface structures, thereby breaking through the selectivity bottleneck for C3 products. This section systematically explores the competitive activation of terminal and secondary hydroxyl C–H bonds in glycerol electrooxidation, the overoxidation behavior of intermediates, and the mechanisms for preserving C3 products, while summarizing strategies for catalyst design and reaction optimization.

2.2.1 Selective oxidation of primary alcohols to glyceric acid. The electrooxidation of glycerol to GLA hinges on the selective activation and dehydrogenation of the primary hydroxyl group's C–H bond. On platinum-based catalysts, the generally accepted pathway involves a two-step, $2e^-$ process: initial oxidation to glyceraldehyde (GLYD), followed by further oxidation to GLA (Fig. 4a).[59,60] The primary challenge is suppressing C–C bond cleavage, which is often triggered by strongly adsorbed intermediates (*e.g.*, *CO–CHOH–CH_2OH), leading to undesired C1/C2 products like formic and glycolic acid.[61,62] In contrast, Au-based catalysts, with their weaker adsorption of intermediates, inherently suppress C–C cleavage but rely on alkaline conditions to facilitate glycerol deprotonation, which lowers the C–H cleavage barrier.[63,64] The reaction path is also highly sensitive to the catalyst's surface structure; for instance, Pt(111) facets favor GLA formation, while Pt(100) tends to stop at GLYD, underscoring the critical role of crystallographic orientation.[61,65]

In order to optimize the C–H bond activation efficiency and inhibit side reactions, the catalyst design strategy focuses on electronic structure regulation, interface engineering, and dynamic surface management. The C–H dehydrogenation energy barrier can be reduced by regulating the d-band center. Wang *et al.* designed a PtCuCoNiMn high-entropy alloy catalyst that enhanced glycerol electro-oxidation through multi-element-induced lattice strain. The catalyst achieves a 5.4-fold higher current density than Pt/C at 0.8 V (*vs.* RHE). DFT calculations showed a downshifted Pt d-band center, weakening oxygenate adsorption and suppressing over-oxidation (Fig. 4b and c). *In situ* surface-enhanced Raman spectroscopy data (SERS) show that the oxidation of Co, Ni, and Mn in PtCuCoNiMn commences in the first CV cycle and is nearly complete after ten cycles (Fig. 4d). These preferentially formed higher valence states create "oxidation buffer sites", which protect the Pt active centers, ensuring the catalyst's sustained activity and stability.[66] A similar effect is achieved in the Pt/CeNC catalyst, where single-atom Ce^{3+} promotes electron transfer to Pt. This likewise downshifts the d-band center, thereby weakening GLA adsorption, facilitating product desorption, and achieving a remarkable turnover frequency of 233 mmol h^{-1} g_{pt}^{-1}.[68] Beyond intrinsic electronic effects, interface engineering creates bifunctional systems for synergistic catalysis. For example, Pt–Bi_2O_3 nanosheets exhibit electron transfer from the support to Pt, which generates electron-rich Pt sites that suppress C–C cleavage. XPS and XANES/EXAFS (Fig. 4e–g) confirm that electron transfer from Bi_2O_3 to Pt creates electron-rich Pt sites, suppressing C–C cleavage. *In situ* Raman spectroscopy (Fig. 4h) shows decreasing intensity at 1088–1130 cm^{-1} (middle C–OH) with potential, while the 1020–1080 cm^{-1} peak (terminal C–OH) remains stable, indicating preferential oxidation of the middle hydroxyl group in a lying-down adsorption mode. DFT calculations confirm that the lying-down configuration on Pt–Bi_2O_3 exhibits optimal adsorption energy and the highest GLA formation rate. Thus, Bi_2O_3 anchors hydroxyl groups to steer glycerol into a lying-down geometry, enabling terminal-selective oxidation to glyceric acid. Bifunctional interface design serves as an effective strategy to further enhance synergistic effects (Fig. 4i).[67] Similarly, in a Pd–CoFe LDH catalyst, electron donation from Pd to the support creates $Pd^{\delta+}$ species. This weakens the adsorption of poisoning *CO-type intermediates. At the same time, the CoFe LDH component promotes the formation of *OH species at low potentials, which collectively enhances activity and selectivity.[69] Moving beyond static catalyst design, dynamic surface management through operational protocols offers a powerful solution to catalyst deactivation. A prime example is pulsed potential electrolysis applied to Pt catalysts. This technique periodically removes strongly adsorbed intermediates and reduces C–C cleavage, which boosts GLA selectivity from 37.8% to 81.8%.[62] *In situ* FTIR revealed that constant potential caused the accumulation of oxidation intermediates on Pt. Enhanced hydrogen bonding (3100–3700 cm^{-1} and 1644 cm^{-1}) indicated strong adsorption of OH and intermediates, blocking glycerol and OH^- re-adsorption. In pulsed

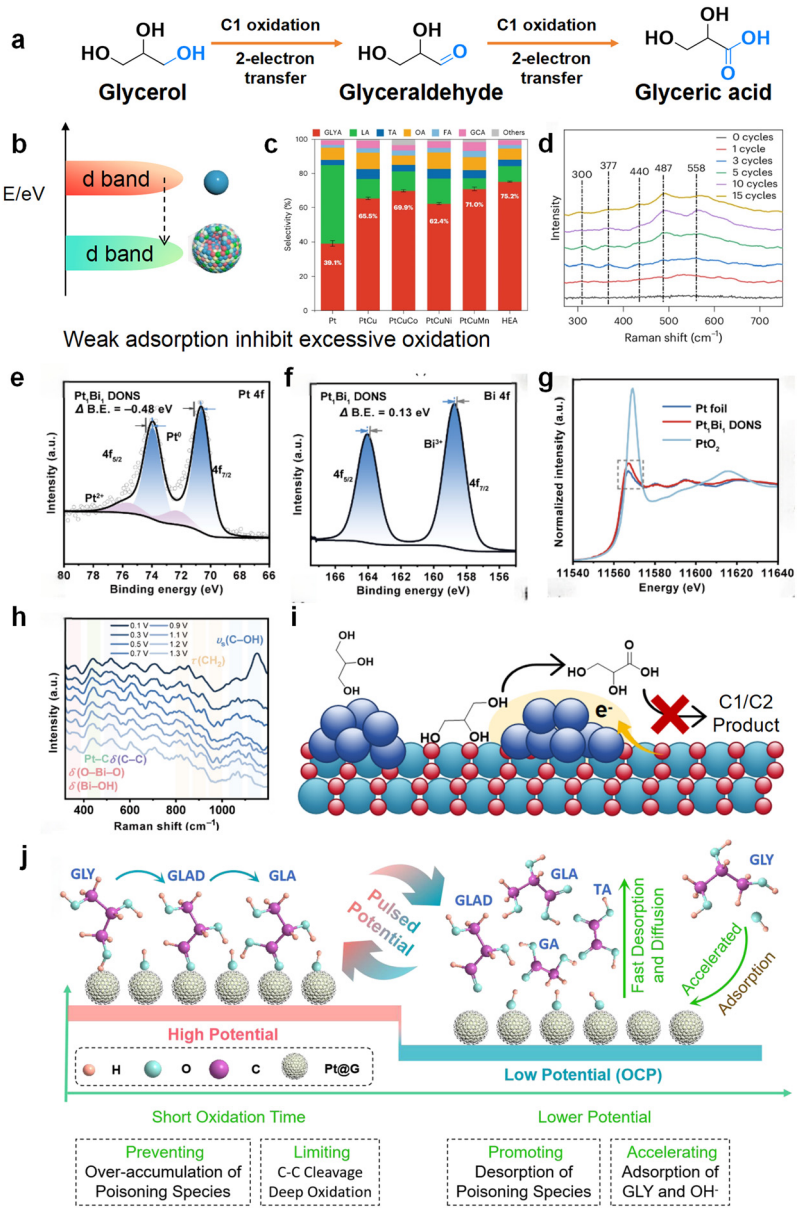

Fig. 4 (a) Reaction pathways for the oxidation of glycerol. (b) The energy band structure of Pt and PtCoNiMn high-entropy alloys. (c) Product distributions at 0.8 V *versus* RHE in 1 M KOH with 0.1 M glycerol over different nanocatalysts; reproduced from ref. 66 with permission from Springer Nature, copyright 2025. (d) *In situ* SERS spectra of PtCuCoNiMn during CV activation. Raman peaks at 300 and 487 cm^{-1} (Cu–O), 377 cm^{-1} (Mn–O (H)), 440 cm^{-1} (Co–O), and 558 cm^{-1} (Ni–O) confirm the existence of oxidized Cu^{+}/Cu^{2+}, Mn, Co, and Ni species, respectively. The progressive increase in the Co–O peak area (440 cm^{-1}) over CV cycles 1–15 indicates continued cobalt oxidation; reproduced from ref. 66 with permission from Springer Nature, copyright 2025. (e) Pt 4f XPS spectrum and (f) Bi 4f XPS spectrum of Pt/Bi_2O_3; reproduced from ref. 67 with permission from Elsevier, copyright 2025. (g) Normalized Pt L3-edge XANES for Pt foil, Pt/Bi_2O_3, and PtO_2; reproduced from ref. 67 with permission from Elsevier, copyright 2025. (h) Electrochemical *in situ* Raman spectral evolution of Pt/Bi_2O_3 at different potentials in 1 mol L^{-1} KOH + 0.5 mol L^{-1} glycerol; reproduced from ref. 67 with permission from Elsevier, copyright 2025. (i) Mechanism of the GOR over Pt/Bi_2O_3. (j) Schematic of the pathways of PE-based GEOR. GLY glycerol, GLAD glyceraldehyde, GLA glyceric acid, TA tartronic acid, GA glycolic acid; reproduced from ref. 62 with permission from Springer Nature, copyright 2024.

mode, intermediate accumulation decreased, and OH coverage increased, promoting GLA desorption. *Quasi-in situ* XPS confirmed that constant potential oxidized Pt to PtO_x, while pulsed electrolysis maintained metallic Pt, suppressing catalyst over-oxidation and preserving activity (Fig. 4j). Collectively, these strategies highlight a paradigm shift from seeking single-component catalysts to designing integrated systems where electronic structure, interfacial synergy, and operational dynamics are controlled to master C–H bond activation. The core challenge in synthesizing glyceric acid lies in suppressing C–C bond cleavage and over-oxidation of intermediates. Successful strategies commonly rely on weakening the adsorp-

tion strength of intermediates at active sites, which can be achieved by constructing electronic effects or designing dynamic operation protocols.

The reaction conditions exert a decisive influence on both the pathway and efficiency of C–H bond activation, necessitating synergistic optimization with catalyst characteristics. Potential critically regulates the binding strength of intermediates *via* the Gibbs adsorption energy relationship ($\Delta G \propto F\Delta E$). Specifically, lower potentials (0.6–0.8 V *vs.* RHE) suppress C–C bond cleavage, thereby achieving GLA selectivity exceeding 80%. Conversely, higher potentials (>0.9 V) promote deep oxidation to C1 products.[67,70] Furthermore, the pH value modulates the reaction pathway by altering reactant speciation and surface coverage. Alkaline conditions (pH > 13) facilitate glycerol deprotonation to form the alkoxide species (GLY-O^-), which significantly lowers the energy barrier for C–H bond cleavage. Consequently, GLA selectivity increases by over 40% compared to acidic environments.[63,71] Furthermore, a high hydroxide ion concentration boosts the surface coverage of nucleophilic $*OH_{ads}$ species, which accelerates the crucial dehydrogenation steps.[69] Finally, managing substrate concentration and mass transfer is vital for maintaining high efficiency. An optimal glycerol-to-catalyst ratio must be maintained, as moderate concentrations facilitate the desorption of GLA and minimize its subsequent over-oxidation.[70] Excessively high local glycerol concentrations, particularly those exceeding 0.6 M, can trigger undesirable side reactions such as the Cannizzaro rearrangement, leading to lactate formation.[62,71] Therefore, engineering catalyst architectures, such as 3D porous electrodes, to enhance mass transfer of reactants and products, is a key strategy for further improving overall performance. Table 2 highlights the impact of electrolyte pH, operation mode, and catalyst composition on GLA selectivity. Data analysis reveals that the field remains predominantly dependent on noble-metal-based systems (*e.g.*, Pt, Pd, and Au), which constitute nearly all representative catalysts listed. Notably, the integration of multi-metallic components appears to be a key driver for performance enhancement. For instance, multi-element PtCuCoNiMn-EC (entry 6) achieves 75.2% selectivity, surpassing simpler noble-metal configurations like PdFe/rGO (entry 1, 21.7%) or Pd-OCTA (entry 5, 42.0%). Furthermore, alkaline conditions generally yield higher selectivity than acidic media, as evidenced by the lower performance of Pt/C in H_2SO_4 (entry 11, 67.3%) compared to most of its alkaline counterparts (entries 2, 6 and 8). Catalyst stability is a key indicator for practical applications. As shown in Table 2, stability can be significantly improved by introducing multiple metal components or constructing strong metal–support interactions. For example, the transition metal oxide layer in PtCuCoNiMn-EC (entry 6) serves as an "oxidation buffer site", protecting the Pt active centers and enabling stable operation for 210 h in an MEA electrolyzer. Pt/CeNC (entry 7) and Pd–CoFe LDH (entry 8) also achieved long-term operation for 150 h and 200 h, respectively, through single-atom modulation by Ce^{3+} and synergistic effects of the LDH support. Deactivation in these systems is often related to the strong adsorption and accumulation of reaction intermediates. Dynamic strategies, such as pulsed potential, can effectively desorb these intermediates and restore activity, providing an operational solution to mitigate deactivation.

In summary, the essence of glycerol electrooxidation to synthesize glyceric acid is to precisely regulate the initial C–H activation step. The dehydrogenation of the primary hydroxyl group to form GLYD is the rate-determining step, and the adsorption strength of the intermediate determines the risk of C–C fracture.[59,61] By optimizing the C–H activation energy barrier through the electronic effect (d-band center down),[66,68] interface synergy (metal–support interaction),[67,69] and

Table 2 Summary of the performance of representative catalysts for electrochemical glycerol oxidation to glyceric acid

No.	Catalyst	Electrolyte	Conc. (mM)	Potential (V *vs.* RHE)	Conv. (%)	Sel. (%)	FE (%)	Catalyst stability (h)	Deactivation mechanism	Ref.
1	PdFe/rGO[a]	1.0 M KOH	100	0.8	48.5	21.7	96.5	—	Progressive oxidation of active sites and intermediate adsorption	60
2	Pt@G[a]	1.0 M KOH	20	Pulse: 0.3/0.7	59.4	81.8	—	—	Progressive oxidation of active sites and intermediate adsorption	62
3	Pt_3Au_7@Ag[a]	0.5 M KOH	500	0.7	—	34.5	—	—	Intermediate adsorption	63
4	PdAu@Ag[a]	0.5 M KOH	500	0.9	—	15.4	—	—	Intermediate adsorption	64
5	Pd-OCTA[a]	1.0 M KOH	100	0.86	82 (60 °C)	42.0	—	—	Intermediate adsorption	65
6	PtCuCoNiMn-EC[b]	1.0 M KOH	100	0.8	—	75.2	—	210	Progressive oxidation of active sites	66
7	Pt/CeNC[a]	1.0 M KOH	600	0.87	87.9	58.8	—	150	Intermediate adsorption	68
8	Pd–CoFe LDH[b]	1.0 M KOH	500	0.9	—	72.8	—	200	Intermediate adsorption	69
9	Pt–CeO_2/CNT[a]	1.0 M KOH	100	0.9	85.5	59.0	—	20	Intermediate adsorption	70
10	Au–CeO_2/CNT[a]	1.0 M KOH	500	1.12	99.7	50.0	—	20	Intermediate adsorption	71
11	Pt/C[a]	0.5 M H_2SO_4	100	0.9	64.1	67.3	—	120	—	72

[a] H-cell. [b] Membrane electrode assembly flow electrolyzer (MEA).

dynamic strategy (pulse potential),[62] >80% GLA selectivity can be achieved while improving the activity. A low potential, alkaline environment and moderate substrate concentration are the key conditions to maintain high C3 selectivity. Techno-economic analysis confirmed that the production cost of glyceric acid in the electrocatalytic pathway ($ 2.30 per kg) was 53% lower than that in thermal catalysis.[72]

2.2.2 Selective oxidation of secondary alcohols to dihydroxyacetone (DHA). The essence of the electrocatalytic conversion of glycerol to the high-value-added product DHA lies in the selective activation of the C–H bond in the secondary hydroxyl group of the glycerol molecule, while effectively suppressing the oxidation of the primary hydroxyl groups and C–C bond cleavage reactions (Fig. 5a). This process is initiated by the oriented adsorption of the glycerol molecule onto the catalyst surface: the ideal adsorption conformation requires the secondary hydroxyl group to preferentially access the active site, where it undergoes dehydroxidation to form the target product DHA. It is noteworthy that DHA is prone to spontaneous isomerization to GLYD under strongly alkaline conditions. GLYD can then be further oxidized to form GLA or undergo C–C bond cleavage, producing low-carbon byproducts such as formic acid.[73] Therefore, the central challenges are twofold: achieving exceptional selectivity for the secondary C–H bond activation and ensuring the subsequent stability of DHA formed. For instance, on the CoO_x catalyst, the highly oxidizing Co^{3+}/Co^{4+} species generated at high potentials simultaneously attack the –OH and –C═O groups, resulting in a significant decrease in DHA selectivity from 60% to 40%.[78] Consequently, successful DHA synthesis hinges on catalysts engineered for specific secondary C–H activation and DHA stabilization.

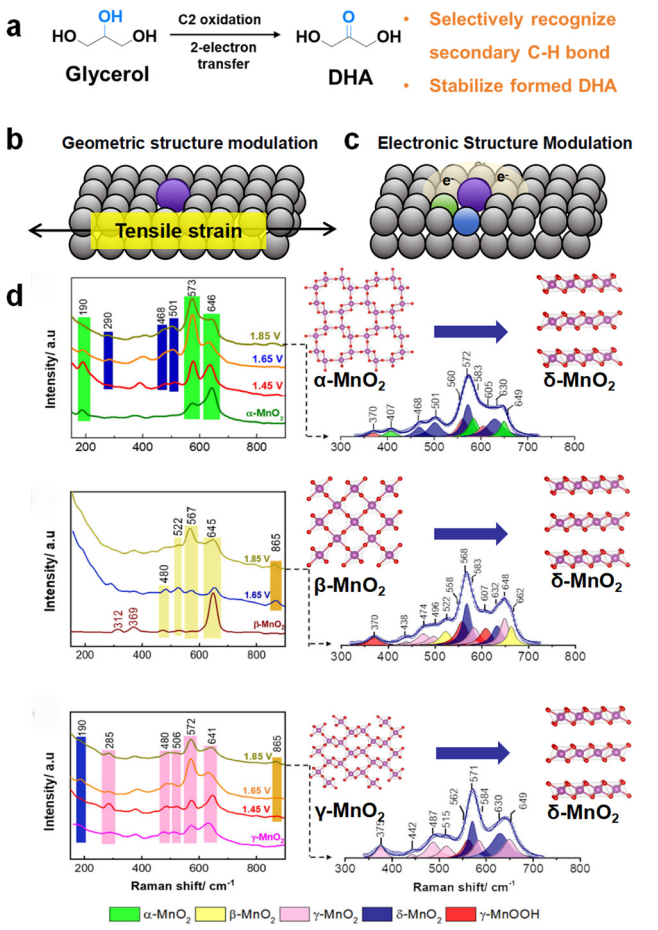

Fig. 5 (a) Reaction pathway for the electrocatalytic oxidation of glycerol to dihydroxyacetone (DHA). Schematics illustrating the (b) geometric and (c) electronic structure modulation strategies for DHA-selective catalysts. (d) *Operando* Raman spectra at different applied potentials and Lorentz fitting peaks at 1.85 V *vs.* RHE for α-MnO_2, β-MnO_2, and γ-MnO_2; reproduced from ref. 76 with permission from the American Chemical Society, copyright 2023.

The design of highly efficient catalysts for glycerol oxidation must satisfy two core requirements: selective adsorption of the secondary hydroxyl group and suppression of C–C bond cleavage activity, with current research strategies primarily divided into noble metal and non-noble metal systems. Noble metal catalysts achieve selectivity through geometric and electronic structure modulation. For instance, Lee *et al.* developed a PtSb/C catalyst. The incorporation of Sb atoms induces lattice strain (Fig. 5b). This creates a unique geometric configuration that selectively interacts with the secondary hydroxyl group while simultaneously weakening C–C bond cleavage, resulting in a DHA selectivity of 68%.[77] A similar outcome is achieved through electronic structure modulation, as demonstrated by an N/P co-doped Pd/CNT (Pd/NPCNT) catalyst, where optimizing palladium's electron density enhances its affinity for the secondary hydroxyl group and increases DHA selectivity to 76.7% (Fig. 5c).[75] Non-noble metal catalysts primarily leverage the dynamic surface reconstruction properties of variable valence metal oxides. This method capitalizes on the *in situ* transformation of metal oxides under operational conditions to generate highly selective, transient active phases. A notable example is MnO_2, where a potential-induced phase transition from the γ-phase to the δ-phase at high potentials suppresses C–C bond cleavage and enhances DHA selectivity to 46%. *Operando* studies (Fig. 5d) confirm that this structural evolution is paramount to performance, with the γ-MnO_2 precursor undergoing the most efficient reconstruction into the active phase.[76] Collectively, these strategies underscore a fundamental design logic for DHA catalysts. This goal is achieved by constructing a local environment, through static site geometry or dynamic phase creation, that provides both steric–electronic discrimination against the primary hydroxyl and stabilization of the DHA ketone group.

Reaction conditions significantly influence the C–H activation efficiency and DHA selectivity by regulating the state of catalyst active sites and the adsorption behavior of glycerol molecules. The applied potential exerts a dual influence. It can enhance C–H activation kinetics but also drive over-oxidation. For example, DHA selectivity reaches 60% at 1.5 V *vs.* RHE over CoO_x, but at 1.7 V *vs.* RHE, the dominance of Co^{3+}/Co^{4+} species leads to deep oxidation of DHA to GLA.[78] Conversely, for MnO_2, high potential is beneficial as it triggers

the selective α → δ phase transition.[74] The electrolyte pH is arguably the most critical factor for DHA stability. Mildly alkaline conditions (pH ~ 9) are optimal, as they facilitate the reaction without triggering the base-catalyzed isomerization of DHA to GLYD, which devastates selectivity in strong alkali conditions (pH 13). In $Na_2B_2O_7$ buffer at pH 9, DHA remains stable on CuO with a selectivity of 60%, whereas under strong alkaline conditions (pH 13) the selectivity is below 3%. In acidic media (*e.g.*, 0.5 M H_2SO_4), catalysts such as PtSb/C are required to resist H^+ poisoning of active sites and sustain DHA generation.[74,77] While temperature primarily accelerates conversion without markedly affecting the C–H activation barrier, it highlights that DHA selectivity is primarily controlled by the catalyst's intrinsic properties and electrolyte pH.[77] Table 3 reveals that the selective oxidation of glycerol to DHA necessitates a fundamentally different reaction environment and catalyst design compared to GLA synthesis. The data underscore the critical role of the electrolyte pH. Unlike strong alkaline media (*e.g.*, KOH) required for GLA, Table 3 shows that near-neutral or mildly alkaline conditions, such as 0.1 M $Na_2B_4O_7$ (entries 1, 2, 4 and 6), are predominantly used to stabilize DHA and suppress isomerization. Furthermore, DHA production generally requires significantly higher operating potentials; for instance, CuO (entry 1) and CoO_x (entry 6) achieve 60% selectivity but at elevated potentials of 2.05 V and 1.5 V, respectively. This contrast highlights that while noble metals like Pd (entry 3) or Pt (entry 5) can drive the reaction at lower potentials (~1.0 V), achieving high DHA selectivity often involves leveraging Earth-abundant metal oxides in specialized local environments to precisely activate the secondary C–H bond. Compared to GLA synthesis, studies on the stability of DHA electrosynthesis catalysts are relatively limited (Table 3). Deactivation of non-precious metal oxide catalysts, such as MnO_2 and CoO_x, is often associated with surface reconstruction or phase transformation under high potentials. While such reconstruction can sometimes facilitate the formation of selective active phases, excessive changes may lead to deactivation. For noble-metal catalysts like PtSb/C, deactivation primarily stems from the strong adsorption of reaction intermediates. Overall, developing catalysts that combine high selectivity with long-term stability, particularly non-precious metal systems capable of operating under mild potentials, remains a key research focus for DHA synthesis.

The optimization of reactor design represents a critical lever for precisely tailoring product selectivity. Gaines *et al.* investigated this *via* a multi-parameter optimization of glycerol electro-oxidation, utilizing a flow electrolysis cell combined with response surface methodology (RSM). The findings revealed a divergence in product behavior: C1 products (formic acid) are more amenable for achieving simultaneous high current density and selectivity in flow systems, whereas the selectivity for C3 products (glyceric/lactic acid) is significantly compromised under high-current regimes. This highlights that although flow reactors offer control over product distribution through enhanced mass transfer and tunable residence times, the sensitivity of specific products to these parameters varies substantially.[79] To address the challenge of selectively targeting high-value C3 products, Setiawan *et al.* utilized a stirred slurry electrocatalytic reactor featuring a Pt/C catalyst to realize the selective oxidation of glycerol to glyceraldehyde. Under mild conditions at 30 °C, the system achieved a selectivity of 36.8% and a faradaic efficiency of 37.4%. Notably, this design not only boosted the anodic selectivity and efficiency for C3 species but also realized the concurrent valorization of glycerol and lignin derivatives by coupling the process with the cathodic reduction of guaiacol.[80]

2.3 5-Hydroxymethylfurfural oxidation: C–H oxidation of furan ring side chains

5-Hydroxymethylfurfural (HMF) is an important biomass platform compound, mainly derived from the dehydration of monosaccharides like glucose and fructose, as well as polysaccharides such as cellulose and starch.[5,81] Its molecular structure contains multiple functional groups, including a furan ring, a hydroxymethyl group, and an aldehyde group, giving it the potential to be converted into high-value chemicals such as 2,5-furandicarboxylic acid (FDCA), 5-hydroxymethyl-2-furancarboxylic acid (HMFCA), and 2,5-diformylfuran (DFF).[82–84] Among these, FDCA can serve as a bio-based polymer monomer, replacing terephthalic acid in the synthesis of polyesters and polyamides. There is strong market demand and it has significantly higher value than HMF.[85] Electrocatalytic technology offers a

Table 3 Summary of the performance of representative catalysts for electrochemical glycerol oxidation to DHA

No.	Catalyst	Electrolyte	Conc. (mM)	Potential (V *vs.* RHE)	Conv. (%)	Sel. (%)	FE (%)	Catalyst stability (h)	Deactivation mechanism	Ref.
1	CuO[a]	0.1 M $Na_2B_4O_7$	100	2.05	—	60.0	—	—	—	73
2	MnO_2 [a]	0.1 M $Na_2B_4O_7$	100	2.05	—	46.0	—	—	Surface reconstruction induced by potential	74
3	Pd/NPCNT[a]	0.5 M KOH	500	1.08	—	42.5	76.71	—	Intermediate adsorption	75
4	γ-MnO_2 [a]	0.1 M $Na_2B_4O_7$	100	1.85	—	50.0	59.7	—	Surface reconstruction induced by potential	76
5	PtSb/C[a]	0.5 M H_2SO_4	100	0.997	90.3	61.4	—	50	Intermediate adsorption	77
6	CoO_x [a]	0.1 M $Na_2B_4O_7$	100	1.5	—	60.0	49.4	3	Intermediate adsorption	78

[a] H-cell.

green pathway for the valorization of HMF, thanks to its mild reaction conditions, high reaction selectivity, and the ability to be coupled with other electrochemical reactions.

The electrocatalytic oxidation of HMF (HMFOR) typically involves multiple electron transfers and a multi-step reaction pathway. It mainly includes two initial competing pathways (Fig. 6a). The first pathway is the preferential oxidation of the aldehyde group. This forms HMFCA. HMFCA is then converted into FDCA. The second pathway is the preferential oxidation of the hydroxyl group. This forms DFF. DFF is further oxidized to FFCA and FDCA.[86,87] The reaction pathway is controlled by the catalyst properties, applied potential, and pH value. Neutral conditions favor the selective oxidation of the aldehyde group to form HMFCA. In contrast, alkaline conditions promote the oxidation of the hydroxyl group and the formation of deep oxidation products.[87,88] The activation of the C–H bond is a key step in the reaction. Its efficiency and selectivity directly affect the final product distribution.[88,89] Research shows that high-valence metal species are the core active centers for C–H bond activation. For example, under neutral conditions, CoOOH specifically activates the aldehyde C–H bond. In alkaline media, species like NiOOH and CuOOH promote C–H bond cleavage through strong electron extraction. This significantly lowers the reaction energy barrier.[88–90]

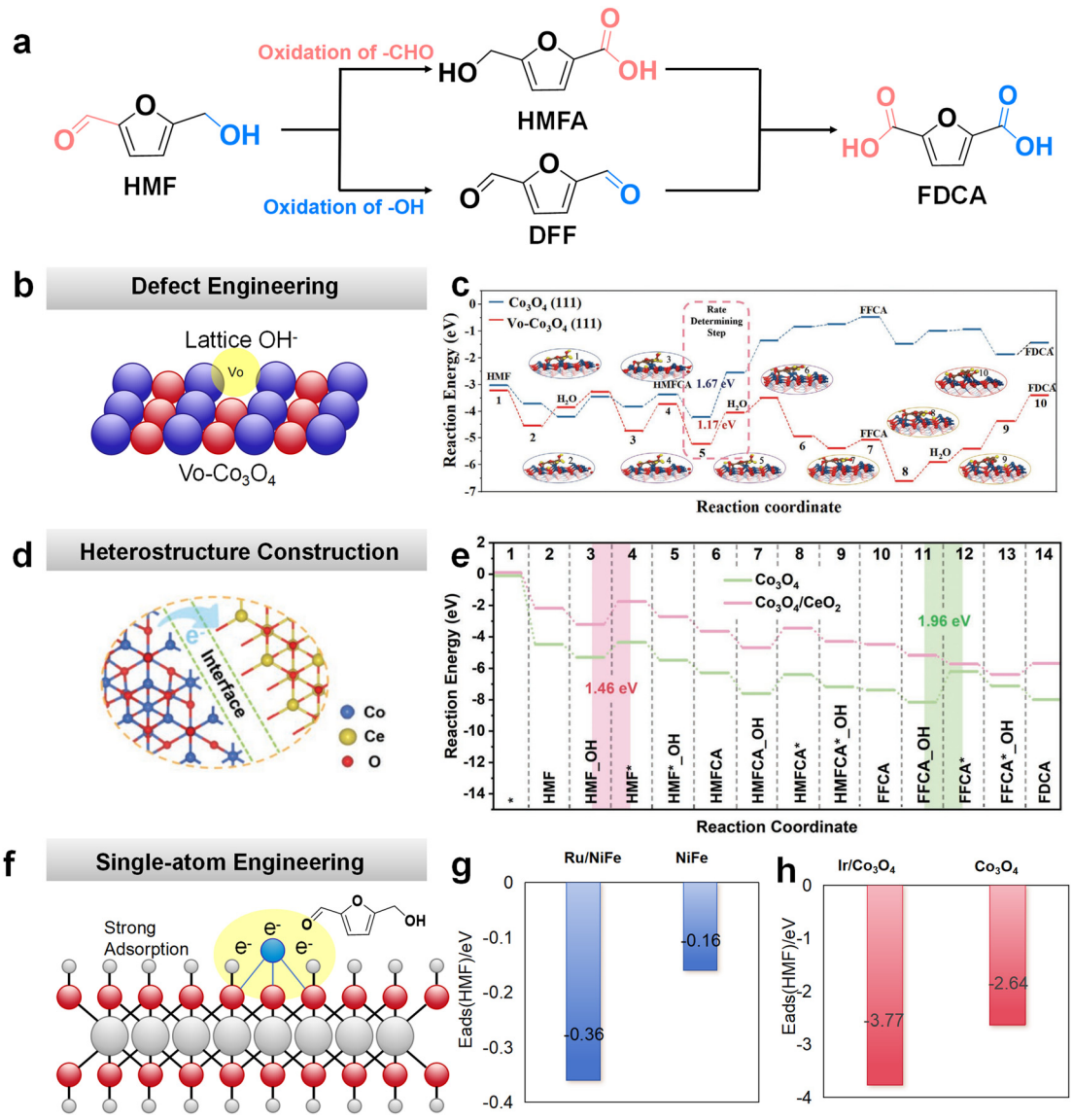

Fig. 6 (a) Reaction pathways for the oxidation of glycerol. (b) Schematic diagram of defect engineering for Vo-Co_3O_4. (c) Free energies of the HMFOR step *via* path I on Vo-Co_3O_4 and Co_3O_4; reproduced from ref. 91 with permission from Wiley-VCH GmbH, copyright 2021. (d) Schematic diagram of the interfacial electronic structure for NF@Co_3O_4/CeO_2. (e) Free energies of the HMFOR step on Co_3O_4 and Co_3O_4/CeO_2, and adsorption configurations of HMFOR intermediates on Co_3O_4/CeO_2; reproduced from ref. 92 with permission from Elsevier, copyright 2023. (f) Modulation of the local electronic structure and reactant adsorption *via* single-atom engineering. (g) HMF adsorption energy of Ru/NiFe and NiFe. (h) HMF adsorption energy of Ir–Co_3O_4 and Co_3O_4.

Catalyst structure engineering strategies offer effective pathways to optimize C–H bond activation efficiency in electrocatalytic HMF oxidation. Defect engineering enhances the catalytic activity by introducing oxygen vacancies or cation vacancies. Vo-Co_3O_4 achieved a higher FDCA yield of 91.9% at 1.34 V *vs.* RHE compared to pristine Co_3O_4 (86.7%). *Operando* XAS/XPS analysis revealed that under the reaction potential, Vo-Co_3O_4 exhibited an increased Co valence and a subsequent adjustment in Co–O coordination, indicating that O^- preferentially filled oxygen vacancies to form lattice OH, which subsequently participated in HMF dehydrogenation (Fig. 6b). DFT calculations confirmed that OH^- occupation of Vo sites avoided competitive adsorption with HMF on metal sites. Furthermore, they identified the dehydrogenation of HMFCA to FFCA as the rate-determining step, the energy barrier of which was significantly reduced from 1.67 eV on Co_3O_4 to 1.17 eV on Vo-Co_3O_4 (Fig. 6c), as the lattice OH facilitated more direct coupling with the intermediate.[91] Beyond defect control, heterostructure construction leverages interfacial effects to modulate electron transfer (Fig. 6d). Zhao *et al.* constructed a Co_3O_4/CeO_2 heterojunction that reduced charge transfer resistance and facilitated HMF and OH* co-adsorption, achieving 98.0% HMF conversion and 94.5% FDCA yield. Charge density difference analysis confirmed electron transfer from Co_3O_4 to CeO_2. This interface significantly lowered both the electrode's inner oxidation resistance (R_p) and interface reaction resistance (R_{ct}), enhancing electron transfer. DFT revealed that the rate-determining step shifted from FFCA to FDCA (1.96 eV barrier on Co_3O_4) to HMF to HMFCA (1.46 eV barrier on Co_3O_4/CeO_2) (Fig. 6e), improving the reaction kinetics.[92] Similarly, the CoP–CoOOH heterostructure optimizes reactant adsorption energies *via* its inherent p–n junction effect, thereby boosting the overall reaction kinetics.[93] Another significant approach involves single-atom engineering to maximize atomic utilization efficiency. The introduction of single-atom Ru into $Ru_{0.3}$/NiFe-LDH significantly enhances the HMF adsorption capacity, increasing the FDCA yield from 45.02% with NiFe-LDH to 82.41%. *In situ* Raman spectroscopy confirms the formation of NiOOH on the catalyst surface after the reaction, identifying it as the active species for the HMFOR. Charge density difference maps reveal that Ru incorporation induces electronic restructuring, with electron accumulation around Ru and depletion at adjacent O atoms, indicating Ni → Ru electron transfer through an O-bridge (Fig. 6f). DFT calculations further demonstrate that $Ru_{0.3}$/NiFe exhibits a significantly higher adsorption energy for HMF compared to that for NiFe-LDH (Fig. 6g), and the presence of Ru reduces the dehydrogenation energy barrier for the transformation of $Ni(OH)_2$ to NiOOH, thereby promoting the kinetics of active phase formation.[94] Similarly, Ir–Co_3O_4 with atomically dispersed Ir sites increases the FDCA yield from 90% to 98% by precisely tuning the d-band center of the catalyst, thereby enhancing the binding strength of key intermediates. DFT calculations reveal that the adsorption energy of HMF on Ir–Co_3O_4 (−3.77 eV) is significantly more negative than that on Co_3O_4 (−2.64 eV), indicating stronger adsorption (Fig. 6h). The Ir sites preferentially adsorb the C=C group in HMF rather than the C=O group. This selective adsorption lowers the reaction energy barrier and accelerates the HMFOR process. Furthermore, the introduction of Ir induces a redistribution of electron density at the Co sites, leading to a lower valence state of Co and enhancing the catalyst's affinity for conjugated cyclic structures.[95] These structural modulation techniques collectively demonstrate how targeted material design can overcome kinetic limitations in multi-step electrochemical oxidation processes. Table 4 reveals that the electrocatalytic oxidation of HMF is an area where Earth-abundant transition metals have not only narrowed the gap with noble metals but, in many cases, surpassed them in performance. A critical insight from Table 4 is the outstanding efficiency of Ni- and Co-based hydroxides/phosphides in alkaline media. For instance, the Ni_2P/NF (entry 5) and Co-LDH (entry 6) systems achieve near-quantitative conversion (>99%) and FDCA selectivity (>98%) at relatively low potentials (1.30–1.45 V), rivaling or exceeding the metrics of Au/C (entry 1). Furthermore, the data highlight that catalyst design, such as the hierarchical structure of Ni–Co–O

Table 4 Summary of the performance of representative catalysts for electrochemical HMF oxidation

No.	Catalyst	Electrolyte	Conc. (mM)	Potential (V *vs.* RHE)	Conv. (%)	Sel. (%)	FE (%)	Catalyst stability (h)	Deactivation mechanism	Ref.
1	Pd/C	0.1 M KOH	20	0.9	97	29 (FDCA)	—	—	—	86
2	Pd_1Au_2/C	0.1 M KOH	20	0.9	100	83 (FDCA)	—	—	—	86
3	PtRhPdIrRuAu[a]	0.1 M KOH	1	1.66	—	63.4 (HMFCA)	—	8	—	87
4	Ni(NS)/CP[a]	0.1 M KOH	5	1.36	99.8	99.2 (FDCA)	—	7.5	—	89
5	N–Co_3O_4/NF[a]	1.0 M KOH	10	1.423	99.5	96.4 (FDCA)	97.3	—	—	98
6	NiFe LDH[a]	1.0 M KOH	10	1.23	99	98 (FDCA)	99.4	6	Partial oxidation and/or structural changes of active sites	99
7	$CuNi(OH)_2$/C[a]	1.0 M KOH	5	1.45	100	93.3 (FDCA)	94.4	—	—	90
8	Vo-Co_3O_4 [a]	1.0 M KOH	10	1.47	~100	91.9 (FDCA)	88.1	—	—	91
9	NF@Co_3O_4/CeO_2 [a]	1.0 M KOH	10	1.40	98.0	94.5 (FDCA)	97.5	—	—	92
10	CoP–CoOOH[b]	1.0 M KOH	150	1.42	99.9	99.4 (FDCA)	98.2	167	—	93
11	$Ru_{0.3}$/NiFe[a]	1.0 M KOH	5	—	99.2	98.7 (FDCA)	98.3	20	—	94

[a] H-cell. [b] Flow-cell.

(entry 7), is pivotal for accelerating the multi-step oxidation of the formyl group while preserving the furan ring. This suggests that for HMF valorization, the field is successfully transitioning away from a dependence on precious metals toward the utilization of robust, non-noble interfaces that provide superior atomic economy and faradaic efficiency (>95%). Furthermore, most high-performance Ni/Co-based catalysts in Table 4 exhibit good operational stability, typically exceeding 6 h. Although the specific deactivation mechanisms have not been thoroughly investigated in many studies, it can be inferred that excessive oxidation or structural changes to the active sites under high potentials may be potential factors. For instance, NiFe LDH (entry 6) maintains high activity even after 6 h of reaction, suggesting that its active phase, NiOOH, possesses good electrochemical stability. Meanwhile, the stable operation of a CoP–CoOOH heterojunction in a flow cell for up to 167 h (entry 10) highlights the importance of rational structural design in resisting performance decay under prolonged operation.

Moderately increasing the temperature accelerates the reaction rate, whereas excessively high temperatures tend to promote side reactions. For instance, Xu *et al.* found that at 80 °C, HMFCA was the primary product, with low FDCA generation, because HMF and its intermediates are prone to side reactions like esterification or polymerization under elevated temperatures.[94] From the perspective of electrolyte concentration, high-concentration HMF electrolytes face pronounced issues of substrate diffusion and mass transport limitations. Xie *et al.* observed that as the HMF concentration increased from 5 mM to 10 mM, the FDCA selectivity rose from 47.5% to 84.9%.[95] Yet, concentrations exceeding 50 mM may lead to a slight decrease in FDCA yield, likely due to adsorption saturation on the catalyst surface. Furthermore, pH plays a crucial role: in strongly alkaline systems (pH $\geq$ 13), HMF oxidation follows the HMFCA pathway, whereas under mildly alkaline conditions (pH < 13), it proceeds *via* the DFF pathway. pH influences the C–H bond activation difficulty by affecting both the predominant form of the HMF molecule and the formation of active species.

The selectivity toward FDCA in the electrochemical oxidation of HMF is often limited by complex reaction networks and competing side reactions. Reactor engineering thus offers a transformative approach, where precise control over mass transport, electric-field distribution, and residence time can effectively direct the reaction pathway and enhance the product yield. In this context, Duan *et al.* developed a single-pass continuous flow reactor. By implementing a high electrode-area-to-electrolyte-volume ratio, minimizing the substrate residence time, and decoupling the substrate/alkali feed, the system successfully mitigated non-faradaic degradation. This design achieved exceptional HMF to FDCA conversion metrics at high concentrations (95.8% conversion, 96.9% selectivity, 556.9 mM), enabling continuous kilogram-scale synthesis (1.17 kg).[96] Building on this, the team recently showcased an engineered solid polymer electrolyte (SPE) reactor. Through the kinetic modulation of faradaic *versus* non-faradaic processes, efficient FDCA production was realized at industrial current densities (1.5 A cm^{-2}) without compromising selectivity (97.0%), faradaic efficiency (88.2%), or product concentration (~1.24 M). This SPE system demonstrated superior durability, operating stably for over 140 h at 0.5 A cm^{-2}. Furthermore, leveraging a modular scale-up approach, a 4.3 kW electrochemical platform was constructed, successfully achieving pilot-scale FDCA production at a rate of 33 kg day^{-1}.[97]

Electrocatalytic activation of C–H bonds in biomass-derived compounds is a pivotal strategy for biomass valorization. Transition metal-based catalysts (such as Pt, Au, Ni, and Co) can enhance the efficiency of C–H bond activation and site selectivity through structural optimization methods like electronic structure regulation and interface engineering. However, they still face challenges, including complex activation mechanisms, the vulnerability of catalysts to intermediate poisoning, and the difficulty in regulating selectivity in the presence of multiple types of C–H bonds. Additionally, most current research focuses on model compounds such as glucose, glycerol, and 5-hydroxymethylfurfural (HMF), while studies on the selective activation of diverse C–H bonds in natural biomass materials with more complex structures remain to be deepened. This stems from issues such as the difficulty in identifying activation sites due to complex structures, competing reactions caused by the coexistence of multiple components, and mass transfer limitations. Therefore, future research should leverage high-precision theoretical calculations and machine learning to decode the dynamic mechanisms of activation for different types of C–H bonds (primary, secondary, tertiary, and furan ring C–H bonds), and establish structure–activity relationship models between catalyst structures and site selectivity. Meanwhile, studies on the electrocatalytic conversion of complex biomass derivatives should be conducted to reveal the interaction rules between their complex structures and catalyst surfaces, thereby overcoming hurdles in selectivity and stability and facilitating the transition of electrocatalytic technology from model compounds to broader practical applications in biomass valorization.

3. Electrocatalytic activation of C=O/C–O bonds

As the fundamental structural units in biomass molecules like cellulose and lignin, selective C–O bond activation is essential for the green synthesis of high-value chemicals. Unlike traditional thermocatalytic methods that often require harsh conditions and noble metal catalysts,[100,101] electrocatalysis uses renewable electricity and precise potential control to achieve highly selective C–O bond conversion under mild conditions.[102,103] This approach offers superior atom economy and environmental benefits. Nevertheless, challenges remain due to the diverse types of C–O bonds in biomass, which vary considerably in bond dissociation energy and reactivity.[104,105] Competing side reactions such as over-hydrogenation and C–C

cleavage further complicate selectivity control. This section highlights recent advances in two key research areas. The first involves the selective hydrogenation of the C=O bond in the side chain of HMF during its reduction. It details the electrocatalytic mechanism for converting HMF into the polymer precursor 2,5-bis(hydroxymethyl)furan (BHMF), and discusses strategies to activate the side chain C=O bond while suppressing furan ring saturation or C–O cleavage. The second focuses on activating C–O bonds in lignin, specifically through the selective cleavage of characteristic β-O-4 and α-O-4 linkages, enabling efficient depolymerization under mild conditions. A systematic analysis is provided from three perspectives—reaction mechanisms, catalyst design, and the influence of reaction conditions, with an emphasis on the roles of applied potential, electrolyte pH and composition, and mass transport. This section aims to provide theoretical guidance for the rational design of electrocatalysts and the optimization of processes for biomass C–O bond activation.

3.1 Electrocatalytic activation of C=O bonds: HMF reduction

The HMF molecule features multiple C–O bond structures, including an aldehyde group (C=O), a furan ring ether linkage (C–O–C), and a hydroxymethyl group (C–OH). The selective activation and transformation of these bonds represent the core challenge in synthesizing high-value products.[106] Among them, BHMF—a symmetric diol—serves as a key monomer for producing bio-based polyesters, pharmaceutical carriers, and green solvents,[107] with its value significantly surpassing that of HMF. Efficient BHMF production fundamentally depends on the precise selective hydrogenation of the aldehyde C=O bond in HMF, while strictly suppressing side reactions such as hydrolytic ring-opening of the furan ring C–O–C bond or dehydration of the hydroxymethyl C–OH bond to maintain product purity and yield. Although conventional thermocatalytic hydrogenation can reduce HMF, it often fails to precisely regulate the competing activation among these multiple C–O bonds.[108,109] Under high-temperature and high-pressure hydrogen conditions, noble metal catalysts (*e.g.*, Pt, Ru) tend to over-reduce the aldehyde group to form 2,5-dimethylfuran (DMF) or cleave the furan ring C–O–C bond, yielding linear byproducts and markedly reducing the BHMF selectivity. The inability to controllably activate specific C–O bonds has become the major bottleneck in the cost-effective production of BHMF. Electrocatalytic reduction, utilizing its potential-driven mechanism for precise bond activation, offers a new approach to address this selectivity issue. By designing active sites on cathode catalysts and tuning the electrode potential, this method can selectively lower the activation energy barrier for the aldehyde C=O bond, promoting its hydrogenation to the target primary alcohol group. The core challenge in the electrocatalytic reduction of HMF to BHMF lies in the efficient activation of the carbonyl (C=O) bond and the precise regulation of the hydrogenation pathway. A study of the reaction mechanism shows that there are significant differences in the C–O activation pathway on different catalyst surfaces (Fig. 7a). On Ag catalysts such as Ag and RhCu, the hydrogen atom transfer path mediated by H_{ads} is dominant. Water is first dissociated in the Walmer step to form adsorbed hydrogen, which then preferentially attacks the carbonyl oxygen atom of HMF to form a key intermediate. The intermediate is then subjected to two consecutive hydrogenation reactions to generate BHMF.[112–114] For instance, an Ag electrode at a potential of −1.3 V, benefiting from high H_{ads} coverage, can effectively suppress intermolecular C–C coupling side reactions, such as the formation of 2,5-bis(hydroxymethyl)hydrofuran (BHH).[112] In contrast, Cu-based catalysts (*e.g.*, Ru_1Cu single-atom alloys) favor a PCET mechanism, involving the direct reduction of the carbonyl group through concerted proton–electron transfer, although this path is prone to inducing dimerization side reactions under high-potential conditions.[111,115] Notably, buffering electrolyte anions (*e.g.*, phosphate) can act as proton shuttles, significantly reducing the C–O activation energy barrier *via* the Langmuir–Hinshelwood (L–H) mechanism.[116,117] As exemplified by Co_3O_4, the proton-donating capability of phosphate (adsorption energy ΔE_{ad} = −2.26 eV) is markedly superior to that of water, thereby substantially enhancing the hydrogenation efficiency. In summary, the selectivity of the C–O activation pathway is fundamentally the result of the synergistic effect between the intrinsic properties of the catalyst and the electrolyte environment.

The design of highly efficient catalysts necessitates the synergistic regulation of C–O bond activation selectivity, H_{ads} supply capability, and the suppression of side reactions. In noble metal optimization, Ag emerges as an ideal support due to its low hydrogen evolution reaction (HER) activity: dendritic high-surface-area Ag achieves 99% FE and product selectivity by exposing abundant active sites.[112] Meanwhile, the Ag/SnO_2 heterojunction leverages the selective adsorption of carbonyl groups by SnO_2 oxygen vacancies and the enhanced water dissociation promoted by Ag nanoparticles, maintaining FE > 95% over a wide potential window of −0.62 to −1.12 V.[116] The isolated Ru sites facilitate water dissociation, thereby generating an H_{ads}-enriched interfacial environment. This key feature alters the reaction pathway from the direct electroreduction observed on pristine Cu, which is susceptible to dimerization, toward a highly efficient electrocatalytic hydrogenation route (Fig. 7b). The ESR spectrum using DMPO as a spin-trapping agent (Fig. 7c) showed a significantly enhanced desorption peak of H_{ads} on the RhCu surface, indicating a greater generation of H_{ads}, which confirmed the role of Rh. Additionally, *in situ* ATR-SEIRAS spectra (Fig. 7d and e) revealed a characteristic peak at 2050 cm^{-1}, attributed to Rh–H_{ads}, the intensity of which increased with more negative applied potentials and was significantly stronger on RhCu than on Cu. At 3620 cm^{-1}, RhCu exhibited a more intense peak corresponding to weakly hydrogen-bonded water molecules, indicating that Rh promoted the formation of ordered, weakly hydrogen-bonded water. These weakly hydrogen-bonded water molecules dissociate more readily to generate H_{ads}, thereby establishing a H_{ads}-enriched interfacial environment. Notably, at a high HMF concentration of 100 mM, Ru_1Cu SAA maintained a high FE of 87.5% for BHMF production (Fig. 7g), a stark contrast to the

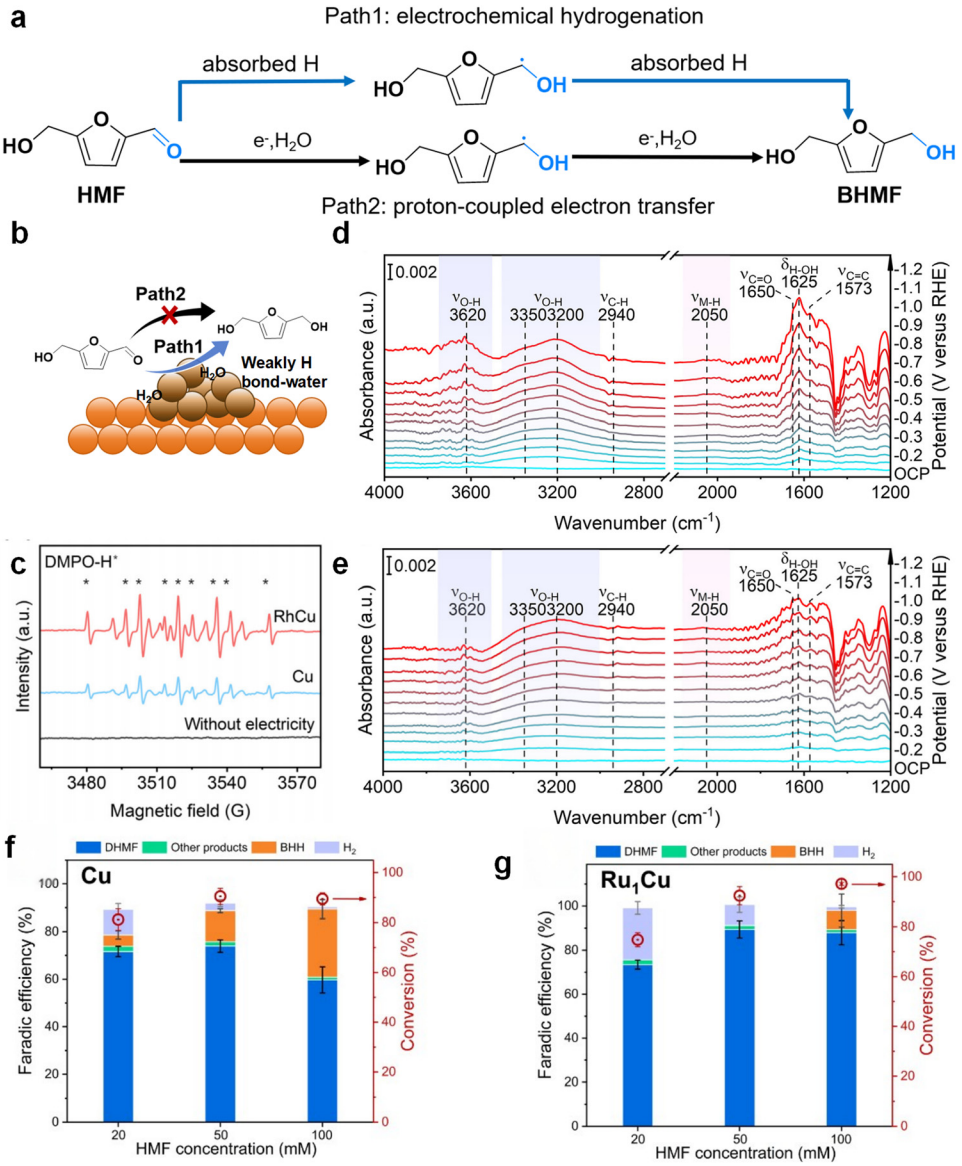

Fig. 7 (a) Schematic representation of the electrochemical reduction mechanism of 5-HMF. (b) Schematic diagram of the electrochemical hydrogenation process of HMF over the RhCu catalyst. (c) ESR spectra of the trapping of hydrogen radicals over RhCu and Cu; reproduced from ref. 110 with permission from Elsevier, copyright 2023. (d) RhCu and (e) Cu *in situ* ATR-SEIRAS spectra under various potentials for the HMF-containing system; reproduced from ref. 110 with permission from Elsevier, copyright 2023. (f) Cu and (g) Ru_1Cu at various concentrations of HMF. Reaction conditions: −0.5 V (*vs.* RHE), passed charges for 20 mM, 50 mM and 100 mM concentration of HMF were 154 C, 390 C, and 790 C, respectively; reproduced from ref. 111 with permission from Wiley-VCH GmbH, copyright 2022.

significantly decreased FE of 59.7% observed for its Cu counterpart (Fig. 7f).[111] DFT calculations reveal that the single-atom Ru sites act as highly efficient water activation centers, significantly lowering the energy barrier for water dissociation and thereby promoting the substantial generation of H. These H species with high surface coverage subsequently react with adsorbed HMF molecules *via* a Langmuir–Hinshelwood mechanism, efficiently hydrogenating them to the target product DHMF. Concurrently, this pathway suppresses the undesired side reaction of HMF dimerization, which would otherwise occur *via* the direct electron transfer route leading to radical intermediates. The Cu/Cu_2O heterointerface enhances H_{ads} adsorption *via* an upward shift of the d-band center while optimizing the adsorption of HMF and the desorption kinetics of DHMF.[117] Regarding supports and structural innovations, N-doped carbon-supported Cu (Cu/NC) strengthens carbonyl adsorption through electron-deficient Cu sites and accelerates charge transfer *via* the electromagnetic shielding effect.[118] The 3D porous BiSn electrode, fabricated using a hydrogen bubble template, increases the electrochemically active surface area (double-layer capacitance C_{dl} = 3.6 mF cm^{-2}), achieving 100% FE at a high current density of 144 mA

Table 5 Summary of the performance of representative catalysts for electrochemical HMF reduction

No.	Catalyst	Electrolyte	Conc. (mM)	Potential (V *vs.* RHE)	Conv. (%)	Sel. (%)	FE (%)	Sel. (%)	FE (%)	Ref.
1	Co_3O_4 [a]	0.1 M PBS	10	−0.59	96	80	26.3	Catalyst stability (h)	Deactivation mechanism	116
2	BiSn[a]	0.5 M PBS	2000	−1.83	~30	~100	~100	—	—	119
3	Ag/Cu foam[a]	0.5 M BBS	20	−0.56	~37.1	99	99	4	—	112
4	Ag/C[a]	0.5 M BBS, pH 9.2	20	−0.56	~50	~85	96.2	—	—	113
5	Ag/SnO_2 [a]	0.5M $KHCO_3$	50	−0.62	—	~99	98.8	—	—	116
6	Oxide-derived-Ag[a]	0.5 M BBS, pH 9.2	20	−0.51	28.9	95.3	~80	—	—	114
7	Ru_1Cu SAA[a]	0.5 M PBS, pH ~7	20	−0.30	65.9	~90	87.0	3	—	111
8	$Cu(OH)_2$-ER/Cu foam[a]	0.1 M KOH	5	−0.15	98.5	—	92.3	20	—	115
9	Cu/Cu_2O[b]	PBS, pH 9.2	10	−0.35	90.7	100	80.5	10	—	117
10	RhCu NWs[a]	0.5 M Na_2SO_4	50	~−0.10	~100	—	92.6	25	Surface reconstruction leading to amorphous layer formation	110
11	Cu/CeO_2 [a]	BBS, pH 9.2	100	−0.51	—	~75	74	16	—	120
12	Pd_3Pt_1 [a]	0.5 M K_2SO_4	50	−0.30	54.72	66.5	94.5	18	—	121

PBS: phosphate buffer; BBS: borate buffer. [a] H-cell. [b] Flow-cell.

cm^{-2}.[119] Clearly, modulating the electronic structures, optimizing interfacial microenvironments, and designing mass transfer structures are the core directions for enhancing the C–O activation efficiency. Table 5 underscores the performance trade-off between HMF reduction and the competing hydrogen evolution reaction (HER). The data reveal that metallic alloying and interface engineering are pivotal for suppressing the HER to enhance FE. Specifically, while oxide-based Co_3O_4 (entry 1) exhibits a low FE of 26.3% due to the dominant HER, the Ag/Cu foam (entry 3) and Ag/C (entry 4) architectures achieve superior FEs (>96%) at −0.56 V. Furthermore, near-quantitative selectivity is attained across diverse regimes: the BiSn alloy (entry 2) requires a high negative potential of −1.83 V, whereas the Cu/Cu_2O system (entry 8) reaches 100% selectivity at 0.35 V. The prevalence of neutral buffers (*e.g.*, BBS/PBS) among high-performing entries (entries 3, 6 and 9) highlights the necessity of a controlled local environment. Consequently, the field is advancing toward sophisticated interfaces, such as single-atom alloys (entry 7) and oxide-derived metals (entry 6), to prioritize organic activation and maximize energy efficiency. Catalyst stability is crucial for the continuous reduction of HMF. As shown in Table 5, stability can be extended to 10–25 h or longer by constructing alloys (*e.g.*, RhCu NWs), single-atom alloys (Ru_1Cu SAA), or stable heterostructures (*e.g.*, Cu/Cu_2O). Possible deactivation mechanisms include leaching and agglomeration of active metals, as well as surface reconstruction. For example, deactivation of the Cu/Cu_2O heterostructure after 25 h of operation in a flow cell was attributed to surface reconstruction, forming an amorphous layer. Therefore, future research should focus on developing robust cathode materials that combine a high faradaic efficiency, high selectivity, and an ultra-long operational lifetime (>1000 h) under industrially relevant current densities and concentrations.

Reaction conditions significantly regulate C–O activation efficiency by influencing H_{ads} coverage, proton transfer kinetics, and mass transfer processes. Regarding potential window control, the Ag electrode achieves optimal H_{ads} coverage (FE–100%) at −1.3 V; excessively negative potentials (<−1.6 V) intensify the HER, while overly positive potentials (>−1.1 V) induce polymerization side reactions due to insufficient H_{ads}.[112] Conversely, the BiSn catalyst balances a high current density with 100% FE at −0.71 V.[119] In terms of pH and electrolyte environment, neutral to weakly alkaline conditions (pH 7–9.2) are most favorable for the reaction;[117,119,120] acidic conditions (pH = 1) promote the formation of 2,5-dimethylfuran (*e.g.*, Pd single atom/TiO_2 catalyst selectivity reached 37.3%), while strongly alkaline conditions (pH > 13) induce HMF decomposition.[122] Phosphate buffer (pH 9) exhibits a superior kinetic performance in the supply of protons *via* the Langmuir–Hinshelwood mechanism compared to KOH systems,[117] and borate buffer (pH 9.2) stabilizes the HMF structure and suppresses an ohmic drop.[120] For concentration and mass transfer regulation, near 100% product selectivity is achievable at a low HMF concentration (0.02 M), whereas a high concentration (0.10 M) readily triggers dimerization side reactions.[111,112] The flow cell design enhances mass transfer, enabling a 19% increase in conversion for ordered mesoporous Ag while reducing the operating voltage to 2.0 V. Regarding coupled systems, pairing cathodic electrocatalytic hydrogenation (ECH) with anodic oxidation reactions (*e.g.*, TEMPO-mediated conversion of HMF to FDCA) can lower the overall cell voltage requirement. For instance, a Pd_3Pt_1 bimetallic layer electrolyzer achieved a current density of 10 mA cm^{-2} at a potential of 0.72 V, demonstrating 43% energy savings compared to conventional systems.[121] In summary, synergistic potential–pH regulation and reactor mass transfer optimization are critical factors for achieving industrial-scale C–O activation.

Paralleling the electro-oxidation of HMF, reactor design is of paramount importance in HMF electrochemical reduction, fundamentally governing the product distribution and conversion efficiency. Schmidpeter *et al.* addressed this by developing a three-dimensional fixed-bed flow reactor employing spherical

polymer-supported carbon–copper catalysts for efficient HMF to DHMF conversion. Through optimization of the carbon sphere dimensions, the system effectively mitigated a pressure drop and ohmic resistance, achieving high conversion (89.6%) and selectivity (84.0%). Crucially, the reactor exhibited robust scalability; a twofold increase in the electrode width yielded a linear doubling of the production rate while maintaining stable selectivity (85.1%). These findings underscore the distinct advantages of 3D fixed-bed architectures for the large-scale electrosynthesis of biomass derivatives.[123] Focusing on device integration and upscaling, Hauke *et al.* designed a high-efficiency alkaline exchange membrane (AEM) electrolyzer utilizing oxide-derived copper bimetallic catalysts (Cu/MO_x). Initially, by tailoring the surface properties of the MO_x phase, they achieved the tunable reduction of HMF to either BHMF or 5-methylfurfuryl alcohol in alkaline media (*via* $2e^-$ and $(2 + 2)e^-$ pathways, respectively). Moreover, capitalizing on the AEM configuration, the study realized the efficient synergistic coupling of cathodic HMF valorization with anodic processes, demonstrating the substantial promise of this integrated approach for scalable electrochemical manufacturing.[124]

3.2 Selective cleavage of C–O bonds in lignin and its derived platform molecules

Lignin, as the most abundant aromatic biomass resource in nature, holds significant importance for replacing fossil resources in producing high-value chemicals.[125,126] Lignin molecules contain a large number of C–O bond linkages, among which β-O-4 and α-O-4 bonds are the two most representative ether bonds.[127,128] β-O-4 bonds constitute over 50% of lignin linkages, while α-O-4 bonds account for nearly 50% in gymnosperm lignin. The selective cleavage and targeted conversion of these bonds represent the core challenge in depolymerizing lignin into high-value monomers (*e.g.*, phenolics, aromatic alcohols).[129] Conventional thermocatalytic methods struggle to precisely control the competing activation of these two bonds and often induce side reactions such as over-hydrogenation of aromatic rings, random cleavage of C–C bonds, or product repolymerization, leading to a significant decrease in target monomer selectivity.[130,131] Electrocatalytic cleavage technology, leveraging its potential-driven precise bond energy modulation mechanism, offers a solution. By designing active sites on electrode catalysts and controlling the working potential, it can selectively reduce the activation barrier of specific C–O bonds, opening a green pathway for the efficient and highly selective conversion of lignin.[132,133] The mechanisms for electrocatalytic cleavage of lignin C–O bonds can be categorized into two main types: oxidative cleavage and reductive cleavage. The core difference lies in the generation and transformation pathways of the active intermediates, driven by distinct catalysts and reaction systems, which exhibit marked specificity.

The oxidative cleavage mechanism primarily relies on the action of reactive oxygen species such as $^{\bullet}OH$, $^{\bullet}O_2^-$, and $^{\bullet}OOH$. In the reaction catalyzed by Ni–Co/C on the β-O-4 model compound (2-phenoxy-1-phenylethanol, PPE), Co promotes the generation of $^{\bullet}OOH$, while Ni enhances the stability of $^{\bullet}O_2^-$. $^{\bullet}OOH$ initiates β-carbon elimination by attacking the C_α–C_β bond, whereas $^{\bullet}O_2^-$ directly oxidizes the C_β–O bond, cleaving it and ultimately yielding products such as benzaldehyde and acetophenone (Fig. 8a).[134] During the cleavage of α-O-4 bonds catalyzed by rhombohedral $ZnIn_2S_4$ (R-ZIS), In sites strongly adsorb and immobilize the benzylic C–O bond of benzyl phenyl ether (BPE). S^{2-} reacts with H_2O to generate $^{\bullet}OH$, which attacks the benzylic carbon, leading to bond cleavage. Subsequently, benzyl alcohol is further oxidized to benzaldehyde and benzoic acid. ^{18}O isotope labeling confirmed that the oxygen atoms originated from water.[135] The mechanism for β-O-4 bond cleavage catalyzed by spinel $NiFe_2O_4$ is similar. Fe^{3+} promotes the generation of $^{\bullet}OH$, which lowers the bond energy barrier through electrophilic attack on the oxygen atom within the β-O-4 linkage, achieving oxidative cleavage of the C_β–O bond.[136] Furthermore, in the NaCl/MeOH system, Cl^- generates chlorine radicals ($Cl^{\bullet}$) under electrocatalytic conditions. $Cl^{\bullet}$ abstracts a C_β–H atom, forming a C_β radical. This radical then combines with $^{\bullet}O_2^-$ to form a peroxo intermediate, ultimately leading to α-O-4 bond cleavage and producing benzaldehyde dimethyl acetal.[137]

In contrast, the reductive cleavage mechanism relies on the synergistic transfer of protons and electrons, achieving C–O bond cleavage *via* hydrogenation or hydrogenolysis. During Ni-catalyzed cleavage of α-O-4 bonds, Ni^{2+} is reduced to Ni^0 at the cathode, simultaneously generating adsorbed hydrogen. After BPE adsorbs onto the Ni surface, Ni^0 activates the benzylic C–O bond, and H_{ads} participates in protonation, cleaving the bond to yield toluene and phenol. Crucially, the valence cycling of Ni ions ($Ni^{2+} \rightarrow Ni^0 \rightarrow Ni^{2+}$) is key to sustaining the reaction.[138] For CuO-catalyzed cleavage of the Caryl–O bond in β-O-4 linkages, residual Cu(I) enhances adsorption onto the aromatic ether oxygen, lowering the barrier for proton attack. This facilitates cleavage *via* a "protonation–electron transfer" step, generating a phenoxy radical and a phenylethanediol intermediate, which are ultimately hydrogenated to hydroquinone and benzyl alcohol, thereby avoiding over-reduction of the aromatic ring (Fig. 8b).[133] In PdNiBi-catalyzed reductive cleavage of β-O-4 bonds, Pd sites activate H_2O to generate H_{ads}, while Bi modulates the electron density of Ni to optimize the adsorption energy. This enables cleavage of the β-O-4 bond through hydrogenation, yielding phenol and acetophenone. The synergistic effect between Pd and Ni suppresses the competing HER.[139] Catalysts serve as the core of electrocatalytic C–O bond cleavage. Their electronic structure, surface properties, and synergistic effects of components directly determine the activity and selectivity. Based on research findings, catalysts can be classified into three categories: single-metal-based, bimetallic/alloy, and metal oxides/spinel, each excelling in specific C–O bond cleavage scenarios. Monometallic catalysts excel at α-O-4 bond cleavage due to their simple structure and well-defined active sites. Ni-based catalysts (*e.g.*, Ni foam or Ni salts) achieve 100% conversion of the α–O–4 model compound BPE in methanol systems, with maximum toluene and phenol yields of 97% and 84%, respectively. This high activity orig-

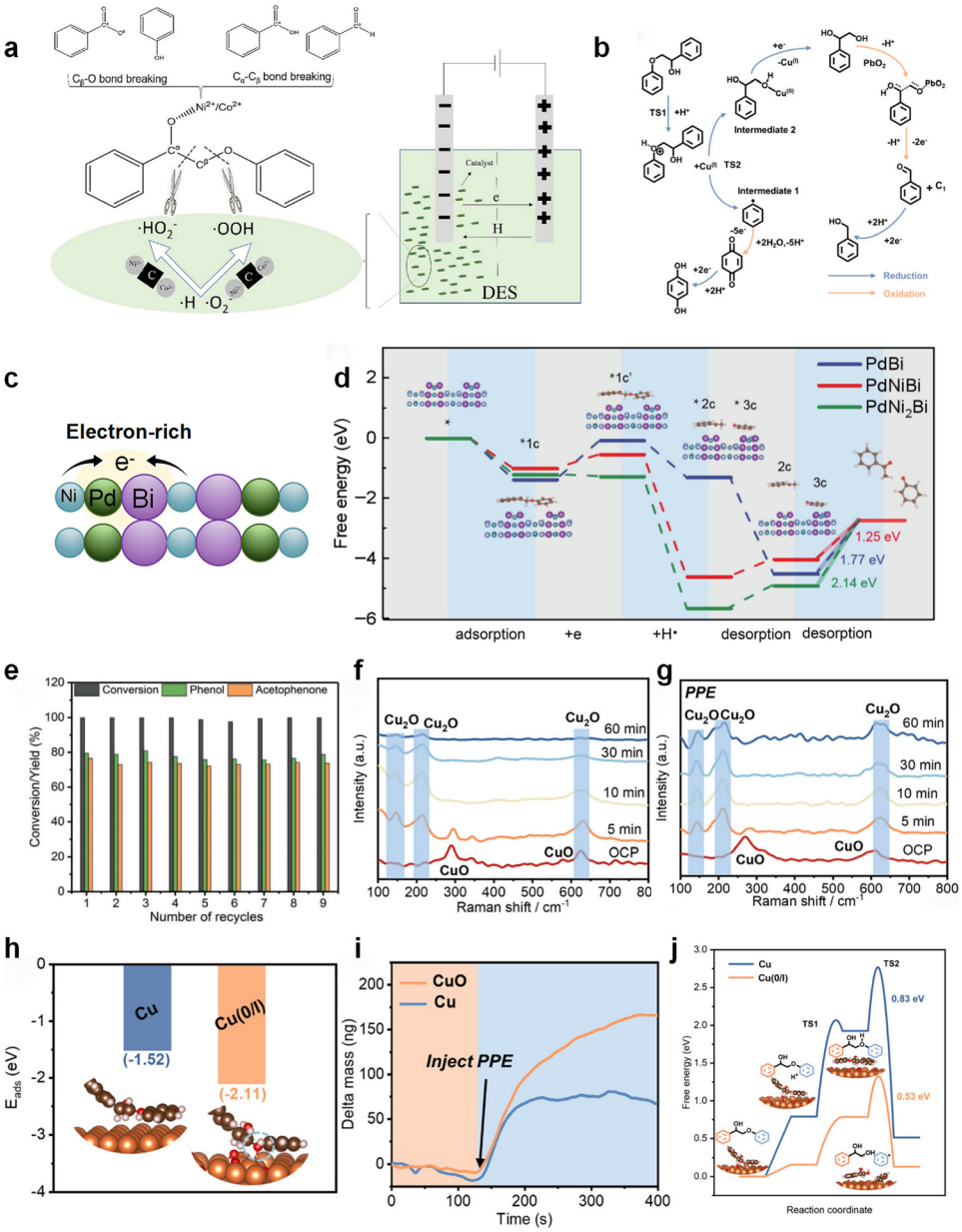

Fig. 8 (a) Diagram of the electrochemical oxidative cleavage of C–O; reproduced from ref. 134 with permission from Elsevier, copyright 2023. (b) Possible PPE reductive cleavage of C–O mechanisms over a CuO/CF cathode under acidic conditions; reproduced from ref. 133 with permission from the American Chemical Society, copyright 2024. (c) Schematic illustration of the electronic structures of PdNiBi. (d) The free energy curve for C–O cleavage catalyzed by PdBi, PdNiBi, and $PdNi_2Bi$; reproduced from ref. 139 with permission from Springer Nature, copyright 2024. (e) Conversion and product yields of 9 successive cycles for the PdNiBi catalyst; reproduced from ref. 139 with permission from Springer Nature, copyright 2024. *In situ* Raman spectra over different electrolysis durations (f) without and (g) with PPE; reproduced from ref. 133 with permission from the American Chemical Society, copyright 2024. (h) Adsorption energies of PPE on Cu and Cu(0/1) crystal models; reproduced from ref. 133 with permission from the American Chemical Society, copyright 2024. (i) QCM mass response over CuO and Cu before and after injecting PPE; reproduced from ref. 133 with permission from the American Chemical Society, copyright 2024. (j) Free energy of the PPE cleavage mechanisms over the Cu and Cu(0/1) surfaces; reproduced from ref. 133 with permission from the American Chemical Society, copyright 2024.

inates from strong adsorption of the benzylic C–O bond on Ni sites and its valence state cycling capability, requiring neither precious metals nor harsh conditions.[138] Pt electrodes also demonstrate specific activity in NaCl/methanol systems. Utilizing Cl^--generated radicals, they facilitate the conversion of BPE to benzaldehyde dimethyl acetal with 95.2% conversion and 94.5% product selectivity. Employing carbon cloth as the counter electrode further enhances the electron transfer efficiency.[137] Bimetallic catalysts optimize active sites through intercomponent electron transfer, significantly enhancing the β-O-4 bond cleavage efficiency. In Ni–Co/C, the synergy between Ni and Co strengthens PPE adsorption, while the

porous architecture provides abundant active sites. This system achieves >90% depolymerization yield in deep eutectic solvent media, delivering benzaldehyde and acetophenone at 124.08 mg g^{-1} and 23.29 mg g^{-1}, and this substantially exceeds the performance of its monometallic Ni/C or Co/C counterparts.[134] In the PdNiBi trimetallic catalyst, the ternary alloy structure facilitates electron transfer from Ni to Pd/Bi, generating electron-rich Pd and Bi active sites that optimize the adsorption behavior toward reaction intermediates (Fig. 8c).[139] This electronic structure enhances electron injection into the C–O bond, effectively weakening and activating the bond, thereby significantly reducing its cleavage barrier. DFT free energy calculations reveal that the energy barrier for C–O bond cleavage on the PdNiBi surface is considerably lower than that on PdBi and $PdNi_3Bi$ (Fig. 8d). As a result, the catalyst achieves complete conversion of β-O-4 model compounds, with yields of phenolic compounds and acetophenone reaching 80–99% and 75–96%, respectively. Furthermore, the moderate electronic structure ensures effective adsorption and activation of reactants while promoting smooth desorption of the cleavage products (phenolics and acetophenone), thereby preventing active site blockage. This contributes to the stability of the catalyst over nine consecutive reaction cycles (Fig. 8e). Metal oxide catalysts balance activity and stability in oxidative cleavage pathways by modulating oxygen species generation and electronic structures. Zou *et al.* found that during the catalytic process over CuO nanorods, *in situ* formed and stabilized Cu(0/I) mixed-valence active sites played a key role. Cu(I) sites enhance the adsorption of the Caryl–O(C) bond and lower the reaction energy barrier, achieving high yields of hydroquinone (95.3%) and benzyl alcohol (88.6%) at −0.4 V (*vs.* RHE). In the depolymerization of poplar lignin, a guaiacyl glycerol yield of 10.9 wt% with over 63% selectivity was obtained.[133] *In situ* Raman spectroscopy (Fig. 8f and g) confirmed that the reactant PPE effectively suppressed the further reduction of Cu(I), thereby maintaining its stability during the reaction. DFT calculations (Fig. 8h) and QCM mass response analysis (Fig. 8i) revealed that the adsorption energy of the Caryl–O(C) bond in PPE on Cu(0/1) sites (−2.11 eV) was significantly stronger than that on pure Cu (−1.52 eV). Moreover, the bond is directionally activated *via* a specific adsorption configuration involving the oxygen atom and the catalyst surface. Additional energy barrier analysis (Fig. 8j) indicated that the Cu(0/1) sites reduced the energy barrier of the rate-determining step for Caryl–O(C) bond cleavage from 0.83 eV on pure Cu to 0.53 eV, markedly enhancing the reaction kinetics. For $NiFe_2O_4$ spinel, Ni–Fe synergy homogenizes the electron distribution, reducing the C–O bond cleavage activation energy. In 1.0 M KOH, it demonstrates 82% PPE conversion with 72% phenol selectivity, requiring an overpotential of only 190 mV at 10 mA cm^{-2}, suitable for alkaline lignin depolymerization.[136] Table 6 highlights the critical influence of catalyst composition and electrolyte media on the C–O bond cleavage efficiency. A key trend is the superior performance of multi-metallic systems and integrated carbon architectures across diverse solvent environments. For instance, while $NiFe_2O_4$ (entry 4) achieves 82% conversion in alkaline methanol, more sophisticated PtNiBi (entry 2) demonstrates near-quantitative conversion 98.6% in ionic liquids. Additionally, the data reveal high versatility in reaction conditions, ranging from high-current-density organic systems for Ni–Co/C (entry 1) to acidic aqueous media for CuO (entry 7), yielding 98.8% hydroquinone. This comparison underscores that optimizing the electrode–electrolyte interface is pivotal for tailoring adsorption–cleavage pathways of specific aryl–ether linkages. Catalyst stability is a key bottleneck in the practical application of lignin electrocatalytic conversion. Data from Table 6 show that polymetallic systems (*e.g.*, PtNiBi) and carbon composite structures exhibit excellent stability (>72 h) in special media such as ionic liquids. In contrast, in aqueous or alcoholic phases, metal oxide catalysts (*e.g.*, $NiFe_2O_4$) may deactivate due to agglomeration during prolonged operation. Therefore, designing catalysts that can withstand complex reac-

Table 6 Summary of the electrochemical performance of representative catalysts for C–O bond cleavage of lignin-derived monomers

No.	Catalyst	Electrolyte	Conc. (mM)	Conditions	Conv. (%)	Yield (%)	FE (%)	Catalyst stability (h)	Deactivation mechanism	Ref.
1	Ni–Co/C[a]	DES/CH_3CN	0.1 PPE	80 mA cm^{-2}	91.86	Benzaldehyde: 36.3, benzoic acid: 44.64, acetophenone: 23.29	—	6	—	134
2	PtNiBi[a]	[Emin][BF_4]/MeCN	5 PPE	−2.0 V *vs.* Ag/AgCl	98.6	Phenol: 79.5, acetophenone: 86.9	—	72	—	139
3	$ZnIn_2S_4$ [a]	Borate buffer/ acetonitrile	10 BPE	2.0 V *vs.* Ag/AgCl	99	—	53.4	24	—	135
4	$NiFe_2O_4$ [a]	KOH/CH_3OH	1 PPE	25 mA cm^{-2}	82	Phenol: 72	—	30	Catalyst agglomeration	136
5	Pt[b]	NaCl/CH_3OH	20 BPE	25 mA cm^{-2}	95.2	Benzaldehyde dimethyl acetal: 94.5	—	—	—	137
6	Carbon paper[a]	$TBAPF_6$/$NiCl_2$	10 BPE	20 mA cm^{-2}	93	Toluene: 90, phenol: 84	14.5	25	—	138
7	CuO[a]	Acidic aqueous	5 BPE	−0.4 V *vs.* RHE	96.5	Hydroquinone: 98.8, benzyl alcohol: 91.8	—	20	—	133

[a] H-cell. [b] Single-cell.

tion media while resisting leaching or aggregation of active components is essential for achieving efficient and stable lignin electrolysis.

System optimization involves adjusting the reaction medium, temperature, current density, and applied potential. Medium selection must balance lignin solubility, ionic conductivity, and intermediate stability. Methanol exhibits an excellent performance in α-O-4 cleavage by hydrogen bonding with BPE. Deep eutectic solvents (DES, such as choline chloride–ethylene glycol) promote the cleavage of β-O-4 through a free radical-stabilized hydrogen bond network. Ionic liquids (*e.g.*, [Emim][BF_4]) inhibit the hydrogen evolution reaction in the reduction system, and a co-solvent with methanol can enhance mass transfer. The electrolyte usually participates in the reaction outside of ion conduction. For example, TBAPF6 is superior to $NaClO_4$ in the Ni system by avoiding phenol oxidation. The conversion rate of BPE reached 95.2% by chlorine-free radicals generated in NaCl solution. The alkaline electrolyte (*e.g.*, 1.0 M KOH) deprotonated the phenolic hydroxyl group, which reduced the overpotential of nickel ferrite by 50 mV and increased the conversion rate by 15%. Temperature modulates reaction kinetics. Although most electrocatalytic systems operate at room temperature, R-ZIS requires 65 °C to accelerate the formation of $^{\bullet}OH$ (increasing the BPE conversion from 70% to 99%). Electrical parameters dictate performance boundaries. For the electrochemical reduction reaction, the CuO peak has a more negative potential at −0.4 V *vs.* RHE, and the hydrogen evolution reaction will reduce the yield of benzyl alcohol. During the oxidation process, Ni–Co/C reached the maximum value of PPE depolymerization at 80 mA cm^{-2}, while the product was overoxidized to CO_2 when the current was over 100 mA cm^{-2}.

Wijaya *et al.* leveraged a stirred slurry electro-reactor (SSER) to realize the electrocatalytic hydrogenation of guaiacol under mild conditions. Kinetic studies elucidated that the reaction was governed by mass transport and particle–electrode contact, with demethoxylation identified as the rate-determining step (RDS). Notably, the system maintained superior stability at industrially relevant current densities (>100 mA cm^{-2}), thereby validating its scalability for biomass valorization.[140] Conversely, to circumvent the economic constraints of membrane-dependent architectures, Huang *et al.* engineered a membraneless paired electrolysis platform. This system facilitated the synergistic coupling of cathodic lignin hydrogenolysis with anodic C–H/N–H cross-coupling. Operating with a carbon felt anode and Ni foam cathode, the protocol achieved the quantitative cleavage of C–O linkages in β-O-4 models, concurrently yielding acetophenone and triarylamine derivatives with high selectivity. Importantly, this strategy demonstrated broad compatibility with various functional groups. It was particularly effective for oxidation-sensitive phenolic hydroxyl groups. The approach also featured a simplified and cost-efficient reactor design.[141]

In the electrocatalytic activation of C–O bonds in biomass-derived compounds, transition metal-based catalysts (such as nickel, cobalt, copper, silver, *etc.*) can enhance the reaction activity and selectivity through structural optimization (alloying, single-atom modification, heterostructure construction, *etc.*). However, this field still faces multiple challenges. Firstly, the types of C–O bonds in biomass are complex (ether bonds, hydroxyl groups, epoxy groups, *etc.*), and the bond dissociation energies and reactivity vary significantly, making it difficult to precisely regulate the activation pathways. Secondly, the stability of the catalysts is insufficient; some systems are prone to performance degradation during cyclic use due to the loss of active sites or carbon deposition. In addition, it is challenging to control product selectivity, which is easily interfered by competing side reactions such as excessive hydrogenation and C–C bond cleavage. Therefore, future research should utilize high-precision theoretical calculations (DFT) and *in situ* characterization techniques to analyze the dynamic reaction pathways of C–O bond activation and the evolution laws of intermediates, and establish a structure–activity relationship model between the electronic structure of the catalyst and reaction performance. It is necessary to systematically study the interaction mechanism between complex components and the catalyst surface, and develop anti-poisoning and high-stability catalytic systems to overcome the bottlenecks of selectivity and stability, thereby promoting the transition of electrocatalytic C–O bond activation technology from model systems to practical industrial applications.

4 Electrocatalytic activation of C–C bonds

The targeted valorization of biomass into high-value chemicals represents a critical pathway toward achieving carbon neutrality and advancing sustainable development.[142,143] The activation of C–C bonds is the key to achieving the conversion of biomass. Electrocatalytic cleavage of C–C bonds enables precise molecular-level product control through selective bond scission, yielding target products.[144,145] However, the efficiency of electrochemical C–C bond cleavage is largely determined by electrocatalyst properties, including electronic structure, crystallinity, and coordination environment, which control substrate/intermediate adsorption–desorption.[145,146] At present, the strategies for modulating and designing electrocatalysts are widely applied to the cleavage of C–C bonds in biomass-derived compounds. In this section, we introduce two types of biomass-derived compounds, namely, polyols and lignin-based compounds.

4.1 Polyol cleavage: valorization of small molecules

Glycerol, a low-value byproduct of biodiesel production, is a common biomass model compound. Controlled C–C bond cleavage can convert glycerol into valuable products such as formic acid (C1), glycolic acid (C2), and oxalic acid (C2). Precise catalyst and reaction system design is essential for controlling product formation.

Formic acid (FA), produced through complete C–C bond cleavage of glycerol, serves as a vital industrial feedstock and an efficient hydrogen storage carrier. Research on the electro-

catalytic oxidation of glycerol into FA primarily focuses on non-precious metal systems, due to their low cost and great activity. Li *et al.* developed nickel–molybdenum–nitride nanoplates on carbon cloth (Ni–Mo–N/CFC) as electrocatalysts, enabling FA production from glycerol in alkaline solutions at a cell voltage of 1.36 V (10 mA cm^{-2}) with 95% FE.[147] Doping strategies are commonly used to enhance electrocatalyst performance. Han *et al.* reported doping Co_3O_4 with transition metals (M = Mn, Fe, Co, Ni) to synthesize MCo_2O_4 spinel-structured catalysts for glycerol electrooxidation.[148] The $CuCo_2O_4$ catalyst exhibited a superior performance, achieving up to 80.6% FA selectivity. However, the cleavage mechanism of the C–C bond was unexplained. Duan *et al.* demonstrated that Bi-doped Co_3O_4 achieved efficient glycerol conversion with a current density of 400 mA cm^{-2} at 1.446 V *vs.* RHE and 97% FE of FA (Fig. 9a).[149] DFT calculations reveal that Bi doping modulates the active sites of Co_3O_4, promoting OH* generation at adjacent Co^{2+}(Td) sites and facilitating C–C bond cleavage, while significantly lowering the energy barrier of the rate-determining step (from 1.00 to 0.67 eV). Electronic structure analysis further indicates that Bi enhances Co–O covalency and reduces charge-transfer energy, thereby accelerating C–C cleavage and enabling more efficient FA production. He *et al.* demonstrated that the incorporation of Co into $Ni(OH)_2$ enabled a current density of 100 mA cm^{-2} at 1.35 V with 94.3% formate selectivity.[150] DFT calculations and *in situ* Raman measurements indicate that proton deintercalation from the hydroxide lattice is a key step in the glycerol oxidation process. The high deprotonation energy of Ni hydroxide (2.73 eV) limits the glycerol oxidation rate, whereas Co doping lowers the deprotonation energy (NiCo: 2.37 eV), accelerating proton deintercalation, exposing more active oxygen sites, and thereby facilitating charge transfer during C–C bond cleavage and enhancing the overall reaction efficiency. Besides catalyst design, cation effects in the electrochemical microenvironment are another key factor controlling formate selectivity. Catalyzed by NiOOH, Gong *et al.* found that alkali metal cations (Li^+, K^+, *etc.*) interacted specifically with glyceraldehyde intermediates, significantly altering the product distribution of glycerol electrooxidation (Fig. 9b).[151] Li^+ can stabilize the aldehyde intermediates, suppress oxidative pathways, and promote non-oxidative C–C bond cleavage. In the LiOH electrolyte, *in situ* IRRAS revealed that the aldehyde intermediates appeared during the first scan but rapidly vanished, while the glycerate signals were weakened, indicating suppressed oxidative pathways. DFT calculations further showed an adsorption energy trend of $Li^+ > K^+ >$ no cations, suggesting that cation–intermediate interactions weakened the adsorption of aldehydes on the NiOOH surface, favoring C–C bond cleavage and directing product selectivity.

Compared with FA, the selective generation of C2 products is more challenging due to uncontrollable C–C bond cleavage in glycerol. Moreover, each C2 molecule formed generates one FA molecule. Consequently, high selectivity of C2 products requires catalysts that balance C–C bond cleavage activity and oxidation capability. The Au-based catalyst has been found to be suitable for generating C2 products. Zhang *et al.* achieved the electro-conversion of glycerol to glycolate using a carbon nanotube-supported gold catalyst (Au/CNT) in alkaline electrolyte, with up to 85% glycolate selectivity at 50% glycerol conversion.[152] Kim *et al.* prepared nanostructured Au catalysts *via* electrochemical reduction of anodically treated Au films, achieving 50.9% glycerol conversion and 47% glycolic acid selectivity under optimized conditions (1.0 V *vs.* RHE, 1 M KOH, 2 h) due to enhanced facet-dependent OH adsorption at (100) and (110) sites and increased surface area (Fig. 9c).[153] Similarly, Shen *et al.* developed hollow bimetallic Au_1Cu_1 catalysts, delivering 90% glycerol conversion and 45% glycolic acid selectivity.[154] To gain insights into the role of copper in the Au_1Cu_1 catalyst, electrochemical *in situ* FTIR and DFT studies were conducted to investigate the glycerol reaction pathways. The results indicate that Au_1Cu_1 exhibits stronger adsorption of glycerol and its intermediates compared to monometallic Au, favoring the formation of glyceric acid, glycolic acid, and formic acid, whereas Au tends to produce lactic acid. Notably, tartronic acid, although detected in the FTIR spectra, was absent from the solution after 30 min over Au_1Cu_1, suggesting strong surface adsorption and subsequent cleavage, which explained the increased yields of glycolic acid and formic acid. These findings highlight the crucial role of copper in enhancing the adsorption capacity and directing product selectivity on Au_1Cu_1. Compared with precious metals, non-precious metals have cost advantages. Gong *et al.* regulated C1/C2 (formate/oxalate) selectivity in glycerol electro-reforming by incorporating phenanthrolines with electron-donating/withdrawing groups into $Ni(OH)_2$. *In situ* Raman spectroscopy and ultraviolet photoelectron spectroscopy (UPS) analysis indicate that electron-donating groups promoted (–OMe) C–C cleavage to product FA (C1), while electron-withdrawing groups ($-NO_2$) accelerated oxidation to oxalate (C2). Selectivity correlated linearly with Hammett parameters, with Ni-phen-NO_2 achieving 45.3% FE for oxalate in 2 M KOH (Fig. 9d).[155]

Glucose is a common small molecule derived from biomass. During the electro-oxidation of glucose to FA, Ni- and Co-based catalysts exhibit excellent C–C bond cleavage performance. Wang *et al.* developed a nanostructured NiCoP catalyst supported on 3D Ni foam, achieving efficient glucose electrooxidation to FA with 85% yield and a current density of 200 mA cm^{-2} at 1.47 V *vs.* RHE.[156] The mechanism involves anodic oxidative reconstruction of the catalyst to form a sandwich-structured NiCoOOH/NiCoP/Ni foam, where NiCoOOH serves as the active site for glucose oxidation, while NiCoP facilitates electron conduction to synergistically enhance the reaction efficiency (Fig. 9e). Co doping lowers the Ni oxidation potential and facilitates the Ni to NiOOH transformation, thereby enhancing activity. *In situ* Raman and colorimetric tests confirm an indirect oxidation pathway, where oxidized NiCoOOH spontaneously converts sugars into formic acid. Post-reaction characterization studies further show that bulk NiCoP remains intact while an amorphous NiCoOOH layer forms on the surface, clarifying the structure–activity relationship. Chen *et al.* developed a nanostructured NiCuO catalyst

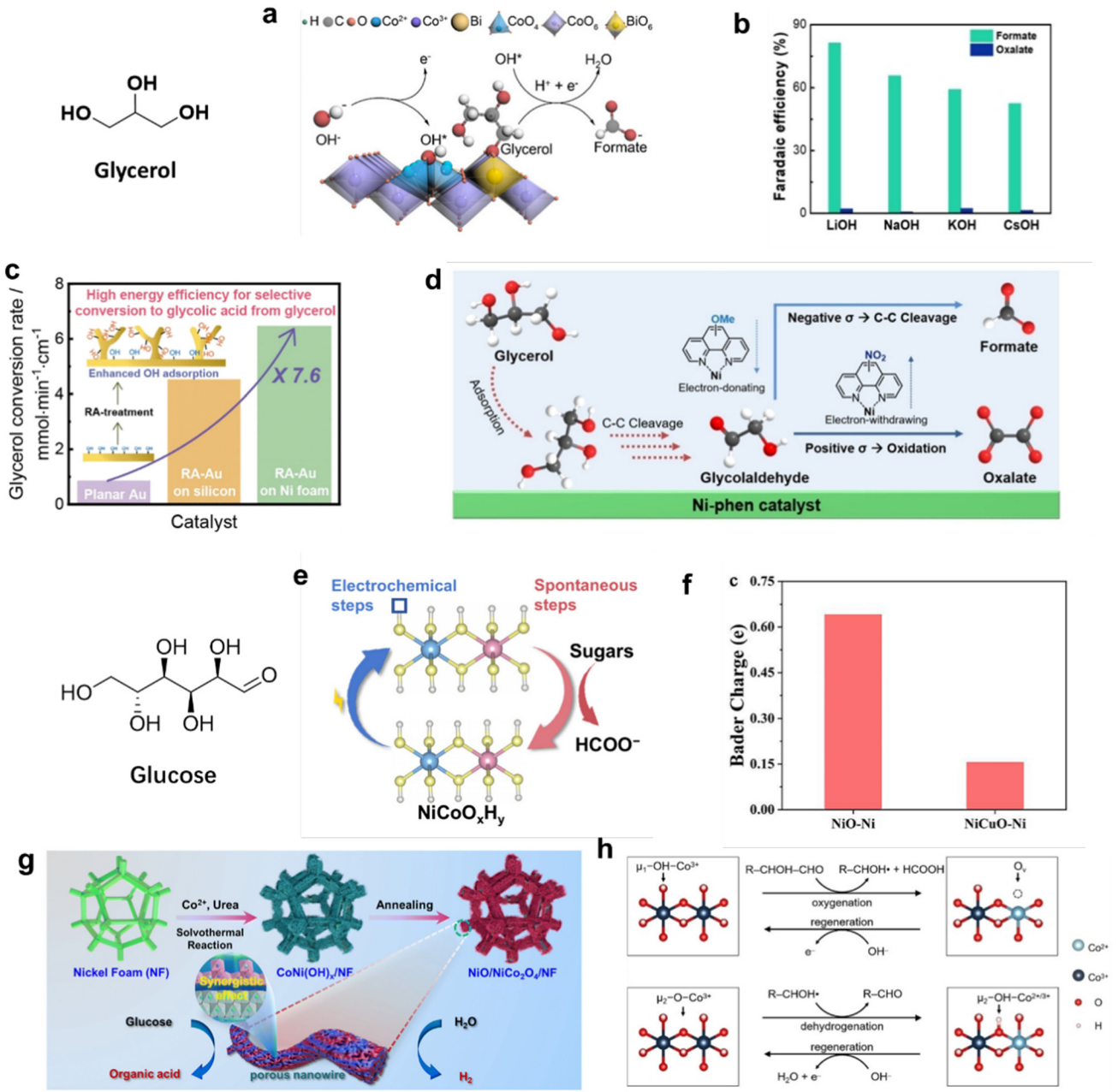

Fig. 9 (a) Schematic illustration of the promoting effects of single-atom Bi doping on the coadsorption of OH* and glycerol; reproduced from ref. 149 with permission from the American Chemical Society, copyright 2022. (b) FEs of the glycerol oxidation products under 1.5 V *vs.* RHE for 30 min in different alkaline solutions and 0.1 M glycerol; reproduced from ref. 151 with permission from Wiley-VCH GmbH, copyright 2022. (c) Schematic of the mechanism of glycerol oxidation with OH and adsorption of intermediates on the surface of planar and RA–Au catalysts; reproduced from ref. 153 with permission from the American Chemical Society, copyright 2021. (d) Schematic illustration of the glycerol oxidation pathway and its correlation with the Hammett parameters; reproduced from ref. 155 with permission from Wiley-VCH GmbH, copyright 2023. (e) Reaction cycle diagram of electrocatalytic polyol on NiCoP/NF; reproduced from ref. 156 with permission from the American Chemical Society, copyright 2024. (f) Bader charge of the Ni atom in NiCuO and NiO; reproduced from ref. 157 with permission from Elsevier, copyright 2024. (g) Schematic illustration of the synthesis process for $NiO/NiCo_2O_4$/NF; reproduced from ref. 158 with permission from Elsevier, copyright 2024. (h) The roles of μ_1-OH–Co^{3+} and μ_2-O–Co^{3+} in the GOR under alkaline conditions; reproduced from ref. 159 with permission from Wiley-VCH GmbH, copyright 2023.

derived from a bimetallic NiCu alloy on 3D Ni foam, achieving 94.6% FE and 93.3% selectivity for FA at 1.29 V (360 mV lower than water splitting).[157] DFT analysis revealed that Cu incorporation reduced the Ni Bader charge in NiCuO, enhancing the electron density for proton release (Fig. 9f), while the Ni d-band center closer to the Fermi level improved intermediate adsorption/desorption and the catalytic activity. In addition, Zhang *et al.* constructed a $NiO/NiCo_2O_4$ porous nanowire heterostructure on nickel foam, leveraging the high specific surface area and rapid mass transfer capability of the one-

dimensional porous structure, enhanced electron transfer *via* bicomponent interfacial synergy, and modulation of the d-band center by bimetallic sites to optimize the intermediate adsorption energy, thereby achieving an efficient electrocatalytic performance for the glucose oxidation reaction (Fig. 9g).[158] Duan *et al.* used cobalt oxyhydroxide (CoOOH) as a catalyst and employed DFT to investigate the C–C bond cleavage mechanism in glucose oxidation.[159] The results indicate that cleaving the C–C bond in R–CHOH–CHO to generate HCOOH and R–CHO involves simultaneous oxidation and dehydrogenation driven by two oxygen species: μ_1-OH–Co^{3+} oxidizes the CHO group to form HCOOH, while μ_2-O–Co^{3+} abstracts the H atom from R–CHOH to generate R–CHO (Fig. 9h). Recently, Ma *et al.* prepared bimetallic oxide ultrathin nanosheets with Ni–O–Co electronic channels on nickel foam (NiCoO–NS/NF) *via* a Cl^--corrosion and calcination strategy. Leveraging the abundant active sites from the ultrathin structure, efficient electron channels formed by Co^{2+}-mediated electron migration from Ni to Co *via* μ-O ligands, and rapid NiOOH active species formation, NiCoO-NS/NF achieved a current density of 222.7 mA cm^{-2} (at 1.4 V *vs.* RHE) and over 90% FE for glucose electrooxidation.[160] DFT analysis further revealed the mechanistic pathway of glucose oxidation. NiOOH-mediated glucose conversion begins with dehydrogenation at the α-H position, forming CH_2OH–$(CHOH)_3$–CHO–CHO, which adsorbs onto the NiOOH surface. Under applied potential, it transfers an electron to the circuit, generating $C_6H_{11}O_6$*. α-C is then oxidized by NiOOH, inducing C–C bond cleavage to yield arabinose and formate, while NiOOH is reduced to $Ni(OH)_2$ and subsequently regenerated. Iterative oxygenation, C–C cleavage, and dehydrogenation continue until HCHO* is formed, which hydrates to the *gem*-diol ($H_2C(OH)_2$*) and is finally dehydrogenated by NiOOH to produce formate as the final product. Table 7 highlights the synergistic impact of catalyst composition and electrolyte environment on the deep oxidation of polyols. The data reveal that Ni-based non-noble systems (*e.g.*, Ni–Mo–N/CFC and NiCoP/NF, entries 1 and 21) exhibit superior C–C bond cleavage capabilities at 1.3–1.5 V, converting glucose or glycerol into FA with high selectivities (>85%). In contrast, while Au-based noble metal systems (entries 10–17) are capable of driving the reaction, they generally underperform compared to optimized transition-metal heterostructures in terms of selectivity or potential requirements. Furthermore, the performance of $Ni(OH)_2$/NF in various alkaline media (entries 6–9) underscores the critical role of electrolyte cations (*e.g.*, Li^+) in enhancing fara-

Table 7 Summary of the electrochemical performance of representative catalysts for C–C bond cleavage of polyols

No.	Catalyst	Electrolyte	Conc. (mM)	Potential (V *vs.* RHE)	Conv. (%)	Sel. (%)	FE (%)	Catalyst stability (h)	Deactivation mechanism	Ref.
1	Ni–Mo–N/CFC[a]	1.0 M KOH	100 (glycerol)	1.30	100	92(FA)	96	—	—	147
2	$CuCo_2O_4$ [a]	0.1 M KOH	100 (glycerol)	1.30	79.7	80.6(FA)	89.1	5	Substrate depletion and pH drop	148
3	$NiCo_2O_4$ [a]	0.1 M KOH	100 (glycerol)	1.26	61.6	65.3(FA)	85.5	—	—	148
4	Bi–Co_3O_4 [b]	1.0 M KOH	100 (glycerol)	1.35	—	97.0(FA)	97.1	200	Potential leaching of Bi species	149
5	NiCo hydroxide[b]	1.0 M KOH	100 (glycerol)	1.474	—	94.3(FA)	100	90	—	150
6	$Ni(OH)_2$/NF[a]	2.0 M LiOH	100 (glycerol)	1.50	—	—	81.3	24 (crude glycerol)	Impure component of the crude glycerol	151
7	$Ni(OH)_2$/NF[a]	2.0 M NaOH	100 (glycerol)	1.50	—	—	73.0	—	—	151
8	$Ni(OH)_2$/NF[a]	2.0 M KOH	100 (glycerol)	1.50	—	—	64.0	—	—	151
9	$Ni(OH)_2$/NF[a]	2.0 M CsOH	100 (glycerol)	1.50	—	—	—	—	—	151
10	Au/CNT[b]	2.0 M KOH	1000 (glycerol)	2.44	50	85(GLOA)	—	12	—	152
11	RA-Au on Si[b]	1.0 M KOH	100 (glycerol)	1.0	72.4	46.6(GLOA)	—	2	—	153
12	RA-Au on NF[b]	1.0 M KOH	100 (glycerol)	1.0	68.7	41.2(GLOA)	—	2	—	153
13	Planar Au[b]	1.0 M KOH	100 (glycerol)	1.0	12.4	42.3(FA)	38.66	2	—	153
14	Au1Cu1[b]	1 M KOH	100 (glycerol)	1.23	72.9	48.3(GLOA)	40.4	C	Consumption of electrolyte solution	154
15	Au1Cu2[b]	1 M KOH	100 (glycerol)	1.23	59.9	43.0(GLOA)	46.5	—	—	154
16	Au2Cu1[b]	1 M KOH	100 (glycerol)	1.23	50.4	47.1(GLOA)	48.4	—	—	154
17	Au[b]	1 M KOH	100 (glycerol)	1.23	53.9	34.2(LA)	15.2	—	—	154
18	$Ni(OH)_2$ [b]	2 M KOH	100 (glycerol)	1.50	—	—	40.0	—	—	155
19	Ni-phen-NO_2 [b]	2 M KOH	100 (glycerol)	1.50	—	—	45.3	50	—	155
20	Ni-phen-OMe[b]	2 M KOH	100 (glycerol)	1.50	—	—	92.7	—	—	155
21	NiCoP/NF[c]	1 M KOH	50 (glucose)	1.47	100	85.2(FA)	82.0	4 (8 cycles)	—	156
22	NiCuO[b]	1.0 M KOH	100 (glucose)	1.15	100	93.3(FA)	94.6	24	—	157
23	NiO/$NiCo_2O_4$/NF[b]	1.0 M KOH	100 (glucose)	1.45	—	72.0(FA)	100	24	Change in the substrate concentration and pH value	158
24	CoOOH/CC[c]	1.0 M KOH	100 (glucose)	1.48	—	—	74.0	30	—	159
25	NiCoO-NS/NF[b]	1.0 M KOH	100 (glucose)	1.50	95.6	71.0(FA)	73.2	50	—	160

GlOA: glycolic acid; LA: lactic acid; FA: formic acid. [a] Single-cell. [b] H-cell. [c] Flow-cell.

daic efficiency. In conclusion, the rational design of transition-metal heterojunctions combined with electrolyte microenvironment optimization offers a highly effective, low-energy alternative to noble metals for the sustainable valorization of complex polyols into high-value small-molecule organic acids. Catalyst stability is equally crucial for continuous C–C bond cleavage processes. As shown in Table 7, Ni- and Co-based non-precious metal catalysts demonstrate stability ranging from several to tens of hours during the deep oxidation of glucose and glycerol. However, under high substrate concentrations, strongly alkaline conditions, or prolonged operation, deactivation may occur due to oxidation of active sites, surface reconstruction, or drastic local pH changes during the reaction. For example, the deactivation of $CuCo_2O_4$ (entry 2) is associated with substrate depletion and pH decrease. Therefore, developing new catalyst systems that maintain structural stability and resist deactivation under industrial operating conditions is essential for achieving the efficient electrolytic refining of biomass-derived polyols.

The accurate resolution of reaction pathways is the cornerstone of electrocatalytic mechanism research, yet traditional H-type electrolytic cells are prone to artifacts due to the poor stability of reactive intermediates. A prime example is the electro-oxidation of glucose to formic acid, which was long believed to proceed *via* the aldonic acid route. Duan *et al.* overturned this conventional wisdom by deploying a single-pass continuous flow reactor (SPCFR). Through the optimization of fluid dynamics and a separated feeding strategy, they effectively mitigated the non-faradaic degradation of aldehyde intermediates. By integrating an *in situ* acid-quenching mechanism within the SPCFR, the team successfully captured transient aldehyde species, thereby validating that the reaction proceeded *via* a stepwise α-scission aldose route. Beyond mechanistic insights, the nine-module stacked SPCFR exhibited exceptional productivity (81.8% single-pass conversion; 562.8 mM concentration), bridging the gap between fundamental mechanistic inquiry and scalable biomass upgrading.[96] With the reaction mechanism clarified, the next frontier lies in the precise manipulation of C–C bond cleavage depth to maximize product value. Ma *et al.* addressed this by designing a Pt@Ni$(OH)_{2-x}$ catalyst enriched with Ni–O–Pt interfaces and oxygen vacancies. This architecture enabled the tunable electro-oxidation of glycerol, allowing for a decisive switch between C–C bond preservation (C2 pathway) and deep scission (C1 pathway). At industrial current densities, the system delivered remarkable selectivities for glycolic acid (95%) and formic acid (92%). A solar-powered reactor with an Internet system-integrated reactor platform facilitated the 'one-click switching' of target products from real-world substrates, underscoring the transformative potential of controllable C–C activation in sustainable plastic upcycling and biorefineries.[161]

4.2 Lignin depolymerization: strategies for C–C bond cleavage

Lignin, a major component of lignocellulosic biomass, is the largest natural source of renewable aromatics, offering significant potential to replace fossil resources in producing high-value chemicals.[162,163] Electrooxidation can selectively break C–C bonds in lignin, such as C_α–C_β bonds in the β-O-4 linkages, under mild conditions through catalyst design or applied potential/current regulation. Selective cleavage of C_α–C_β bonds or C_β–O bonds can improve the yield of target products. However, selective cleavage of C_α–C_β bonds (84–90 kcal mol^{-1}) is particularly challenging due to their higher dissociation energy compared to C_β–O bonds (62–70 kcal mol^{-1}).[164,165] Therefore, enhancing the activity and selectivity of the catalyst remains a key research focus.

The β-O-4 linkage, which constitutes nearly 50% of lignin's structural units, poses significant challenges for selective cleavage due to a high C_α–C_β bond dissociation energy, poor selectivity control, and steric hindrance, creating a major bottleneck for lignin's targeted conversion into high-value chemicals.[145,166,167] Wang *et al.* reported a strategy employing an atomically dispersed platinum electrocatalyst (Pt_1/N-CNTs) to facilitate C_α–C_β bond cleavage by promoting C_β radical intermediates (Fig. 10a).[168] DFT calculations revealed that *tert*-butyl hydroperoxide (^{t}BuOOH), used as a radical initiator, generated ^{t}BuO• or ^{t}BuOO• radicals *via* highly exothermic processes (−2.85 eV and −2.32 eV, respectively), which subsequently underwent C–O coupling with C_β radicals to form an unstable adduct. The adduct readily undergoes C_α–C_β bond cleavage, producing benzaldehyde, phenyl formate, and *tert*-butanol, achieving 99% dimer conversion and 81% benzaldehyde yield. Similarly, Fang *et al.* proposed a method for breaking the C_α–C_β bond using a dodecyl sulfate-intercalated cobalt sulfide (DS-CoS) nanocone catalyst.[169] DFT calculations indicate that surface Co^{2+} on DS-CoS nanocones is oxidized to $Co^{3+}OH$ at low potential, generating hydroxyl radicals, which abstract an H-atom from C_α–OH of β–O–4 to form C_α–O$^\bullet$, which significantly reduces the C_β–O bond dissociation energy from 64 to 40 kcal mol^{-1}, thereby enabling adjacent C–C bond cleavage *via* β-scission (Fig. 10b).

Phenethyl alcohol and its derivatives with C(OH)–C or C(O)–C units are commonly used as model compounds to imitate the study of the β-O-4 bond. Duan *et al.* reported a novel C–C bond scission mechanism using a manganese-doped cobalt oxyhydroxide (MnCoOOH) catalyst with phenethyl alcohol and acetophenone as substrates (Fig. 10c).[170] Mechanistic studies indicate that C_α–C_β bond cleavage is driven by *in situ*-generated OH* radicals under alkaline conditions, proceeding *via* the generation of OH (barrier: 1.29 eV) rather than the more energetically demanding deprotonation step (1.66 eV). Specifically, phenethyl alcohol undergoes α-hydrogen (H_α) deprotonation to form a nucleophilic alkoxide. Subsequently, the adsorbed hydroxyl radical (OH*) species promote β-hydrogen (H_β) elimination to generate the corresponding ketone. Hydroxide ions facilitate the formation of a carbanion intermediate during keto–enol tautomerization that is readily attacked by electrophilic OH* to yield 2-hydroxyacetophenone. Benzoate is ultimately formed through dehydrogenation, geminal diol formation, and C–C bond cleavage.

Ketone–alcohol (KA) oil, derived from the hydrogenation of lignin-derived phenolics, primarily comprises cyclohexanol

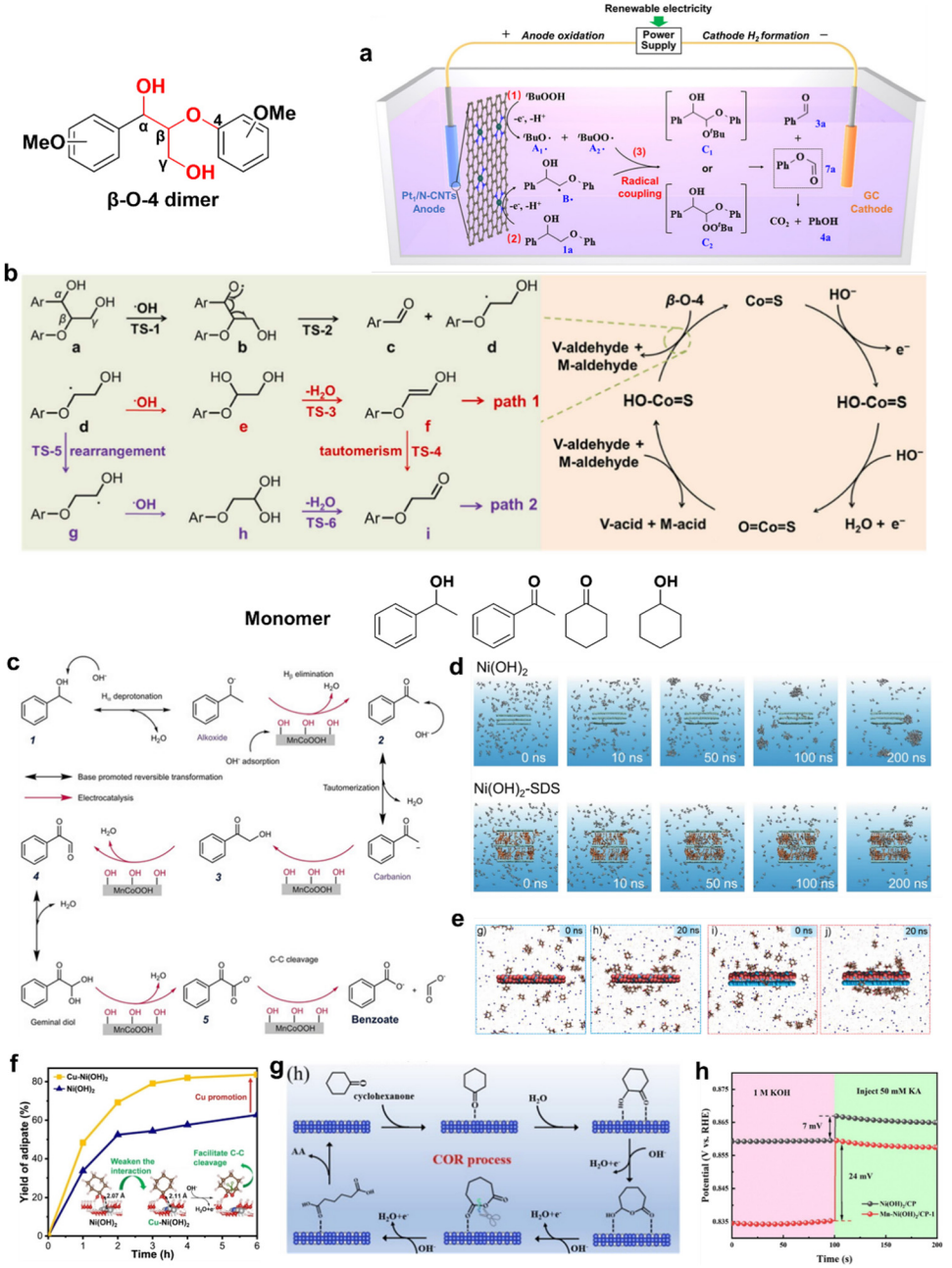

Fig. 10 (a) Proposed mechanism of Pt_1/N-CNT-catalyzed conversion of 2-phenoxy-1-phenylethanol (representative β-O-4 dimeric model compound); reproduced from ref. 168 with permission from the American Chemical Society, copyright 2021. (b) Proposed mechanism for the electrocatalytic oxidation of β-O-4 over DS-CoS nanocones; reproduced from ref. 169 with permission from Elsevier, copyright 2023. (c) A plausible tandem nucleophilic oxidation reaction (NOR) mechanism for the electrochemical oxidation of 1-phenylethanol; reproduced from ref. 170 with permission from Wiley-VCH GmbH, copyright 2021. (d) The time sequence of typical snapshots of cyclohexanone diffusion dynamics on pure $Ni(OH)_2$ and $Ni(OH)_2$-SDS; reproduced from ref. 172 with permission from Springer Nature, copyright 2022. (e) The time sequence of typical snapshots of cyclohexanone diffusion dynamics on (g and h) Co_3O_4 and (i and j) Co_3O_4/GDY; reproduced from ref. 173 with permission from Wiley-VCH GmbH, copyright 2023. (f) The electrooxidation performance of cyclohexanol to adipic acid over Cu–$Ni(OH)_2$ and $Ni(OH)_2$; reproduced from ref. 174 with permission from Wiley-VCH GmbH, copyright 2022. (g) The proposed reaction process for the cyclohexanol/cyclohexanone oxidation reaction on the $Cu_{0.81}Ni_{0.19}$ catalyst; reproduced from ref. 175 with permission from Elsevier, copyright 2025. (h) OCP curves of Mn–$Ni(OH)_2$/CP-1 and $Ni(OH)_2$/CP in 1 M KOH and 0.1 M KA oil; reproduced from ref. 176 with permission from the American Chemical Society, copyright 2024.

and cyclohexanone. Electrocatalytic oxidation of KA oil offers a sustainable alternative route for synthesizing adipic acid, a critical structural unit in industrial nylon 66 production. In the oxidation of KA oil, the cleavage of C(OH)–C bonds within cyclohexanol and C(O)–C bonds within cyclohexanone represents the core step for achieving the synthesis of adipic acid.

Ni-based catalysts have garnered significant attention due to their excellent activity in KA oil electrooxidation. In 2004, Petrosyan *et al.* reported the electrocatalytic oxidation of KA oil to adipic acid using a nickel oxyhydroxide (NiOOH) catalyst.[171] However, the low current density remains an unresolved issue. To enhance the performance of Ni-based catalysts, Duan *et al.* proposed an electrocatalytic strategy using sodium dodecyl sulfonate (SDS)-modified nickel hydroxide ($Ni(OH)_2$), achieving efficient electrocatalytic oxidation of cyclohexanone to adipic acid (Fig. 10d).[172] Crucially, SDS intercalation promotes the enrichment of immiscible cyclohexanone in the aqueous phase, resulting in a 3.6-fold enhancement in adipic acid productivity and a FE increase from 56% to 93% compared to unmodified $Ni(OH)_2$. To elucidate the diffusion mechanism of cyclohexanone from the bulk electrolyte to the catalyst surface, coarse-grained molecular dynamics (CGMD) simulations were performed. The results indicate that cyclohexanone exhibits low affinity toward the $Ni(OH)_2$ surface and predominantly remains in the bulk solution, whereas on SDS-intercalated Ni $(OH)_2$, cyclohexanone primarily accumulates at the nanosheet edges, facilitating its oxidation. DFT calculations further reveal that during KA oil electrooxidation, cyclohexanol is first dehydrogenated on NiOOH to form cyclohexanone, which can reversibly convert into enol or *gem*-diol intermediates under alkaline conditions. Subsequent nucleophilic dehydrogenation generates cyclohexane-1,2-dione, which is finally oxidized to adipic acid. Similarly, Chen *et al.* employed a synergistic substrate enrichment and adsorption activation strategy by constructing a Co_3O_4/graphdiyne (GDY) interfacial system.[173] They utilized the hydrophobic π domain of GDY to enrich cyclohexanone and simultaneously adjusted the d-band center of Co sites to enhance adsorption activation, achieving efficient adipic acid production (Fig. 10e). To investigate the synergistic effect of Co_3O_4 and GDY on adsorption and catalytic performance, DFT calculations and MD simulations were performed. The results show significant interfacial charge transfer between GDY and Co_3O_4, which shifts the d-band center of Co sites closer to the Fermi level, enhancing the adsorption and activation of cyclohexanone, H_2O, and OH^-. MD simulations indicate that cyclohexanone is dispersed in the bulk electrolyte over Co_3O_4, while it predominantly accumulates at the edges of Co_3O_4/GDY nanosheets, favoring electrocatalytic oxidation. In addition, Wang *et al.* utilized Cu^{2+}-doped $Ni(OH)_2$ electrocatalysts, achieving 84% yield and 87% selectivity for adipic acid *via* cyclohexanol oxidation (Fig. 10f).[174] To elucidate the reaction pathway and intermediates, *in situ* IRRAS measurements were conducted on $Ni(OH)_2$ and 2% Cu–$Ni(OH)_2$. During electrolysis, cyclohexanol characteristic peaks gradually decreased, while cyclohexanone peaks appeared transiently before disappearing, leading to the formation of adipic acid; additional peaks at 1314 and 1190 cm^{-1} were attributed to accumulated intermediates. Cu^{2+} doping accelerated the consumption of cyclohexanone and suppressed intermediate accumulation, indicating that Cu facilitated C–C bond cleavage by promoting radical formation. DFT calculations further revealed that cyclohexanol first adsorbed and lost a hydroxyl hydrogen to form radicals, followed by cyclohexanone formation and C_α–C_β bond cleavage to yield adipic acid. Cu doping substantially lowers the energy barrier for radical generation (from +0.54 to −1.02 eV), thereby accelerating the oxidation process. Recently, Chen *et al.* developed 3D dendritic nickel–copper alloy arrays ($Cu_{0.81}Ni_{0.19}$/NF) *via* electrodeposition, achieving co-electrosynthesis of adipic acid from KA oil (>90% FE, 0.6 mmol h^{-1} yield) in a membrane-free flow electrolyzer.[175] *In situ* spectroscopy reveals that the alloy promotes the direct formation of active NiOOH species for cyclohexanone-to-adipic acid conversion through 2-hydroxycyclohexanone and 2,7-oxepanedione intermediates (Fig. 10g). DFT calculations indicate that cyclohexanone adsorption on $Cu_{0.8}Ni_{0.2}$ (−1.82 eV) is lower than that on Ni (−1.77 eV) and Cu (−1.40 eV), and differential charge density analysis shows enhanced electron density in the alloy layers, suggesting a significant electronic interaction between Ni and Cu. Furthermore, Mn can also enhance the electrochemical performance of $Ni(OH)_2$. Shen *et al.* achieved selective electrooxidative cleavage of C(OH)–C/C(O)–C bonds in KA oil to adipic acid (46.8% selectivity) at 50 mA mg^{-1} using Mn-doped $Ni(OH)_2$ freestanding electrodes, where Mn–Ni electronic interactions optimize substrate adsorption while maintaining oxygen evolution inertness (Fig. 10h).[176]

Optimizing the reactor design offers an effective route to address the depolymerization challenges posed by lignin's highly complex cross-linked network. Stiefel *et al.* innovatively constructed an electrochemical reaction system coupling a 3D structured electrode with membrane separation technology, achieving efficient lignin depolymerization at ambient temperature and pressure. Benefiting from this unique reactor design, the system effectively disrupts intricate C–C and C–O bond networks within 4 h, converting lignin into monomers. Crucially, by integrating membrane filtration, the system successfully realizes the continuous online separation of products, offering a new paradigm for mild lignin conversion.[177] Building upon efficient depolymerization and separation, exploring energy coupling and product valorization becomes increasingly significant. Se-Jun Yim *et al.* designed an integrated modular flow system utilizing redox-active phosphomolybdic acid (PMA) as both a catalyst and an electron mediator. This approach successfully achieved the synergistic co-production of continuous lignin valorization and low-voltage green hydrogen. Through tandem flow operation, the system effectively circumvents the energy-intensive oxygen evolution reaction (OER), reaching a hydrogen production current density of 20.5 mA cm^{-2} at a low voltage of 1.5 V. This provides a novel paradigm for coupling biomass conversion with energy storage.[178]

Electrocatalytic C–C bond cleavage in biomass-derived compounds is a pivotal strategy for biomass valorization. Transition metal-based catalysts (*e.g.*, Ni, Co) enhance the reaction efficiency through structural optimization, but challenges include ambiguous mechanisms, catalyst stability, and product selectivity. Additionally, while most current research focuses on model compounds like glucose, the electrocatalytic conversion of native biomass materials (*e.g.*, lignin, crude glycerol) remains underdeveloped due to complex challenges

arising from multicomponent mixtures, including competing reactions, mass transfer resistance, and catalyst degradation. Therefore, future efforts should leverage high-precision theoretical calculations and machine learning to decode the dynamic mechanisms of C–C bond cleavage in model compounds and establish structure–activity relationship models, while simultaneously conducting studies on native biomass conversion to reveal the interaction rules between their components and catalyst surfaces, thereby overcoming selectivity and stability hurdles to facilitate the transition of electrocatalysis from model systems to practical applications.

5. Conclusions and perspectives

Electrocatalytic bond activation has emerged as a transformative strategy for sustainable biomass valorization, enabling precise molecular reconstruction under mild conditions. This review comprehensively analyzed the mechanisms, catalyst design principles, and reaction engineering strategies for the activation of C–H, C–O, and C–C bonds in key biomass platforms (*e.g.*, glucose, glycerol, HMF, lignin derivatives). Key conclusions and future perspectives are outlined as follows.

5.1 Key advances

In terms of mechanistic insights, significant progress has been made in understanding the activation of different bonds. For the C–H bond, surface-mediated PCET pathways enable the selective oxidation of carbohydrates (such as glucose C1/C6), polyols (like glycerol primary/secondary –OH), and furans (including HMF aldehyde/hydroxymethyl). This achieves high-value products (glucaric acid, DHA, FDCA) with over 90% selectivity. Regarding the C–O bond, reductive hydrogenolysis (*via* H_{ads} species) and oxidative cleavage (*via* ROS such as $^{\bullet}OH/^{\bullet}O_2^-$) allow for the selective scission of lignin β-O-4 linkages and furfural C=O bonds, yielding monomeric aromatics and BHMF with FE exceeding 95%. As for the C–C bond, radical-driven (*e.g.*, $^{\bullet}OH$) or bifunctional-site-mediated cleavage strategies convert lignin C–C bonds and polyols (glycerol/glucose) into adipic acid, formate, and glycolate, overcoming high bond dissociation energies. In catalyst innovations, electronic modulation through methods such as alloying, doping, and heterojunctions optimizes d-band centers to enhance bond adsorption and activation. Structural engineering, including the development of single-atom catalysts, high-entropy alloys, and defect-rich oxides, maximizes atomic efficiency and stabilizes intermediates. Interface design with synergistic sites helps suppress side reactions like C–C cleavage and over-oxidation. Process optimization has also seen advancements. Potential-dependent selectivity, such as low potential for C3 retention in glycerol oxidation, allows for controlled reactions. pH-controlled pathways, where alkaline media are suitable for C–H oxidation and neutral media are favorable for C=O hydrogenation, contribute to efficient processes. In addition, the rational design of catalysts coupled with the synergistic innovation of reactor engineering serves as the twin pillars underpinning the evolution of biomass electrocatalysis. Advanced reactor configurations, such as flow cells and SPE systems, have proved to be instrumental in optimizing mass transport and steering reaction pathways, thereby successfully spanning the divide between fundamental mechanistic exploration (*e.g.*, intermediate capture) and engineering-scale application. The development of intelligent, integrated platforms that combine conversion, separation, and energy coupling represents a critical frontier. Such an integrated approach is necessary to overcome existing technological barriers and enable viable commercial-scale industrialization.

5.2 Persistent challenges

Selectivity control remains a major hurdle, particularly in differentiating chemically similar bonds, such as primary *versus* secondary –OH in glycerol and C_α–C_β *versus* C_β–O in lignin. Additionally, suppressing competing reactions, such as furan ring opening during HMF reduction and repolymerization of lignin fragments, poses significant challenges. Catalyst limitations are another key issue. The dependence on noble metals (*e.g.*, Pt/Pd for C–H activation) leads to high costs. Deactivation due to the strong adsorption of intermediates or products (*e.g.*, glucaric acid poisoning) and structural instability under operational conditions (*e.g.*, aggregation of single-atom sites) further restricts the efficiency and longevity of catalysts. System compatibility is also problematic. The reliance on harsh electrolytes (*e.g.*, strong alkalis cause corrosion) can limit the applicability of the processes. Low mass transfer efficiency for macromolecular biomass (*e.g.*, lignin) and scalability barriers in coupled reactions (*e.g.*, anodic oxidation/cathodic reduction pairing) hinder the practical implementation of electrocatalytic bond activation for biomass valorization.

5.3 Future perspectives

For next-generation catalysts, bio-inspired precision is a promising direction, involving the design of catalysts with spatial confinement (*e.g.*, SACs@MOFs) or multiple interaction sites to distinguish similar functional groups. At present, achieving peak performance in electrocatalysis remains heavily reliant on precious metal catalysts, particularly for C–H bond activation. Consequently, there is an urgent need to develop non-precious metal catalysts (*e.g.*, Ni, Fe, and Cu-based materials) that exhibit noble-metal-like activity. Additionally, creating dynamic interfaces with self-healing or potential-adaptive surfaces to resist poisoning can enhance catalyst stability. Mechanism-driven innovation will play a vital role. The use of *in situ*/*operando* techniques, such as time-resolved spectroscopy (*e.g.*, IR, Raman) and computational AI, to map reaction dynamics at solid–liquid interfaces can deepen our understanding of the underlying processes. Machine learning applications to predict bond dissociation pathways and optimize catalyst descriptors (*e.g.*, d-band center, O/P adsorption energy) will accelerate catalyst development. Integrated system design is another area of focus. Exploring mild-condition catalysis, such as non-oxygen-dependent pathways (*e.g.*, halogen-mediated radical reactions) for neutral-pH operation, can

improve process compatibility. Energy-coupled systems that pair anodic biomass oxidation with cathodic H_2O_2 production or CO_2 reduction to achieve net-zero energy consumption are also promising. Prioritizing native biomass valorization using real feedstocks (*e.g.*, crude glycerol, lignocellulose) over model compounds, while addressing multicomponent interference, is essential for practical applications. In terms of sustainability metrics, developing life-cycle assessment frameworks to quantify environmental and economic benefits (*e.g.*, carbon footprint, *E*-factor reduction) and establishing standardized testing protocols for catalyst stability (>1000 h operation) and product separation efficiency are necessary to ensure the long-term viability and sustainability of electrocatalytic biomass valorization.

Author contributions

Mengyuan Liu: conceptualization, investigation, methodology, data curation, visualization, writing – original draft preparation, writing – review & editing. Guohao Xu: formal analysis, software, visualization, writing – review & editing. Chendong Lin: formal analysis, software, visualization, writing – review & editing. Xiaotong Chen: supervision, validation, visualization, writing – review & editing. Wei Liu: supervision, validation, visualization, writing – review & editing. Shunji Xie: project administration, resources, funding acquisition, supervision, validation, visualization, writing – original draft preparation, writing – review & editing.

Conflicts of interest

There are no conflicts to declare.

Data availability

No primary research results, software or code has been included and no new data were generated or analysed as part of this review.

Acknowledgements

This work was supported by the National Natural Science Foundation of China (Nos. U24A20490, U23A2087, 22502161, W2412025), the Fujian Provincial Natural Science Foundation of China (No. 2024J011005), the Fundamental Research Funds for the Central Universities (Nos. 20720240123, 20720250005), and the China Postdoctoral Science Foundation funded project (No. 2024M761762).

References

1 J. Wang and W. Azam, Natural Resource Scarcity, Fossil Fuel Energy Consumption, and Total Greenhouse Gas Emissions in Top Emitting Countries, *Geosci. Front.*, 2024, **15**(2), 101757.
2 P. Achakulwisut, P. Erickson, C. Guivarch, R. Schaeffer, E. Brutschin and S. Pye, Global Fossil Fuel Reduction Pathways under Different Climate Mitigation Strategies and Ambitions, *Nat. Commun.*, 2023, **14**(1), 5425.
3 N. Tripathi, C. D. Hills, R. S. Singh and C. J. Atkinson, Biomass Waste Utilisation in Low-Carbon Products: Harnessing a Major Potential Resource, *npj Clim. Atmos. Sci.*, 2019, **2**(1), 35.
4 M. Antar, D. Lyu, M. Nazari, A. Shah, X. Zhou and D. L. Smith, Biomass for a Sustainable Bioeconomy: An Overview of World Biomass Production and Utilization, *Renewable Sustainable Energy Rev.*, 2021, **139**, 110691.
5 C. Tian, R. Dorakhan, J. Wicks, Z. Chen, K.-S. Choi, N. Singh, J. A. Schaidle, A. Holewinski, A. Vojvodic, D. G. Vlachos, L. J. Broadbelt and E. H. Sargent, Progress and Roadmap for Electro-Privileged Transformations of Bio-Derived Molecules, *Nat. Catal.*, 2024, **7**(4), 350–360.
6 J. Zhang, J. Gu, R. Shan, H. Yuan and Y. Chen, Advances in Thermochemical Valorization of Biomass towards Carbon Neutrality, *Resour., Conserv. Recycl.*, 2025, **212**, 107905.
7 A. Yadav, V. Sharma, M.-L. Tsai, C.-W. Chen, P.-P. Sun, P. Nargotra, J.-X. Wang and C.-D. Dong, Development of Lignocellulosic Biorefineries for the Sustainable Production of Biofuels: Towards Circular Bioeconomy, *Bioresour. Technol.*, 2023, **381**, 129145.
8 J. Wang, J. Fu, Z. Zhao, L. Bing, F. Xi, F. Wang, J. Dong, S. Wang, G. Lin, Y. Yin and Q. Hu, Benefit Analysis of Multi-Approach Biomass Energy Utilization toward Carbon Neutrality, *Innovation*, 2023, **4**(3), 100423.
9 X. Yang, Y. Zhang, P. Sun and C. Peng, A Review on Renewable Energy: Conversion and Utilization of Biomass, *Smart Mol.*, 2024, **2**(4), e20240019.
10 R. Katahira, T. J. Elder and G. T. Beckham, *Chapter 1. A Brief Introduction to Lignin Structure, in Energy and Environment Series*, Royal Society of Chemistry, Cambridge, 2018, pp. 1–20.
11 J. S. Câmara, R. Perestrelo, R. Ferreira, C. V. Berenguer, J. A. M. Pereira and P. C. Castilho, Plant-Derived Terpenoids: A Plethora of Bioactive Compounds with Several Health Functions and Industrial Applications—A Comprehensive Overview, *Molecules*, 2024, **29**(16), 3861.
12 A. A. Latimer, A. R. Kulkarni, H. Aljama, J. H. Montoya, J. S. Yoo, C. Tsai, F. Abild-Pedersen, F. Studt and J. K. Nørskov, Understanding Trends in C–H Bond Activation in Heterogeneous Catalysis, *Nat. Mater.*, 2017, **16**(2), 225–229.
13 J. H. Docherty, T. M. Lister, G. Mcarthur, M. T. Findlay, P. Domingo-Legarda, J. Kenyon, S. Choudhary and I. Larrosa, Transition-Metal-Catalyzed C–H Bond Activation for the Formation of C–C Bonds in Complex Molecules, *Chem. Rev.*, 2023, **123**(12), 7692–7760.
14 Z. Qiu and C.-J. Li, Transformations of Less-Activated Phenols and Phenol Derivatives via C–O Cleavage, *Chem. Rev.*, 2020, **120**(18), 10454–10515.

15 L. Souillart and N. Cramer, Catalytic C–C Bond Activations via Oxidative Addition to Transition Metals, *Chem. Rev.*, 2015, **115**(17), 9410–9464.
16 N. L. Verma, M. Kumar, D. Sharma, Jaipal, S. Kumar, N. Rathore and G. Jaiswar, Transition-Metal-Mediated C-C Bond Activation: Recent Advances and Its Applications in Organic Synthesis, *Results Chem.*, 2023, **6**, 101130.
17 K. Wu, N. Lam, D. A. Strassfeld, Z. Fan, J. X. Qiao, T. Liu, D. Stamos and J. Yu, Palladium(II)–Catalyzed C–H Activation with Bifunctional Ligands: From Curiosity to Industrialization, *Angew. Chem., Int. Ed.*, 2024, **63**(19), e202400509.
18 J. He, M. Wasa, K. S. L. Chan, Q. Shao and J.-Q. Yu, Palladium-Catalyzed Transformations of Alkyl C–H Bonds, *Chem. Rev.*, 2017, **117**(13), 8754–8786.
19 S. Kang, J. Fu and G. Zhang, From Lignocellulosic Biomass to Levulinic Acid: A Review on Acid-Catalyzed Hydrolysis, *Renewable Sustainable Energy Rev.*, 2018, **94**, 340–362.
20 L. Du, Y. Shao, J. Sun, G. Yin, C. Du and Y. Wang, Electrocatalytic Valorisation of Biomass Derived Chemicals, *Catal. Sci. Technol.*, 2018, **8**(13), 3216–3232.
21 Y. Sun, J. Miao, X. Fan, K. Zhang and T. Zhang, Recent Progress in Electrochemical Conversion from Biomass Derivatives into High-Value-Added Chemicals, *Small Struct.*, 2024, **5**(7), 2300576.
22 F. W. S. Lucas, R. G. Grim, S. A. Tacey, C. A. Downes, J. Hasse, A. M. Roman, C. A. Farberow, J. A. Schaidle and A. Holewinski, Electrochemical Routes for the Valorization of Biomass-Derived Feedstocks: From Chemistry to Application, *ACS Energy Lett.*, 2021, 1205–1270.
23 Y. Ramli, V. Chaerusani, Z. Yang, R. Yang, J. Zhang, A. Abudula and G. Guan, Electrochemical Conversion of Biomass Derivatives to Value-Added Chemicals: A Review, *Green Carbon*, 2025, **3**(2), 113–129.
24 C. Lu, S. Yang, P. Shi, S. Huang, C. Cai, J. Zhu, X. Zhuang and T. Wang, Integrated Electrochemical Biomass Oxidation and CO_2 Reduction over Ultra–wide Potential Window, *Angew. Chem., Int. Ed.*, 2025, **64**(20), e202502846.
25 M. Zhang, Z. Zheng, X. Zhang, Z. Jiang, X. Yong, K. Li, X. Tu and K. Yan, Pairing Electrocatalytic Reduction and Oxidation of Biomass-Derived 5-Hydroxymethylfurfural into Highly Value-Added Chemicals, *JACS Au*, 2025, **5**(2), 937–947.
26 N. S. Weliwatte, H. Chen, T. Tang and S. D. Minteer, Three-Stage Conversion of Chemically Inert *n*-Heptane to α-Hydrazino Aldehyde Based on Bioelectrocatalytic C–H Bond Oxyfunctionalization, *ACS Catal.*, 2023, **13**(1), 563–572.
27 M. Dong, S. Jia, X. Chen, J. Jiao, C. Xue, Z. Xia, H. Cheng, T. Deng, C. Chen, K. Dong, H. Wu, M. He and B. Han, Cathode-Induced C–H Bond Heterolysis for Olefin Isomerization and Applications in Electrocarboxylation, *J. Am. Chem. Soc.*, 2025, **147**(23), 19976–19985.
28 P. Wu, L. Li, H. Li and Z. Fang, Interfacial High-Valence Ni (IV)-Enabled C-H Activation for Photoelectrochemical C-C Bond Cleavage of Lignin to Exclusively Produce Aromatic Carboxylic Acids, *Chem. Eng. J.*, 2024, **490**, 151722.
29 S. Rani, S. Aslam, K. Lal, S. Noreen, K. A. M. Alsader, R. Hussain, B. Shirinfar and N. Ahmed, Electrochemical C–H/C–C Bond Oxygenation: A Potential Technology for Plastic Depolymerization, *Chem. Rec.*, 2024, **24**(3), e202300331.
30 Y. Yan, H. Zhou, S.-M. Xu, J. Yang, P. Hao, X. Cai, Y. Ren, M. Xu, X. Kong, M. Shao, Z. Li and H. Duan, Electrocatalytic Upcycling of Biomass and Plastic Wastes to Biodegradable Polymer Monomers and Hydrogen Fuel at High Current Densities, *J. Am. Chem. Soc.*, 2023, **145**(11), 6144–6155.
31 Z. Zhai, Y. Lu, L. Ouyang, J. Lu, W.-L. Ding, B. Cao, Y. Wang, F. Huo, Q. Zhao, W. Wang, S. Zhang and H. He, Modulating Product Selectivity in Lignin Electroreduction with a Robust Metallic Glass Catalyst, *Nat. Commun.*, 2025, **16**(1), 3414.
32 P. K. Baroliya, M. Dhaker, S. Panja, S. A. Al-Thabaiti, S. M. Albukhari, Q. A. Alsulami, A. Dutta and D. Maiti, Transition Metal–Catalyzed C–H Functionalization Through Electrocatalysis, *ChemSusChem*, 2023, **16**(12), e202202201.
33 S. K. Sinha, P. Ghosh, S. Jain, S. Maiti, S. A. Al-Thabati, A. A. Alshehri, M. Mokhtar and D. Maiti, Transition-Metal Catalyzed C–H Activation as a Means of Synthesizing Complex Natural Products, *Chem. Soc. Rev.*, 2023, **52**(21), 7461–7503.
34 Z. Li, K. Su, J. Ren, D. Yang, B. Cheng, C. K. Kim and X. Yao, Direct Catalytic Conversion of Glucose and Cellulose, *Green Chem.*, 2018, **20**(4), 863–872.
35 P. Zhao, X. Sun, S. Hao, Y. Zhang, J. Chen, H. Zhang and S. Dong, Glucose Oxidase-like Rhodium Single-Atom Nanozymes: A Mimic Platform for Biometabolism and Electrometabolism of Glucose Oxidation at Neutral pH, *ACS Energy Lett.*, 2023, **8**(4), 1697–1704.
36 M. P. J. M. Van Der Ham, E. Van Keulen, M. T. M. Koper, A. A. Tashvigh and J. H. Bitter, Steering the Selectivity of Electrocatalytic Glucose Oxidation by the Pt Oxidation State, *Angew. Chem., Int. Ed.*, 2023, **62**(33), e20230670.
37 J. S. Brindle, P. S. Nelson, R. P. Charde, S. A. Sufyan and M. M. Nigra, Catalytic Cooperativity between Glucose Oxidase and Gold Nanoparticles in the Sequential Oxidation of Glucose to Saccharic Acid, *Green Chem.*, 2022, **24**(13), 5162–5170.
38 A. M. Cañete-Rodríguez, I. M. Santos-Dueñas, J. E. Jiménez-Hornero, A. Ehrenreich, W. Liebl and I. García-García, Gluconic Acid: Properties, Production Methods and Applications—An Excellent Opportunity for Agro-Industrial by-Products and Waste Bio-Valorization, *Process Biochem.*, 2016, **51**(12), 1891–1903.
39 Q. Zhang, Z. Wan, I. K. M. Yu and D. C. W. Tsang, Sustainable Production of High-Value Gluconic Acid and Glucaric Acid through Oxidation of Biomass-Derived Glucose: A Critical Review, *J. Cleaner Prod.*, 2021, **312**, 127745.

40 Y. Guo, J. Liu, Y.-T. Xu, B. Zhao, X. Wang, X.-Z. Fu, R. Sun and C.-P. Wong, *In Situ* Redox Growth of Mesoporous Pd-Cu_2O Nanoheterostructures for Improved Glucose Oxidation Electrocatalysis, *Sci. Bull.*, 2019, **64**(11), 764–773.
41 X.-D. Ma, R. Liu, S. Yue, H.-J. Xie and X.-H. Xia, Multilevel Structured CuCoP with Synergistic Catalytic Active Site Designed for Hydrogen Evolution Coupled Gluconic Acid Synthesis, *Rare Met.*, 2025, **44**(5), 3141–3155.
42 G. Moggia, J. Schalck, N. Daems and T. Breugelmans, Two-Steps Synthesis of D-Glucaric Acid via D-Gluconic Acid by Electrocatalytic Oxidation of D-Glucose on Gold Electrode: Influence of Operational Parameters, *Electrochim. Acta*, 2021, **374**, 137852.
43 T. Rafaïdeen, S. Baranton and C. Coutanceau, Highly Efficient and Selective Electrooxidation of Glucose and Xylose in Alkaline Medium at Carbon Supported Alloyed PdAu Nanocatalysts, *Appl. Catal., B*, 2019, **243**, 641–656.
44 J. P. Oña, L. Laverdure, R. M. Latonen, N. Kumar, M. Peurla, I. Angervo, K. Honkala and H. Grénman, Influence of Reaction Parameters on Nanogold-Catalyzed Glucose and Xylose Oxidation: A Joint Experimental and DFT Study, *ACS Catal.*, 2024, **14**(3), 1532–1544.
45 G. Yuan, S. Yu, J. Jie, C. Wang, Q. Li and H. Pang, Cu/Cu_2O Nanostructures Derived from Copper Oxalate as High Performance Electrocatalyst for Glucose Oxidation, *Chin. Chem. Lett.*, 2020, **31**(7), 1941–1945.
46 X. Wu, Z.-J. Zhao, X. Shi, L. Kang, P. Das, S. Wang, S. Chu, H. Wang, K. Davey, B. Zhang, S.-Z. Qiao, J. Gong and Z.-S. Wu, Multi-Site Catalysis of High-Entropy Hydroxides for Sustainable Electrooxidation of Glucose to Glucaric Acid, *Energy Environ. Sci.*, 2024, **17**, 3042–3051.
47 N. Neha, T. Rafaïdeen, T. Faverge, F. Maillard, M. Chatenet and C. Coutanceau, Revisited Mechanisms for Glucose Electrooxidation at Platinum and Gold Nanoparticles, *Electrocatalysis*, 2023, **14**(1), 121–130.
48 A. H. B. Dourado, A. G. M. da Silva, F. A. C. Pastrián, R. L. Munhos, A. P. De Lima Batista, A. G. S. De Oliveira-Filho, J. Quiroz, D. C. De Oliveira, P. H. C. Camargo and S. I. Córdoba de Torresi, *In Situ* FTIR Insights into the Electrooxidation Mechanism of Glucose as a Function of the Surface Facets of Cu_2O-Based Electrocatalytic Sensors, *J. Catal.*, 2019, **375**, 95–103.
49 W.-J. Liu, Z. Xu, D. Zhao, X.-Q. Pan, H.-C. Li, X. Hu, Z.-Y. Fan, W.-K. Wang, G.-H. Zhao, S. Jin, G. W. Huber and H.-Q. Yu, Efficient Electrochemical Production of Glucaric Acid and H_2 via Glucose Electrolysis, *Nat. Commun.*, 2020, **11**(1), 265.
50 M. P. J. M. Van Der Ham, T. J. P. Hersbach, J. J. Delgado, B. D. Matson, J. Lim, M. Führer, T. Van Haasterecht, M. W. G. M. Verhoeven, E. J. M. Hensen, D. Sokaras, M. T. M. Koper and J. H. Bitter, Improved Electrocatalytic Activity of Pt on Carbon Nanofibers for Glucose Oxidation Mediated by Support Oxygen Groups in Pt Perimeter, *Appl. Catal., B*, 2023, **338**, 123046.
51 G. Moggia, J. Schalck, N. Daems and T. Breugelmans, Two-Steps Synthesis of D-Glucaric Acid via D-Gluconic Acid by Electrocatalytic Oxidation of D-Glucose on Gold Electrode: Influence of Operational Parameters, *Electrochim. Acta*, 2021, **374**, 137852.
52 D. Bin, H. Wang, J. Li, H. Wang, Z. Yin, J. Kang, B. He and Z. Li, Controllable Oxidation of Glucose to Gluconic Acid and Glucaric Acid Using an Electrocatalytic Reactor, *Electrochim. Acta*, 2014, **130**, 170–178.
53 D. Düzenli, I. Onal and I. Tezsevin, Investigation of Glucose Electrooxidation Mechanism over N–modified Metal–doped Graphene Electrode by Density Functional Theory Approach, *J. Comput. Chem.*, 2022, **43**(26), 1793–1801.
54 J. Wu, X. Yang and M. Gong, Recent Advances in Glycerol Valorization via Electrooxidation: Catalyst, Mechanism and Device, *Chin. J. Catal.*, 2022, **43**(12), 2966–2986.
55 S. Bagheri, N. M. Julkapli and W. A. Yehye, Catalytic Conversion of Biodiesel Derived Raw Glycerol to Value Added Products, *Renewable Sustainable Energy Rev.*, 2015, **41**, 113–127.
56 G. Dodekatos, S. Schünemann and H. Tüysüz, Recent Advances in Thermo-, Photo-, and Electrocatalytic Glycerol Oxidation, *ACS Catal.*, 2018, **8**(7), 6301–6333.
57 Z. Li, J. Yan, J. Sun, P. Xu, C. Ma and C. Gao, Production of Value-Added Chemicals from Glycerol Using in Vitro Enzymatic Cascades, *Commun. Chem.*, 2018, **1**(1), 71.
58 P. U. Okoye, D. M. Arias, B. H. Hameed, P. J. Sebastian, S. Li and W. Song, Thermocatalytic Routes and Reactor Strategies for Valorization of Biodiesel-Derived Glycerol to Fuels, *Appl. Therm. Eng.*, 2022, **214**, 118901.
59 H. J. Kim, J. Lee, S. K. Green, G. W. Huber and W. B. Kim, Selective Glycerol Oxidation by Electrocatalytic Dehydrogenation, *ChemSusChem*, 2014, **7**(4), 1051–1056.
60 A. Cassani, N. Tuleushova, Q. Wang, H. Guesmi, V. Bonniol, J. Cambedouzou, S. Tingry, M. Bechelany, D. Cornu and Y. Holade, Fe-Modified Pd as an Effective Multifunctional Electrocatalyst for Catalytic Oxygen Reduction and Glycerol Oxidation Reactions in Alkaline Media, *ACS Appl. Energy Mater.*, 2021, **4**(9), 9944–9960.
61 R. M. L. M. Sandrini, J. R. Sempionatto, G. Tremiliosi–Filho, E. Herrero, J. M. Feliu, J. Souza-Garcia and C. A. Angelucci, Electrocatalytic Oxidation of Glycerol on Platinum Single Crystals in Alkaline Media, *ChemElectroChem*, 2019, **6**(16), 4238–4245.
62 W. Chen, L. Zhang, L. Xu, Y. He, H. Pang, S. Wang and Y. Zou, Pulse Potential Mediated Selectivity for the Electrocatalytic Oxidation of Glycerol to Glyceric Acid, *Nat. Commun.*, 2024, **15**(1), 2420.
63 Y. Zhou, Y. Shen and J. Xi, Seed-Mediated Synthesis of Pt_xAu_y@Ag Electrocatalysts for the Selective Oxidation of Glycerol, *Appl. Catal., B*, 2019, **245**, 604–612.
64 Y. Zhou, Y. Shen and X. Luo, Optimizing the Activity and Selectivity of Glycerol Oxidation over Core-Shell Electrocatalysts, *J. Catal.*, 2020, **381**, 130–138.
65 I. Terekhina, J. White, A. Cornell and M. Johnsson, Electrocatalytic Oxidation of Glycerol to Value-Added Compounds on Pd Nanocrystals, *ACS Appl. Nano Mater.*, 2023, **6**(13), 11211–11220.

66 S. Wang, Y. Lin, Y. Li, Z. Tian, Y. Wang, Z. Lu, B. Ni, K. Jiang, H. Yu, S. Wang, H. Yin and L. Chen, Nanoscale High-Entropy Surface Engineering Promotes Selective Glycerol Electro-Oxidation to Glycerate at High Current Density, *Nat. Nanotechnol.*, 2025, **20**(5), 646–655.

67 H.-Y. Yang, B. Sun, X. Xiao, X. Ai, R.-B. Jiang, P. Chen and Y. Chen, Adsorption Configuration Control on Pt-Bi_2O_3 for the Oriented Conversion of Glycerol to Glyceric Acid via Terminal Hydroxyl Oxidation, *Sci. Bull.*, 2025, **70**(18), 2977–2985.

68 T. Chen, L. Lv, J. Yu, J. Du, Z. Ma, C. Guan, H. Wei and H. Chu, Synergy of Rare Earth Single Atoms and Pt Nanoparticles for Efficient Electro-Oxidation of Glycerol into Glycerate, *Sci. China: Chem.*, 2025, **68**, 4205–4215.

69 J. Zhou, J. Chen, R. Shi, Q. Gao, X. Zhao, C.-J. Wang, Z. Guo, E. C. M. Tse, F. Liu and Y. Chen, Synergistic Pd-CoFe Sites for Efficient and Selective Electrooxidation of Glycerol to Glyceric Acid Coupled with H_2 Evolution, *Chem. Eng. J.*, 2025, **513**, 163056.

70 J. Li, Z. Li, Z. Zheng, X. Zhang, H. Zhang, H. Wei and H. Chu, Tuning the Product Selectivity toward the High Yield of Glyceric Acid in Pt–CeO_2/CNT Electrocatalyzed Oxidation of Glycerol, *ChemCatChem*, 2022, **14**(16), e202200509.

71 T. Chen, C. Guan, F. Yao, X. Qi, J. Yu, J. Du, L. Lv, H. Wei and H. Chu, Electrosynthesis of Glyceric Acid from Glycerol Oxidation on Au–CeO_2/CNT Catalyst, *J. Rare Earths*, 2025, **43**(3), 453–461.

72 H. J. Kim, Y. Kim, D. Lee, J.-R. Kim, H.-J. Chae, S.-Y. Jeong, B.-S. Kim, J. Lee, G. W. Huber, J. Byun, S. Kim and J. Han, Coproducing Value-Added Chemicals and Hydrogen with Electrocatalytic Glycerol Oxidation Technology: Experimental and Techno-Economic Investigations, *ACS Sustainable Chem. Eng.*, 2017, **5**(8), 6626–6634.

73 C. Liu, M. Hirohara, T. Maekawa, R. Chang, T. Hayashi and C.-Y. Chiang, Selective Electro-Oxidation of Glycerol to Dihydroxyacetone by a Non-Precious Electrocatalyst-CuO, *Appl. Catal., B*, 2020, **265**, 118543.

74 G.-S. Tran, T.-G. Vo and C.-Y. Chiang, Earth-Abundant Manganese Oxide Nanoneedle as Highly Efficient Electrocatalyst for Selective Glycerol Electro-Oxidation to Dihydroxyacetone, *J. Catal.*, 2021, **404**, 139–148.

75 M. S. Ahmad, K. H. Ng, C.-L. Chen, F. Kabir, T. Witoon, T. Y. Wu and C. K. Cheng, Nitrogen-Phosphorous Co-Doped Palladium Electrocatalyst for Glycerol Electro-Oxidation Reaction (GEOR): An Efficient System for Mesoxalic Acid and Dihydroxyacetone Production, *Fuel*, 2023, **333**, 126471.

76 G.-S. Tran, T.-G. Vo and C.-Y. Chiang, *Operando* Revealing the Crystal Phase Transformation and Electrocatalytic Activity Correlation of MnO_2 toward Glycerol Electrooxidation, *ACS Appl. Mater. Interfaces*, 2023, **15**(18), 22662–22671.

77 S. Lee, H. J. Kim, E. J. Lim, Y. Kim, Y. Noh, G. W. Huber and W. B. Kim, Highly Selective Transformation of Glycerol to Dihydroxyacetone without Using Oxidants by a PtSb/C-Catalyzed Electrooxidation Process, *Green Chem.*, 2016, **18**(9), 2877–2887.

78 T.-G. Vo, P.-Y. Ho and C.-Y. Chiang, *Operando* Mechanistic Studies of Selective Oxidation of Glycerol to Dihydroxyacetone over Amorphous Cobalt Oxide, *Appl. Catal., B*, 2022, **300**, 120723.

79 R. N. Gaines, B. A. Kleimenhagen, J. J. Griebler, L. C. Harris, A. A. Gewirth, S. A. Rogers and P. J. A. Kenis, Optimizing the Flow Electrooxidation of Glycerol Using Statistical Design of Experiments, *J. Electrochem. Soc.*, 2024, **171**(6), 063506.

80 F. A. Setiawan, I. S. Y. Louise, K. J. Smith, C. S. Kim and E. L. Gyenge, Paired Electrosynthesis Using Bio-Oils: Guaiacol Hydrodeoxygenation Coupled with Glycerol Oxidation in a Stirred Slurry Reactor, *ACS Sustainable Chem. Eng.*, 2025, **13**(21), 7803–7811.

81 B. Qiu, W. Hu, D. Zhang, B. Shen, Y. Wang and H. Chu, Efficient Conversion of Biomass to 5-Hydroxymethylfurfural via Hydrothermal Liquefaction: Mechanisms, Catalysts and Potential Applications, *Fuel*, 2024, **375**, 132568.

82 L. Guo, X. Zhang, L. Gan, L. Pan, C. Shi, Z. Huang, X. Zhang and J. Zou, Advances in Selective Electrochemical Oxidation of 5–Hydroxymethylfurfural to Produce High–Value Chemicals, *Adv. Sci.*, 2023, **10**(4), 2205540.

83 Z. Jiang, Y. Zeng, D. Hu, R. Guo, K. Yan and R. Luque, Chemical Transformations of 5-Hydroxymethylfurfural into Highly Added Value Products: Present and Future, *Green Chem.*, 2023, **25**(3), 871–892.

84 R.-J. Van Putten, J. C. Van Der Waal, E. De Jong, C. B. Rasrendra, H. J. Heeres and J. G. De Vries, Hydroxymethylfurfural, A Versatile Platform Chemical Made from Renewable Resources, *Chem. Rev.*, 2013, **113**(3), 1499–1597.

85 S. Pandey, M.-J. Dumont, V. Orsat and D. Rodrigue, Biobased 2,5-Furandicarboxylic Acid (FDCA) and Its Emerging Copolyesters' Properties for Packaging Applications, *Eur. Polym. J.*, 2021, **160**, 110778.

86 D. J. Chadderdon, L. Xin, J. Qi, Y. Qiu, P. Krishna, K. L. More and W. Li, Electrocatalytic Oxidation of 5-Hydroxymethylfurfural to 2,5-Furandicarboxylic Acid on Supported Au and Pd Bimetallic Nanoparticles, *Green Chem.*, 2014, **16**(8), 3778–3786.

87 X. Huang, B. Zhang, C. Guo, G. Yang, Q. Zhang, S. Li, H. Yu and F. Peng, Noble-Metal High-Entropy-Alloy Tuning the Products of Electrocatalytic 5-Hydroxymethylfurfural Oxidation, *Sustainable Energy Fuels*, 2023, **7**(21), 5224–5231.

88 Y. Xie, L. Sun, X. Pan, Z. Zhou and G. Zhao, Selective Two-Electron Electrocatalytic Conversion of 5-Hydroxymethylfurfural Boosting Hydrogen Production under Neutral Condition over $Co(OH)_2$-CeO_2 Catalyst, *Appl. Catal., B*, 2023, **338**, 123068.

89 X. Lu, K. Wu, B. Zhang, J. Chen, F. Li, B. Su, P. Yan, J. Chen and W. Qi, Highly Efficient Electro-Reforming of

5-Hydroxymethylfurfural on Vertically Oriented Nickel Nanosheet/Carbon Hybrid Catalysts: Structure–Function Relationships, *Angew. Chem., Int. Ed.*, 2021, **60**(26), 14528–14535.

90 H. Chen, J. Wang, Y. Yao, Z. Zhang, Z. Yang, J. Li, K. Chen, X. Lu, P. Ouyang and J. Fu, Cu–Ni Bimetallic Hydroxide Catalyst for Efficient Electrochemical Conversion of 5-Hydroxymethylfurfural to 2,5-Furandicarboxylic Acid, *ChemElectroChem*, 2019, **6**(23), 5797–5801.

91 Y. Lu, T. Liu, C. Dong, C. Yang, L. Zhou, Y. Huang, Y. Li, B. Zhou, Y. Zou and S. Wang, Tailoring Competitive Adsorption Sites by Oxygen-Vacancy on Cobalt Oxides to Enhance the Electrooxidation of Biomass, *Adv. Mater.*, 2022, **34**(2), 2107185.

92 G. Zhao, G. Hai, P. Zhou, Z. Liu, Y. Zhang, B. Peng, W. Xia, X. Huang and G. Wang, Electrochemical Oxidation of 5–Hydroxymethylfurfural on CeO_2–Modified Co_3O_4 with Regulated Intermediate Adsorption and Promoted Charge Transfer, *Adv. Funct. Mater.*, 2023, **33**(14), 2213170.

93 H. Wang, Y. Zhou and S. Tao, CoP-CoOOH Heterojunction with Modulating Interfacial Electronic Structure: A Robust Biomass-Upgrading Electrocatalyst, *Appl. Catal., B*, 2022, **315**, 121588.

94 H. Xu, G. Xin, W. Hu, Z. Zhang, C. Si, J. Chen, L. Lu, Y. Peng and X. Li, Single-Atoms Ru/NiFe Layered Double Hydroxide Electrocatalyst: Efficient for Oxidation of Selective Oxidation of 5-Hydroxymethylfurfural and Oxygen Evolution Reaction, *Appl. Catal., B*, 2023, **339**, 123157.

95 Y. Xie, L. Sun, X. Pan, Z. Zhou and G. Zhao, Selective two-electron electrocatalytic conversion of 5-Hydroxymethylfurfural boosting hydrogen production under neutral condition over $Co(OH)_2$-CeO_2 catalyst, *Appl. Catal., B*, 2023, **338**, 123068.

96 H. Zhou, Y. Ren, B. Yao, Z. Li, M. Xu, L. Ma, X. Kong, L. Zheng, M. Shao and H. Duan, Scalable Electrosynthesis of Commodity Chemicals from Biomass by Suppressing Non-Faradaic Transformations, *Nat. Commun.*, 2023, **14**(1), 5621.

97 Y. Ren, W. Kong, Y. Li, W. Zhan, C. Zhang, Y. Miao, B. Yao, S. Li, Z. Li, X. Liu, S. Zhan, H. Zhou, M. Shao and H. Duan, Selective Electrooxidation of 5-Hydroxymethylfurfural at Pilot Scale by Engineering a Solid Polymer Electrolyte Reactor, *Nat. Catal.*, 2025, **8**(8), 771–783.

98 M. Sun, Y. Wang, C. Sun, Y. Qi, J. Cheng, Y. Song and L. Zhang, Nitrogen-Doped Co_3O_4 Nanowires Enable High-Efficiency Electrochemical Oxidation of 5-Hydroxymethylfurfural, *Chin. Chem. Lett.*, 2022, **33**(1), 385–389.

99 W.-J. Liu, L. Dang, Z. Xu, H.-Q. Yu, S. Jin and G. W. Huber, Electrochemical Oxidation of 5-Hydroxymethylfurfural with NiFe Layered Double Hydroxide (LDH) Nanosheet Catalysts, *ACS Catal.*, 2018, **8**(6), 5533–5541.

100 K. Lee, Y. Jing, Y. Wang and N. Yan, A Unified View on Catalytic Conversion of Biomass and Waste Plastics, *Nat. Rev. Chem.*, 2022, **6**(9), 635–652.

101 D. Lee, H. Nam, M. W. Seo, S. H. Lee, D. Tokmurzin, S. Wang and Y.-K. Park, Recent Progress in the Catalytic Thermochemical Conversion Process of Biomass for Biofuels, *Chem. Eng. J.*, 2022, **447**, 137501.

102 S. Sun, Z. Liu, Z. J. Xu and T. Wu, Opportunities and Challenges in Biomass Electrocatalysis and Valorization, *Appl. Catal., B*, 2024, **358**, 124404.

103 H. Duan and F. Wang, Opportunities for Electrocatalytic Biomass Valorization, *Chem. Catal.*, 2022, **2**(4), 641–643.

104 S. Feng, P. T. T. Nguyen, X. Ma and N. Yan, Photorefinery of Biomass and Plastics to Renewable Chemicals Using Heterogeneous Catalysts, *Angew. Chem., Int. Ed.*, 2024, **63**(37), e202408504.

105 Y. M. Questell-Santiago, M. V. Galkin, K. Barta and J. S. Luterbacher, Stabilization Strategies in Biomass Depolymerization Using Chemical Functionalization, *Nat. Rev. Chem.*, 2020, **4**(6), 311–330.

106 Y. Wang, H. Wang, X. Kong and Y. Zhu, Catalytic Conversion of 5–Hydroxymethylfurfural to High–Value Derivatives by Selective Activation of C–O, C=O, and C=C Bonds, *ChemSusChem*, 2022, **15**(13), e202200421.

107 W. Zhao, F. Wang, K. Zhao, X. Liu, X. Zhu, L. Yan, Y. Yin, Q. Xu and D. Yin, Recent Advances in the Catalytic Production of Bio-Based Diol 2,5-Bis(Hydroxymethyl) Furan, *Carbon Resour. Convers.*, 2023, **6**(2), 116–131.

108 Y. Wan and J. Lee, Recent Advances in Reductive Upgrading of 5–Hydroxymethylfurfural via Heterogeneous Thermocatalysis, *ChemSusChem*, 2022, **15**(13), e202102041.

109 L. Hu, J. Xu, S. Zhou, A. He, X. Tang, L. Lin, J. Xu and Y. Zhao, Catalytic Advances in the Production and Application of Biomass-Derived 2,5-Dihydroxymethylfuran, *ACS Catal.*, 2018, **8**(4), 2959–2980.

110 W. Zhang, Y. Qi, Y. Zhao, W. Ge, L. Dong, J. Shen, H. Jiang and C. Li, Rh-Dispersed Cu Nanowire Catalyst for Boosting Electrocatalytic Hydrogenation of 5-Hydroxymethylfurfural, *Sci. Bull.*, 2023, **68**(19), 2190–2199.

111 K. Ji, M. Xu, S. Xu, Y. Wang, R. Ge, X. Hu, X. Sun and H. Duan, Electrocatalytic Hydrogenation of 5-Hydroxymethylfurfural Promoted by a Ru1Cu Single-Atom Alloy Catalyst, *Angew. Chem., Int. Ed.*, 2022, **61**(37), e202209849.

112 J. J. Roylance, T. W. Kim and K.-S. Choi, Efficient and Selective Electrochemical and Photoelectrochemical Reduction of 5-Hydroxymethylfurfural to 2,5-Bis (Hydroxymethyl)Furan Using Water as the Hydrogen Source, *ACS Catal.*, 2016, **6**(3), 1840–1847.

113 X. H. Chadderdon, D. J. Chadderdon, T. Pfennig, B. H. Shanks and W. Li, Paired Electrocatalytic Hydrogenation and Oxidation of 5-(Hydroxymethyl) Furfural for Efficient Production of Biomass-Derived Monomers, *Green Chem.*, 2019, **21**(22), 6210–6219.

114 H. Liu, T.-H. Lee, Y. Chen, E. W. Cochran and W. Li, Paired Electrolysis of 5-(Hydroxymethyl)Furfural in Flow Cells with a High-Performance Oxide-Derived Silver Cathode, *Green Chem.*, 2021, **23**(14), 5056–5063.

115 M. Li, T. Zheng, D. Lu, S. Dai, X. Chen, X. Pan, D. Dong, R. Weng, G. Xu and F. Wang, Facet Effect on the Reconstructed Cu-Catalyzed Electrochemical Hydrogenation of 5-Hydroxymethylfurfural (HMF) towards 2,5-Bis (Hydroxymethy)Furan (BHMF), *J. Energy Chem.*, 2023, **84**, 101–111.

116 X.-Q. Pan, X.-Y. Zhang, G.-X. Huang, S.-C. Mei, J.-W. Huang, J.-J. Chen, W.-J. Liu and H.-Q. Yu, Promoting Electrocatalytic Hydrogenation of 5-Hydroxymethylfurfural Using Buffer Electrolytes as Proton-Donating Motifs: Theoretical Predictions and Experimental Validations, *Appl. Catal., B*, 2023, **323**, 122191.

117 Z. Bao, C. Wang, Z. Wang, X. Bai, Y. Zhao, X. Shi and L. Zheng, Steering the Selectivity in Electrocatalytic Hydrogenation of 5-Hydroxymethylfurfural via Buffer Effect, *Chem. Eng. J.*, 2025, **515**, 163570.

118 H. Wu, X. Chen, H. Xu, R. Yang, X. Wang, J. Chen, Z. Xie, L. Wu and Y. Mai, Insight into the Mechanism of 5-Hydroxymethylfurfural Electroreduction to 2,5-Bis (Hydroxymethyl)Furan over Cu Anchored N-Doped Carbon Nanosheets, *Nano Res.*, 2024, **17**(9), 7991–7999.

119 G. Piao, S. H. Yoon, H. G. Cha, D. S. Han and H. Park, Porous Dendritic BiSn Electrocatalysts for Hydrogenation of 5-Hydroxymethylfurfural, *J. Mater. Chem. A*, 2022, **10**(45), 24006–24017.

120 G. S. De Luna, P. Zeller, E. Öztuna, F. Maluta, A. Canciani, F. Ospitali, P. H. Ho, A. Paglianti, A. Knop-Gericke, G. Fornasari, J. J. Velasco-Vélez and P. Benito, *In Situ* Development of a 3D Cu-CeO_2 Catalyst Selective in the Electrocatalytic Hydrogenation of Biomass Furanic Compounds, *ACS Catal.*, 2023, **13**(19), 12737–12745.

121 X.-L. Liu, W. Zhong, Y.-F. Jin, T.-J. Wang, X. Xiao, P. Chen, Y. Chen and X. Ai, Pd-Pt Bimetallene for the Energy-Saving Electrochemical Hydrogenation of 5-Hydroxymethyl-furfural, *Chin. J. Catal.*, 2025, **69**, 241–248.

122 Y. Wu, Y. Jiang, W. Chen, X. Yue, C. Dong, M. Qiu, T. T. T. Nga, M. Yang, Z. Xia, C. Xie, L. Xu, R. Wang, S. Wang and Y. Zou, Selective Electroreduction of 5-Hydroxymethylfurfural to Dimethylfuran in Neutral Electrolytes via Hydrogen Spillover and Adsorption Configuration Adjustment, *Adv. Mater.*, 2024, **36**(7), 2307799.

123 J. Schmidpeter, J. Gläsel, O. Shimelis, M. Schulz and B. J. M. Etzold, Spherical Carbon Catalysts as Scalable Fixed-Bed Electrode in Flow Electrosynthesis, *J. Environ. Chem. Eng.*, 2025, **13**(5), 118630.

124 P. Hauke, T. Merzdorf, M. Klingenhof and P. Strasser, Hydrogenation versus Hydrogenolysis during Alkaline Electrochemical Valorization of 5-Hydroxymethylfurfural over Oxide-Derived Cu-Bimetallics, *Nat. Commun.*, 2023, **14**(1), 4708.

125 R. Patel, P. Dhar, A. Babaei-Ghazvini, M. N. Dafchahi and B. Acharya, Transforming Lignin into Renewable Fuels, Chemicals, and Materials: A Review, *Bioresour. Technol. Rep.*, 2023, **22**, 101463.

126 L. A. Zevallos Torres, A. Lorenci Woiciechowski, V. O. De Andrade Tanobe, S. G. Karp, L. C. Guimarães Lorenci, C. Faulds and C. R. Soccol, Lignin as a Potential Source of High-Added Value Compounds: A Review, *J. Cleaner Prod.*, 2020, **263**, 121499.

127 R. Rinaldi, R. Jastrzebski, M. T. Clough, J. Ralph, M. Kennema, P. C. A. Bruijnincx and B. M. Weckhuysen, Paving the Way for Lignin Valorisation: Recent Advances in Bioengineering, Biorefining and Catalysis, *Angew. Chem., Int. Ed.*, 2016, **55**(29), 8164–8215.

128 L. Jia, C.-J. Li and H. Zeng, Cleavage/cross-Coupling Strategy for Converting β-O-4 Linkage Lignin Model Compounds into High Valued Benzyl Amines via Dual C–O Bond Cleavage, *Chin. Chem. Lett.*, 2022, **33**(3), 1519–1523.

129 S. Kim, S. C. Chmely, M. R. Nimlos, Y. J. Bomble, T. D. Foust, R. S. Paton and G. T. Beckham, Computational Study of Bond Dissociation Enthalpies for a Large Range of Native and Modified Lignins, *J. Phys. Chem. Lett.*, 2011, **2**(22), 2846–2852.

130 D. Raikwar, S. Majumdar and D. Shee, Thermocatalytic Depolymerization of Kraft Lignin to Guaiacols Using HZSM-5 in Alkaline Water–THF Co-Solvent: A Realistic Approach, *Green Chem.*, 2019, **21**(14), 3864–3881.

131 M. Oregui-Bengoechea, I. Gandarias, N. Miletić, S. F. Simonsen, A. Kronstad, P. L. Arias and T. Barth, Thermocatalytic Conversion of Lignin in an Ethanol/Formic Acid Medium with NiMo Catalysts: Role of the Metal and Acid Sites, *Appl. Catal., B*, 2017, **217**, 353–364.

132 X. Liu, Y. Wang and H. Duan, Recent Progress in Electrocatalytic Conversion of Lignin: From Monomers, Dimers, to Raw Lignin, *Precis. Chem.*, 2024, **2**(9), 428–446.

133 Y. He, X. Zeng, Z. Lu, S. Mo, Q. An, Q. Liu, Y. Yang, W. Lan, S. Wang and Y. Zou, Aqueous Electrocatalytic Hydrogenation Depolymerization of Lignin β-O-4 Linkage via Selective C_{aryl}–O(C) Bond Cleavage: The Regulation of Adsorption, *J. Am. Chem. Soc.*, 2024, **146**(46), 32022–32031.

134 J. Zhang, C. Suo, J. Sun, W. Li, S. Luo, C. Ma and S. Liu, Electrocatalysis Cα–Cβ and Cβ–O Bond Cleavage of Lignin Model Compound Using Ni-Co/C as Catalyst Electrode in Deep Eutectic Solvent, *J. Electroanal. Chem.*, 2023, **938**, 117385.

135 Q. Zhu, B. Gong, S. Huang, Y. Jin, S. Liu, S. Shao, Y. Yang, T. Cataldo, N. M. Bedford and J. C.-H. Lam, Rhombohedral $ZnIn_2S_4$-Catalysed Anodic Direct Electrochemical Oxidative Cleavage of C–O Bond in α-O-4 Linkages in Ambient Conditions, *Green Chem.*, 2024, **26**(7), 4135–4150.

136 X. Chen, Y. Qi, B. Liu, X. Qiu, X. Lin and Y. Qin, Structural Optimization of the $NiFe_2O_4$ Spinel Catalyst Aimed at Efficient Electrocatalytic C-O Bond Cleavage of Lignin, *Chem. Eng. Sci.*, 2025, **301**, 120722.

137 H. Zhang, Z. Li, X. Yang, M. Li, L. Wei and J. Yang, Study on the Efficient Electrocatalytic Depolymerization of α-O-4

Bond in Lignin Assisted by Simple Electrolyte, *Int. J. Biol. Macromol.*, 2024, **279**, 135260.

138 F. Lin, H.-Y. Tse, H. C. Erythropel, P. V. Petrović, M. Garedew, J. Chen, J. C.-H. Lam and P. T. Anastas, Development of a Ni-Promoted, Selective Electrochemical Reductive Cleavage of the C–O Bond in Lignin Model Compound Benzyl Phenyl Ether, *Green Chem.*, 2022, **24**(16), 6295–6305.

139 G. Liu, Y. Lu, J. Lu, Y. Wang, S. Liang, H. He and L. Jiang, Ionic Liquid-Trimetallic Electrocatalytic System for C–O Bond Cleavage in Lignin Model Compounds and Lignin under Ambient Conditions, *Nano Res.*, 2024, **17**(4), 2420–2428.

140 Y. P. Wijaya, R. D. D. Putra, K. J. Smith, C. S. Kim and E. L. Gyenge, Guaiacol Hydrogenation in Methanesulfonic Acid Using a Stirred Slurry Electrocatalytic Reactor: Mass Transport and Reaction Kinetics Aspects, *ACS Sustainable Chem. Eng.*, 2021, **9**(39), 13164–13175.

141 Z. Huang, Z. Yu, Z. Guo, P. Shi, J. Hu, H. Deng and Z. Huang, Selective Cleavage of C_β–O–4 Bond for Lignin Depolymerization via Paired–Electrolysis in an Undivided Cell, *Angew. Chem., Int. Ed.*, 2024, **63**(37), e202407750.

142 K. Wang, Z. Li, Z. Guo, J. Huang, T. Liu, M. Zhou, J. Hu and H. Li, Electroreductive Upgradation of Biomass into High-Value Chemicals and Energy-Intensive Biofuels, *Green Chem.*, 2024, **26**(5), 2454–2475.

143 M. Shao, Y. Xiong, Y. Wang, G. Wang, F. Hao, F. Liu, L. Guo, X. Meng, C. Wang, J. Wang, M. Wang and Z. Fan, Electroreductive Valorization of Biomass-Derived Aromatic Compounds with Metal Nanomaterials, *CCS Chem.*, 2025, **7**(8), 2233–2254.

144 S.-H. Shi, Y. Liang and N. Jiao, Electrochemical Oxidation Induced Selective C–C Bond Cleavage, *Chem. Rev.*, 2021, **121**(1), 485–505.

145 J. Li and H. Duan, Recent Progress in Energy-Saving Hydrogen Production by Coupling with Value-Added Anodic Reactions, *Chem*, 2024, **10**(10), 3008–3039.

146 Y. Wang, Y. Chen, L. Liu, L. Ren, J. Wang, K. Li, J. He, S. Li, J. Cai, C. Qi, P. Hu, Y. Cao, X. Zhong and J. Wang, Anion Doping Promotes Electrocatalyst Reconfiguration for Efficient C–C Bond Cleavage of 4-Methylcyclohexanol, *Green Chem.*, 2025, **27**(7), 2008–2018.

147 Y. Li, X. Wei, L. Chen, J. Shi and M. He, Nickel-molybdenum nitride nanoplate electrocatalysts for concurrent electrolytic hydrogen and formate productions, *Nat. Commun.*, 2019, **10**, 5335.

148 X. Han, H. Sheng, C. Yu, T. W. Walker, G. W. Huber, J. Qiu and S. Jin, Electrocatalytic Oxidation of Glycerol to Formic Acid by $CuCo_2O_4$ Spinel Oxide Nanostructure Catalysts, *ACS Catal.*, 2020, **10**(12), 6741–6752.

149 Y. Wang, Y.-Q. Zhu, Z. Xie, S.-M. Xu, M. Xu, Z. Li, L. Ma, R. Ge, H. Zhou, Z. Li, X. Kong, L. Zheng, J. Zhou and H. Duan, Efficient Electrocatalytic Oxidation of Glycerol via Promoted OH* Generation over Single-Atom-Bismuth-Doped Spinel Co_3O_4, *ACS Catal.*, 2022, **12**(19), 12432–12443.

150 Z. He, J. Hwang, Z. Gong, M. Zhou, N. Zhang, X. Kang, J. W. Han and Y. Chen, Promoting Biomass Electrooxidation via Modulating Proton and Oxygen Anion Deintercalation in Hydroxide, *Nat. Commun.*, 2022, **13**(1), 3777.

151 J. Wu, J. Li, Y. Li, X. Ma, W. Zhang, Y. Hao, W. Cai, Z. Liu and M. Gong, Steering the Glycerol Electro–Reforming Selectivity via Cation–Intermediate Interactions, *Angew. Chem.*, 2022, **134**(11), e202113362.

152 Z. Zhang, L. Xin, J. Qi, Z. Wang and W. Li, Selective Electro-Conversion of Glycerol to Glycolate on Carbon Nanotube Supported Gold Catalyst, *Green Chem.*, 2012, **14**(8), 2150.

153 D. Kim, L. S. Oh, Y. C. Tan, H. Song, H. J. Kim and J. Oh, Enhancing Glycerol Conversion and Selectivity toward Glycolic Acid via Precise Nanostructuring of Electrocatalysts, *ACS Catal.*, 2021, **11**(24), 14926–14931.

154 L. Shen, L. Sun, M. Douthwaite, O. Akdim, S. Taylor and G. J. Hutchings, Hollow Au_1Cu_1(111) Bimetallic Catalyst Promotes the Selective Electrochemical Conversion of Glycerol into Glycolic Acid, *ACS Catal.*, 2024, **14**(15), 11343–11351.

155 J. Wu, X. Liu, Y. Hao, S. Wang, R. Wang, W. Du, S. Cha, X. Ma, X. Yang and M. Gong, Ligand Hybridization for Electro–reforming Waste Glycerol into Isolable Oxalate and Hydrogen, *Angew. Chem., Int. Ed.*, 2023, **62**(9), e202216083.

156 J. Luo, F. Kong, J. Yang and M. Wang, NiCo-Phosphide Bifunctional Electrocatalyst Realizes Electrolysis of Sugar Solution to Formic Acid and Hydrogen, *Nano Lett.*, 2024, **24**(31), 9617–9626.

157 X. Chen, Z. Zhang, Y. Yang, B. Hu, Q. Wu, W. Fan, J. Hao and W. Shi, NiCu-Based Catalysts with High Selectivity for Electro–Oxidation of Glucose to Formic Acid, *Chem. Eng. Sci.*, 2024, **291**, 119937.

158 Z. Zhang, J. Zhao, M. Hong, S. Chen and Y. Qiao, Enhanced Electrocatalytic Glucose Oxidation Assisted Hydrogen Production *via* the Interfacial Synergistic Effect of $NiO/NiCo_2O_4$ Porous Nanowires, *Green Chem.*, 2024, **26**(15), 8808–8817.

159 Y. Zhu, H. Zhou, J. Dong, S. Xu, M. Xu, L. Zheng, Q. Xu, L. Ma, Z. Li, M. Shao and H. Duan, Identification of Active Sites Formed on Cobalt Oxyhydroxide in Glucose Electrooxidation, *Angew. Chem., Int. Ed.*, 2023, **62**(15), 202219048.

160 Z. Ma, H. Guo, P. Wang, L. Dai, S. Zhan and F. Shen, Construction of Ultra-Thin Nanosheets with Ni-O-Co Electron Channels to Accelerate Electron Transfer in Electrooxidation of Glucose to Formic Acid, *Chem. Eng. J.*, 2025, **514**, 163249.

161 F. Ma, C. Zhang, W. Li, R. Hu, Z. Wang, J. Wang, J. Li, Y. Nie, Z. Zheng and X. Jiang, Selectively Steering the Retention and Cleavage of C–C Bond in Electrooxidation of PET Plastic and Biomass-Derived Alcohols by Defective $Ni(OH)_{2-x}$-Supported Pt, *ACS Catal.*, 2025, **15**(6), 4759–4769.

162 C. G. Yoo, X. Meng, Y. Pu and A. J. Ragauskas, The Critical Role of Lignin in Lignocellulosic Biomass Conversion and Recent Pretreatment Strategies: A Comprehensive Review, *Bioresour. Technol.*, 2020, **301**, 122784.

163 Y. M. Questell-Santiago, M. V. Galkin, K. Barta and J. S. Luterbacher, Stabilization Strategies in Biomass Depolymerization Using Chemical Functionalization, *Nat. Rev. Chem.*, 2020, **4**(6), 311–330.

164 L. Dong, J. Xia, Y. Guo, X. Liu, H. Wang and Y. Wang, Mechanisms of Caromatic-C Bonds Cleavage in Lignin over NbO_x-Supported Ru Catalyst, *J. Catal.*, 2021, **394**, 94–103.

165 C.-H. Rao, H.-R. Wei, X.-L. Miao, M.-Z. Jia, X.-R. Yao, X.-Y. Zheng and J. Zhang, Selective Cleavage of Cα–Cβ Bonds in Lignin Models Using a Bifunctional Pyridinium Photocatalyst via a PCET Process, *Green Chem.*, 2023, **25**(10), 3974–3981.

166 C. S. Lancefield, O. S. Ojo, F. Tran and N. J. Westwood, Isolation of Functionalized Phenolic Monomers through Selective Oxidation and C-O Bond Cleavage of the β–O–4 Linkages in Lignin, *Angew. Chem.*, 2015, **127**(1), 260–264.

167 M. Marinović, P. Nousiainen, A. Dilokpimol, J. Kontro, R. Moore, J. Sipilä, R. P. De Vries, M. R. Mäkelä and K. Hildén, Selective Cleavage of Lignin β-*O*-4 Aryl Ether Bond by β-Etherase of the White-Rot Fungus *Dichomitus Squalens*, *ACS Sustainable Chem. Eng.*, 2018, **6**(3), 2878–2882.

168 T. Cui, L. Ma, S. Wang, C. Ye, X. Liang, Z. Zhang, G. Meng, L. Zheng, H.-S. Hu, J. Zhang, H. Duan, D. Wang and Y. Li, Atomically Dispersed $Pt–N_3C_1$ Sites Enabling Efficient and Selective Electrocatalytic C–C Bond Cleavage in Lignin Models under Ambient Conditions, *J. Am. Chem. Soc.*, 2021, **143**(25), 9429–9439.

169 Z. Fang, F. Li, M. Wang, F. Li, X. Wu, K. Fan, Q. Tang, L. Sun and P. Zhang, Selective Electrocatalytic Upgrading of Lignin to Aryl Aldehydes and Carboxylic Acids over Dodecyl Sulfate-Intercalated CoS Nanocones, *Appl. Catal., B*, 2023, **323**, 122149.

170 H. Zhou, Z. Li, S. Xu, L. Lu, M. Xu, K. Ji, R. Ge, Y. Yan, L. Ma, X. Kong, L. Zheng and H. Duan, Selectively Upgrading Lignin Derivatives to Carboxylates through Electrochemical Oxidative C(OH)–C Bond Cleavage by a Mn–Doped Cobalt Oxyhydroxide Catalyst, *Angew. Chem.*, 2021, **133**(16), 9058–9064.

171 B. V. Lyalin and V. A. Petrosyan, Electrosynthesis of Adipic Acid by Undivided Cell Electrolysis, *Russ. Chem. Bull.*, 2004, **53**(3), 688–692.

172 Z. Li, X. Li, H. Zhou, Y. Xu, S.-M. Xu, Y. Ren, Y. Yan, J. Yang, K. Ji, L. Li, M. Xu, M. Shao, X. Kong, X. Sun and H. Duan, Electrocatalytic Synthesis of Adipic Acid Coupled with H2 Production Enhanced by a Ligand Modification Strategy, *Nat. Commun.*, 2022, **13**(1), 5009.

173 F. Liu, X. Gao, R. Shi, J. Xiong, Z. Guo, E. C. M. Tse and Y. Chen, Graphdiyne as an Electron Modifier for Boosting Electrochemical Production of Adipic Acid, *Adv. Funct. Mater.*, 2024, **34**(6), 202310274.

174 R. Wang, Y. Kang, J. Wu, T. Jiang, Y. Wang, L. Gu, Y. Li, X. Yang, Z. Liu and M. Gong, Electrifying Adipic Acid Production: Copper–Promoted Oxidation and C–C Cleavage of Cyclohexanol, *Angew. Chem.*, 2022, **134**(50), 202214977.

175 X. Ren, Q. Zhang, Y. Tong, G. Zhou, C. Lin, Y. Zhao and P. Chen, Nickel-Copper Alloying Arrays Realizing Efficient Co-Electrosynthesis of Adipic Acid and Hydrogen, *J. Energy Chem.*, 2025, **101**, 7–15.

176 J. Chen and Y. Shen, Effects of Manganese Doping into Nickel Hydroxides for the Electrochemical Conversion of KA Oil, *ACS Sustainable Chem. Eng.*, 2024, **12**(15), 5907–5916.

177 S. Stiefel, A. Schmitz, J. Peters, D. Di Marino and M. Wessling, An Integrated Electrochemical Process to Convert Lignin to Value-Added Products under Mild Conditions, *Green Chem.*, 2016, **18**(18), 4999–5007.

178 S.-J. Yim, H. Oh, Y. Choi, G.-N. Ahn, C.-H. Park, Y. H. Kim, J. Ryu and D.-P. Kim, Modular Flow Reactors for Valorization of Kraft Lignin and Low-Voltage Hydrogen Production, *Adv. Sci.*, 2022, **9**(35), 2204170.

